Title
The Life and Death of a Tectonic Plate: Imaging the Juan de Fuca Plate with Amphibious Seismic Data

Author
Hawley, William Bythewood

Publication Date
2019

Peer reviewed|Thesis/dissertation

The Life and Death of a Tectonic Plate: Imaging the Juan de Fuca Plate with Amphibious Seismic Data

by

William Bythewood Hawley

A dissertation submitted in partial satisfaction of the

requirements for the degree of

Doctor of Philosophy

in

Earth and Planetary Science

in the

Graduate Division

of the

University of California, Berkeley

Committee in charge:

Professor Richard M. Allen, Chair
Professor Mark Richards
Professor Walter Álvarez
Professor Gibor Basri

Summer 2019

The Life and Death of a Tectonic Plate: Imaging the Juan de Fuca Plate with Amphibious Seismic Data

Abstract

The Life and Death of a Tectonic Plate: Imaging the Juan de Fuca Plate with Amphibious Seismic Data

by

William Bythewood Hawley

Doctor of Philosophy in Earth and Planetary Science

University of California, Berkeley

Professor Richard M. Allen, Chair

Understanding of Earth's evolution has been hindered, in part, by the technical challenges associated with placing seismic instruments on the seafloor. As technology improves, more arrays of ocean bottom seismometers are being deployed around the ocean basins. Perhaps the most ambitious such array, the Cascadia Initiative, covered the entirety of a small oceanic plate, the Juan de Fuca plate, with ocean bottom seismometers in a four-year experiment. That array is the primary motivation for this study.

The two models presented in this work, CASC16-P and CASC19-S, are teleseismic tomographic studies. They are each the first of their kind to use offshore and onshore data to simultaneously image the P- and S-wave seismic velocity structure of the mantle beneath the Juan de Fuca and North American plates. These models have provided insight into the tectonics of oceanic plates: how they are created, how they might interact with the mantle over the course of their life, how they might be influenced by an overriding continental plate, how they behave in the mantle after subduction, and how subduction could cease.

This work focuses on the on- and offshore regions of the Pacific Northwest of the United States—in particular, on the interaction between the Juan de Fuca plate, the North American plate, and the upper mantle. But it also demonstrates the value in oceanic arrays. The offshore instruments used in this study have allowed the identification of new features offshore, and better resolution of features near the coastlines. Ocean bottom seismology represents a rapidly growing new frontier that has the potential to investigate earth evolution in detail that was not previously possible. The work we present here has both helped illuminate the tectonics of the Pacific Northwest, and helped generate detailed hypotheses about the nature of global tectonics that will be tested elsewhere.

To family and friends who taught me the value of curiosity.

"The larger the island of knowledge, the longer the shoreline of wonder."

–Donald Hoffman

Contents

Contents **ii**

List of Figures **iv**

1 Introduction **1**

2 Imaging the Oceanic Mantle: New Constraints on the Formation and Evolution of the Juan de Fuca plate **3**

2.1 Introduction . . . 3
2.1.1 Geologic Setting . . . 4
2.2 Data and Methods . . . 6
2.2.1 Seismic Data . . . 6
2.2.2 Travel-time observations . . . 6
2.2.3 Tomographic inversion . . . 7
2.3 Tomographic Results . . . 11
2.3.1 Offshore . . . 13
2.3.2 Onshore . . . 15
2.3.3 Resolution Tests . . . 16
2.4 Discussion . . . 18
2.4.1 Offshore Features . . . 18
2.4.1.1 Juan de Fuca Ridge . . . 19
2.4.1.2 Oceanic Lithosphere-Asthenosphere Boundary . . . 22
2.4.2 Structure of the Juan de Fuca slab and surrounding mantle . . . 24
2.4.2.1 Incoming Plate Structure . . . 24
2.4.2.2 Intra-slab seismicity and megathrust interface . . . 25
2.4.2.3 Juan de Fuca slab morphology . . . 26
2.4.2.4 Subduction-induced mantle flow . . . 27
2.4.3 Segmentation of the Cascadia Subduction Zone . . . 29
2.4.3.1 Offshore segmentation . . . 29
2.4.3.2 Interface segmentation . . . 31
2.4.3.3 Deeper segmentation . . . 32
2.4.3.4 What causes segmentation? . . . 34

2.4.4 Mantle beneath western US . . . 36
2.5 Conclusion . . . 38

3 Tomography reveals buoyant asthenosphere accumulating beneath the Juan de Fuca plate 40
3.1 Introduction . . . 40
3.2 Method and Tomographic Model . . . 40
3.3 Interpretation . . . 42
3.4 Geodynamic Scaling Relationships . . . 44
3.5 Implications and Conclusions . . . 46
3.6 Resolution Tests . . . 46
3.7 Model Parameters . . . 47
3.8 Scaling Relationships . . . 47
3.9 Acknowledgements . . . 52

4 The Fragmented Death of the Farallon Plate 55
4.1 Introduction . . . 55
4.2 Data and Methods . . . 57
4.3 Tomographic Model . . . 58
4.4 Interpretation . . . 60
4.4.1 Causes of the hole . . . 60
4.4.2 Effects on the subducting Juan de Fuca plate . . . 62
4.4.3 Implications for subduction termination . . . 64
4.5 Conclusions . . . 64
4.6 Resolution Tests . . . 65
4.7 Acknowledgements, samples, and data . . . 65

5 Conclusion 68

Bibliography 71

List of Figures

2.1 Regional Overview 5
2.2 Removal of noise from OBS. 8
2.3 Subsets of the array with high station density. 9
2.4 Histograms of delays. 10
2.5 Examples of delays from two events. 11
2.6 Station and event corrections. 12
2.7 Slices through tomographic models. 14
2.8 Checkerboard resolution tests. 17
2.9 Kernel size. 18
2.10 Detail of Juan de Fuca – Gorda ridge. 20
2.11 Segmentation of the Cascadia Subduction Zone. 35

3.1 Regional Overview; Casc16-P study area. 41
3.2 Slices through Casc16-P, showing low velocity "roll." 43
3.3 Geodynamical model setup. 44
3.4 Resolution test: high-velocity slab. 48
3.5 Resolution test: low velocity layer thickness. 49
3.6 Resolution test: dipping low velocity layer depth 50
3.7 Station/event correction term tests. 51
3.8 Relationship between thickness and viscosity. 53

4.1 Regional overview; Casc19-S study area. 57
4.2 Slices through Casc19-S, showing hole in the slab. 59
4.3 Causes and effects of the hole in the Juan de Fuca slab. 61
4.4 Schematic model of the hole. 63
4.5 Resolution test: low velocities near the slab. 66
4.6 Resolution test: depth extent of the slab hole. 67

Acknowledgments

The work presented in this dissertation would not have been possible without the help, advice, and support of many people. First, I would like to thank my advisor, Richard Allen. Richard has been exceptional in his role, providing wisdom and guidance where it was needed, while largely allowing me to pursue the science that I found interesting. This style was not indifference; Richard was often more excited about my work than even I. His unwavering support is the foundation upon which this dissertation is built. This is a lesson I intend to carry with me not just through my career, but through many aspects of my life.

I took my first earth science class with Jerry Mitrovica in my final semester as an undergraduate at Harvard. I was writing a senior thesis for a degree in astrophysics, and was set to move to Dallas to become a high school physics teacher. Jerry took it upon himself to be for me an advocate like I had not known before. Were he not convinced that I should at least consider graduate school, I would certainly not have gone. His belief in me, and genuine desire to see me succeed, came at a time where I had almost lost both for myself.

I am grateful to many faculty, postdocs, and staff I have interacted with at Berkeley, too many to name here—but particularly to Mark Richards, for teaching me the importance of formulating more than one approach to arrive at a solution; Walter Alvarez for the continual reminder that curiosity animates scientists and the public alike; Roland Bürgmann, Barbara Romanowicz, Doug Dreger, Michael Manga, Bruce Buffett, Kurt Cuffey, Chi-Yuen Wang, Burkhard Militzer, Gibor Basri, Jennifer Strauss, Peggy Hellweg, Taka'aki Taira, Ronni Grapenthin, and many others.

Friends and colleagues from within and outside this department developed into a strong community. My officemates through the years: Qingkai, Mong-Han, Chris, Kathryn, Runze, Yuexin; other Earth Imaging graduate students: Rob, Cheng, Robert, Claire; those with whom I would sing: Devon, Noble, Becky, Steve, Sterling, George, Nick, Emma, Jacob, Vanessa, Christine; those with whom I would run: Noah, Stephanie, Jake, Jake, Nick; those with whom I shared science with the wider world: Tucker, Chris, Jenn, Kathryn, Mariel, Thomas; those with whom I would disappear into the mountains: Noble, Chris, Chris, Jake. I was fortunate to go to sea three times, and am grateful for the friendships that form when confined to a ship for weeks: Maya, Voon, Chris, Dan, Jim, Zach, Caroline, Yuki, Carlos, Emily, Josh, Ernie, Mark, Thomas, Dan, Julianna, Joey, Jeff, Trevor, Chris, Ryan, Sonya, Kaiola, Theresa, Marshal, Mohan, Adi, Ashley, Eivind, Vesi. Family and friends supported and visited me, even though they may not have understood what I was doing: Sally, Greg, Steve, Lauren, Chris, David, Olga, Isha, Stephanie, Titus, Tyler.

When I am with Chris Jensen, I feel we are like Lewis and Clark. We have been to the ends of the Earth together, and through all this time, he has been a sounding board, a

confidant, a cheerleader, and a brother. He pushes me and challenges me every day, and this dissertation certainly would not have been possible without him.

Chapter 1

Introduction

The long-term, large-scale evolution of the earth is described by plate tectonics (e.g., Dietz, 1961; Hess, 1962; McKenzie, 1969; McKenzie and Parker, 1967; Wilson, 1963, 1965). In this framework, the surface of the earth, the lithosphere, is divided into a dozen or so rigid plates that move relative to each other. Any section of the lithosphere falls generally into one of two classes: oceanic and continental lithosphere. Oceanic lithosphere is created at mid-ocean ridges. Where two plates move apart, upwelling material from the mantle reaches the surface, cools, and becomes new oceanic lithosphere. Eventually, within $\sim$200 million years, the majority of this material is recycled back into the mantle through subduction. Continental lithosphere, by contrast, is formed of lighter minerals that rarely experience subduction, and are therefore generally older, thicker, and structurally more complicated than the ocean basins. Because of this difference in how oceanic and continental lithosphere is created and recycled, along with the facts that oceanic plates cover a much larger proportion of the earth and tend to have larger plate velocities (e.g., DeMets et al., 2010), oceanic and continental plates likely play different roles in the dynamics of plate tectonics.

While plate tectonics does a remarkable job explaining many observations on earth's surface—including the structure of ocean basins and mountainous plateaus, and the locations of volcanos and earthquakes—key questions about the formation, evolution, and eventual recycling of tectonic plates remain unresolved: are mid-ocean ridges active or passive; i.e., does the upwelling mantle drive spreading at mid-ocean ridges, or is the upwelling simply a response to the diverging plates? How does flow in the mantle affect the motions of plates, and vice versa? How do small fragments of oceanic plates accrete onto nearby plates? What is the driving mechanism behind the motions of the plates?

Seismology is the primary tool for investigating the earth's interior. Seismic tomography, a method of inverting seismic wave travel-times for the 3-dimensional seismic velocity structure in some region of interest (e.g., Aki and Lee, 1976), has become an exceptionally powerful tool when combined with mineral physical constraints from the laboratory (e.g., Stixrude and Lithgow-Bertelloni, 2005). This technique has helped refine our view of the

present physical and chemical state of the interior of the earth.

Although many significant advances have been made since seismic tomography emerged in the 1970s, high-resolution regional studies must be performed beneath an array of seismic stations. Deploying seismometers on the ocean floor presents formidable challenges, which has limited our ability to study oceanic lithosphere. In turn, a complete, dynamical description of plate tectonics will likely remain out of reach until we achieve a full characterization of oceanic plates and the mantle beneath them. Until recently, deployments of ocean bottom seismometers have been geographically small and designed to help solve a specific geophysical phenomenon, such as the MELT (Mantle Electromagnetic and Tomography; MELT Seismic Team, 1998) experiment and PLUME (Plume-Lithosphere Undersea Melt Experiment; Wolfe et al., 2011).

The TransportableArray, part of EarthScope, represented a departure from the model of constructing arrays to provide data on focused research topics. The TransportableArray covered the entirety of the continental United States with seismometers approximately 70 km apart, each installed for at least two years. The Cascadia Initiative (Toomey et al., 2014) effectively extended TransportableArray to the west, covering the entirety of the Juan de Fuca plate from the Juan de Fuca Ridge, where it is created, to the Cascadia Subduction Zone, where it is recycled into the mantle. For the first time, we have the opportunity to image the entirety of an oceanic plate.

This dissertation advances our understanding of plate tectonics through placing bounds on the answers to the questions presented in the second paragraph of this chapter. The research uses a large compliment of seismic stations from multiple arrays, but relies most heavily on the Cascadia Initiative offshore, and the TransportableArray onshore. The two velocity models presented here are of compressional and shear wave velocity in the upper 2500 km of the earth beneath these arrays. This dissertation is organized into three sections. The first presents the two velocity models, discusses how they were generated, and contextualizes some of the important features that are found in the model. The second and third sections each focus on a single significant feature observed in the model. Each provides insight into the interaction that an oceanic plate has with the mantle beneath it.

Chapter 2

Imaging the Oceanic Mantle: New Constraints on the Formation and Evolution of the Juan de Fuca plate

2.1 Introduction

Western North America provides an exceptional opportunity to probe how the Earth's mantle affects—and is affected by—its crust. This is largely for two reasons: first, it is because the region displays a fantastic diversity of geological and geophysical phenomena. The dominant feature of the region is the plate boundary on the western margin, which is undergoing a transition from the convergent Cascadia Subduction Zone to the transform San Andreas and Queen Charlotte–Fairweather systems (Atwater, 1970). To the west, the entire Juan de Fuca oceanic plate exists within 500 km of this margin. To the east, the land that exists between the margin and the Great Plains, about 1500 km wide, comprises all types of tectonic faulting, a wide variety of Quaternary volcanic activity, and lithospheric ages that extend as far back as the Archaean Wyoming Craton (Hoffman, 1988)).

Second, western North America represents a good laboratory because of the remarkable extent of data that has been collected in the last fifteen years. The backbone of the seismic data comes from EarthScope's TransportableArray, which covered the entire U.S. with seismometers beginning in 2004, and a typical station spacing of ∼70km. A complimentary amphibious array, the Cascadia Initiative (Toomey et al., 2014), operated similar station spacing across the entire Juan de Fuca plate and the Cascadia Subduction Zone from 2011 to 2015. These two arrays, combined with smaller regional arrays, have allowed for significant advances in imaging the interior structure of the Earth, from the crust down to the core-mantle boundary, and from beneath a mid ocean ridge that creates an oceanic plate, through the subduction zone where that plate is recycled into the mantle, and into the continental interior, where interactions between the fragmenting slab, convection in the

mantle, and the overriding North American plate generate myriad geological phenomena on the surface.

In this work, we present two new body-wave tomographic models of the region that include data from both onshore and offshore. We will discuss our models in the context of four key research domains: (1) the processes that govern the formation and evolution of an oceanic plate; (2) new constraints on the morphology of the subducting slab; (3) along-strike segmentation of the Cascadia Subduction Zone; and (4) the interaction between the fragmenting slab, the extending North American lithosphere, and the actively convecting mantle underneath the western United States.

2.1.1 Geologic Setting

For the last ∼70 Ma, much of the evolution of North America has been driven by the subduction of the Farallon plate, and the subsequent transition from a convergent to a transverse plate boundary as North America migrated over the East Pacific Rise (Atwater, 1970; Severinghaus and Atwater, 1990), both in terms of changes in the crustal stress field and flow in the mantle. When this happened at about 30 Ma, a segment of the ridge ceased to exist, shutting off the creation of both plates along that segment. The Pacific plate, now immediately adjacent to North America, translates northward along the new plate interface, defined today by the San Andreas fault. The Farallon plate continued to sink beneath North America, and can be seen in tomographic images as a high-velocity body beneath eastern North America (e.g., van der Lee and Nolet, 1997; Porritt et al., 2014). The northern remnant of the Farallon plate continues to decrease in size, and exists today as the Juan de Fuca plate (Fig. 2.1).

A period of Farallon flat slab subduction is thought to have caused the Laramide Orogeny at ∼70 Ma (e.g., Humphreys and Coblentz, 2007; Liu et al., 2010). The collapse of the western side of the thickened North American lithosphere beginning at ∼20 Ma led to the Basin and Range province, but it is not clear whether it is being driven by gravitational instability as subduction ceased (Atwater, 1970; Humphreys and Coblentz, 2007) or by active mantle upwelling associated with the East Pacific Rise (Moucha et al., 2009). There is also ambiguity in whether the Columbia River Basalt eruptions at ∼17 Ma and the subsequent age-progressive Yellowstone hotspot track are related primarily to the subduction of the Juan de Fuca slab (James et al., 2011; Liu and Stegman, 2012; Zhou et al., 2018b) or a mantle plume (Camp and Ross, 2004; Darold and Humphreys, 2013; Obrebski et al., 2010).

There is also considerable uncertainty in the extent to which mantle flow affects plate motions, and vice versa. Two experiments at mid ocean ridges, one on the southern East Pacific Rise (Katz, 2010; MELT Seismic Team, 1998; Toomey et al., 2002) and the other on the Juan de Fuca ridge (Bell et al., 2016; Byrnes et al., 2017) suggest that mantle buoyancy plays a role in the process of plate creation, in contrast to the standard model, which envisions

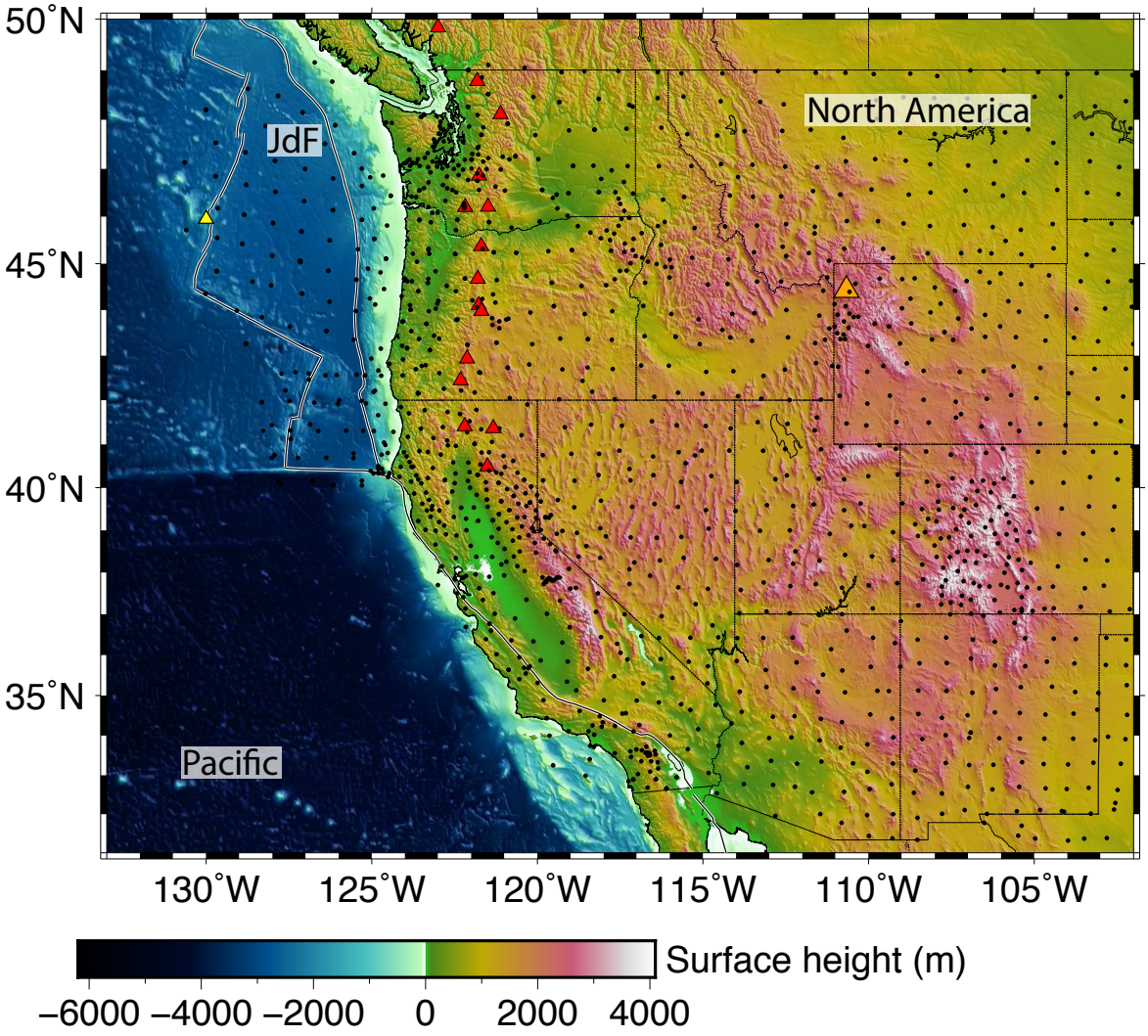

Figure 2.1: Overview of the Pacific Northwest. Plate boundaries are shown by double white lines. Plates are labeled, JdF is Juan de Fuca plate. Stations used in our tomographic models are black dots. Major Cascade volcanos are shown by red triangles, the yellow triangle offshore marks Axial Volcano, and the large orange triangle onshore marks Yellowstone.

melt passively produced by the divergence of two tectonic plates (e.g., McKenzie, 1969). Away from the ridges, on a broad scale, inferred flow in the asthenosphere aligns with plate motion (Becker et al., 2014), suggesting that the motions are coupled. But more localized studies of seismic anisotropy in oceanic lithosphere paint a more complicated picture in which flow in the mantle is not always aligned with the motion of the plate immediately above it (Bodmer et al., 2015; Lin et al., 2016; Martin-Short et al., 2015).

2.2 Data and Methods

2.2.1 Seismic Data

The bulk of our seismic data are derived from two large arrays: the EarthScope TransportableArray and the Cascadia Initiative (Toomey et al., 2014). The TransportableArray consists of land-based seismometers that covered the continental United States with a station spacing of approximately 70 km, and each station was in place for approximately two years. Although the array extends much farther east, we use data from stations that are west of 100°W (Fig. 2.1). The Cascadia Initiative was a four-year amphibious experiment, consisting of offshore stations that occupied 120 sites on and near the Juan de Fuca plate offshore the Pacific Northwest of North America, also with ∼70 km station spacing. During the first and third years, summer 2011 – 2012 and 2013 – 2014, the seismometers occupied sites in the northern half of the study area; in the second and fourth years, the instruments focused on the southern half of the study area. Because most of these sites were occupied for two years of the deployment, the Cascadia Initiative serves as an offshore extension of the Transportable Array.

In addition to these two arrays, we use data from two offshore networks, the Blanco Transform Experiment (network code X9), and Neptune Canada (NV); and the following land-based networks: Berkeley Digital Seismic Network (BDSN), ANZA Regional Network (ANZA), Cascade Chain Volcano Monitoring Network (CC), two EarthScope Flexible Array deployments (FACES and Mendocino), GEOSCOPE (GEO), Global Seismographic Network (IU), United States National Seismic Network (USNSN), COLZA/OSU, DELTA LEVY Northern California, Montana Regional Seismic Network (MRSN), Northern California Seismic Network (NCSN), Western Great Basin/Eastern Sierra Nevada Network (NN), Pacific Northwest Regional Seismic Network (PNSN), Southern California Seismic Network (SCSN), University of Oregon Regional Network (UO), University of Utah Regional Network (UURN), Yellowstone Wyoming Seismic Network (WY).

2.2.2 Travel-time observations

We select waveforms at each of these stations that show direct P- and S- wave arrivals from events whose epicenter is between 30 and 80 degrees from the station. The noise characteristics of ocean bottom stations is different from that of land-based stations: for OBS stations, the noise is generally derived from wind and waves, both by direct forcing at longer periods and by coupling to elastic waves in the earth at shorter periods (Webb, 1998). After removing instrument response, we analyzed the P- and S-wave arrivals on the vertical component in a number of frequency bands, and determined that much of the intermediate frequency range—about 0.5 to 2 Hz; frequencies that produce the best teleseismic arrivals on land-based stations (Lewis and Dorman, 1998)—is dominated by noise in the ocean stations. This analysis (Fig. 2.2) led us to apply a third-order bandpass filter to the record, with

corner frequencies of 0.08 Hz and 0.12 Hz for the P-waves (corresponding to periods of 8.3 – 12.5 s), and 0.025 Hz and 0.05 Hz for the S-waves (corresponding to periods of 20 – 40 s). For the onshore stations, we use two additional higher frequency bands for P-wave observations to recover finer structure, from 0.02 – 0.1 Hz (10 – 50 s) and from 0.8 – 2.0 Hz (0.5 – 1.25 s).

Windows around the first arrival were manually picked, using IASP91 (Kennett and Engdahl, 1991) to predict the arrival times. The arrival windows are then cross-correlated with all other arrivals for a given event using the method of VanDecar and Crosson (1990), and those arrivals with low cross-correlation coefficients were discarded. The threshold for discarding arrivals was different for different events and phases, but was always above 0.8. The arrivals for each event are demeaned, so that every event is then associated with a series of relative travel-time delays at each station.

We further clean the data by removing relative delays that do not pass a series of visual inspections. First, we remove delays from some stations that are more densely clustered than the rest of the array. These six regions are plotted in Fig. 2.3. For each of these clusters, we have used only delays from the single station that recorded arrivals for the largest number of earthquakes. After removing these clusters of stations, we remove delays that are larger than 97.5% of the of the remaining dataset; histograms for the both datasets are plotted in Fig. 2.4. Finally, we visually inspect the delays for each event. Some events show geographic patterns in the relative delay times that are physically unrealistic, and we remove all delays associated with these events. Examples of a good and bad event are shown in Fig. 2.5.

2.2.3 Tomographic inversion

After this process, we are left with a dataset of 61,559 P-wave arrivals and 34,670 S-wave arrivals. The model box we prescribe is a spherical cap, extending from 27°N to 51°N, from 101°W to 133°W, and from the surface to 2500 km depth. There are 65 nodes in each direction, corresponding to node spacing of 41.1 km in latitude, 38.4 km vertically, and ranging in longitude from 34.2 km in the north of the domain to 48.6 km in the south of the domain.

The inversion scheme we use is based on Obrebski et al. (2010). To associate each delay with a set of nodes, we calculate sensitivity kernels as a function of frequency band and depth following the method of Dahlen et al. (2000), which accounts or wavefront healing and scattering. We then invert these delays using an LSQR solver. In the inversion, we also include event and station correction terms (Fig. 2.6). The sensitivity kernels obviate the need for smoothing, but the model does require damping, both for the nodes within the model domain and for the event and station correction terms.

The event terms account for the fact that each event might have a different subset of stations, which would give rise to a different demeaned delay time for any given station

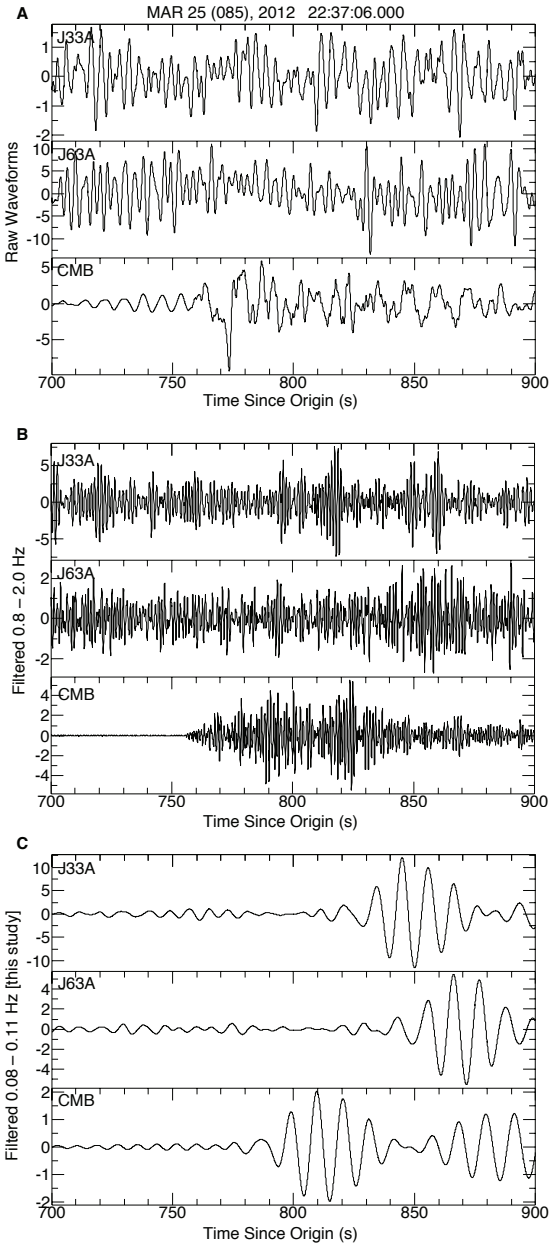

Figure 2.2: Noise removal. (A) Raw waveforms from a shallow OBS (7D.J33A, 348m depth), a deep OBS (7D.J63A, 2882m depth), and a land-based station (BK.CMB) showing the P arrival from a M7.1 event in Chile. (B) The same waveforms filtered 0.8 – 2.0 Hz, a common filter (Lewis and Dorman, 1998) for teleseismic P imaging studies onshore. The two OBS show no clear P arrival. (C) The primary filter band used in this study, 0.08 – 0.11 Hz, shows clear and similar arrivals on all three stations.

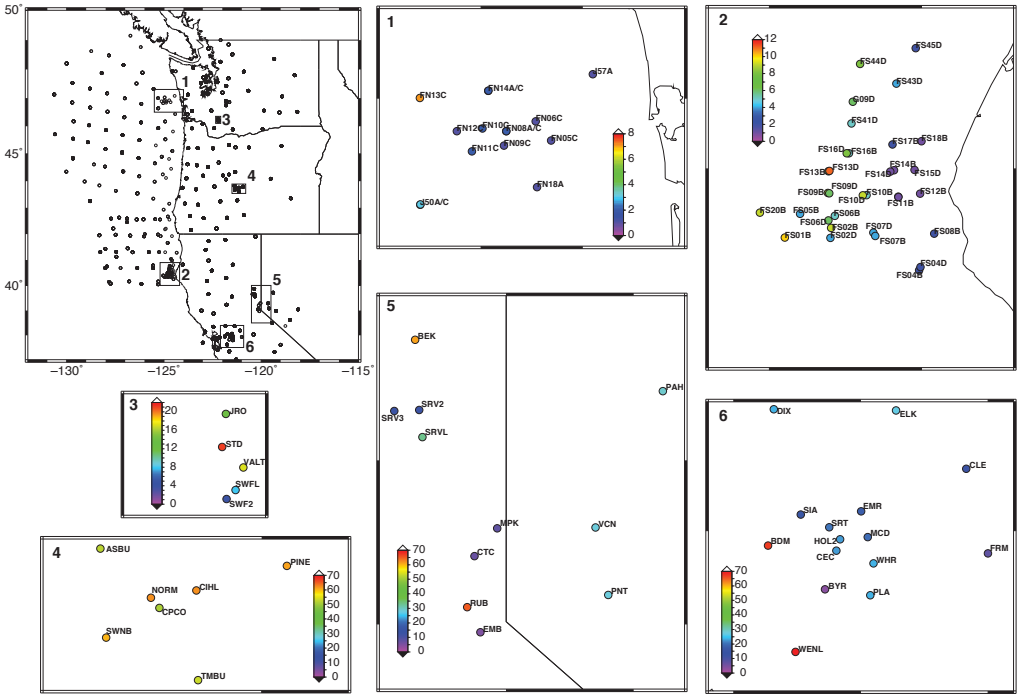

Figure 2.3: Subsets of the array with high station density. Overview map on the top left shows the stations offshore and near the coast. Six labeled boxes mark regions of high station density, corresponding to detailed maps to the right and below. Color represents the number of events observed by each station. In general, the one or two stations with the highest number of usable observations were kept for the inversion; the rest were discarded.

between events. Imagine, for example, two nearly co-located events are recorded two subsets of stations, but these subsets only have one instrument in common. One of the events has relatively fast delays, the other has relatively slow delays. Because each event is demeaned, the single station that records both events will be slower than average for one event (thus a positive delay), but faster than average for the other (thus a negative delay). These two delays, one positive and one negative, would have nearly identical sensitivities to nodes in the model domain, and would generate a large misfit if not corrected for the difference in mean delay between the two events. The event correction term is then included to account for the fact that the mean delay for each event is set to zero.

Station terms account for the velocity structure that is immediately beneath a station, attributable primarily to the crust and, especially offshore, sedimentary structure. These types of structures are shallow enough that they are not resolvable in the model. Without station correction terms, this velocity structure can be incorrectly mapped to the mantle, creating artifacts. While a perfect velocity model for the crustal and sedimentary structure

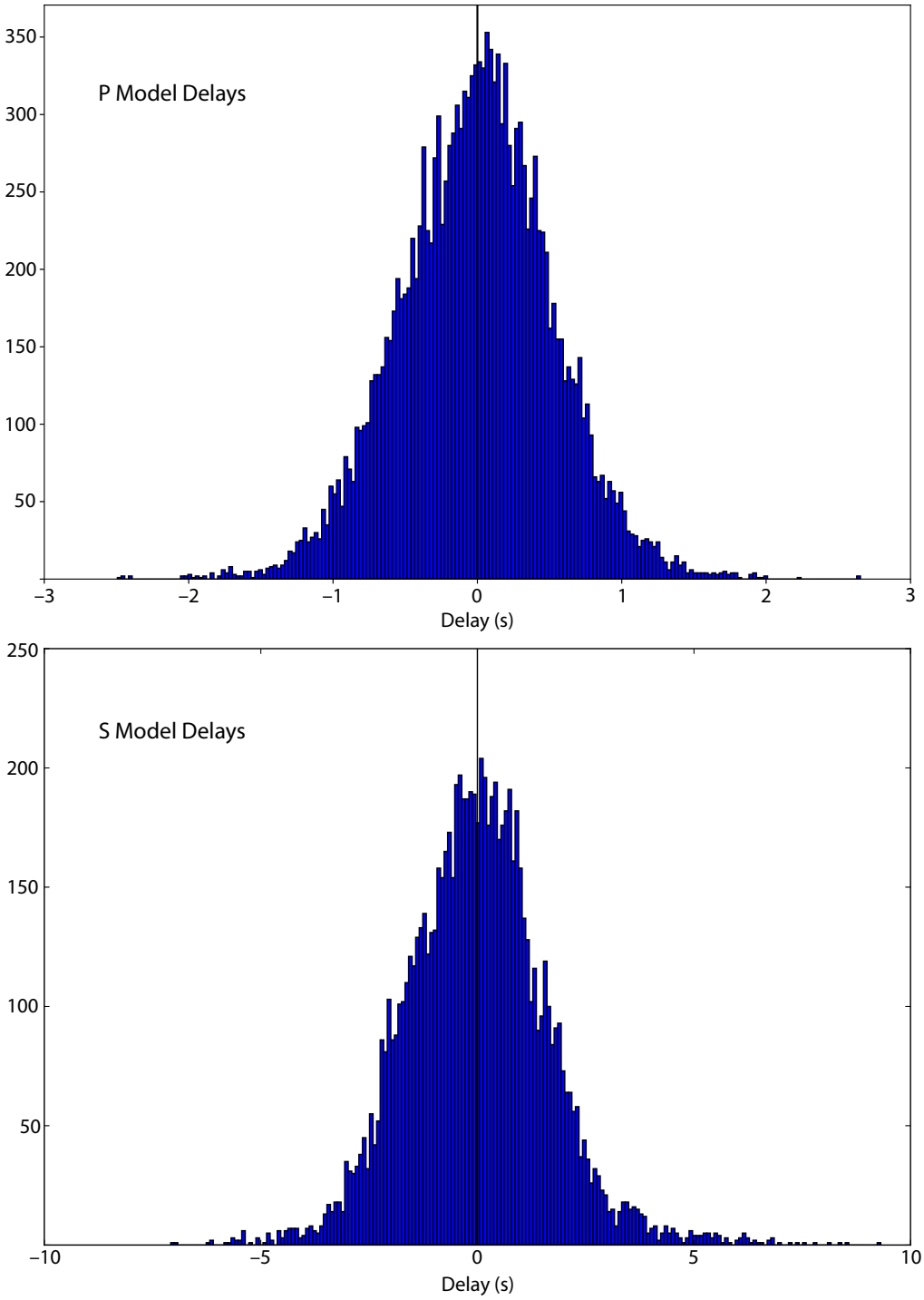

Figure 2.4: Histograms of delays. All arrivals picked in the P (top) and S (bottom) models, divided into 200 bins. The tails of each were removed for the models.

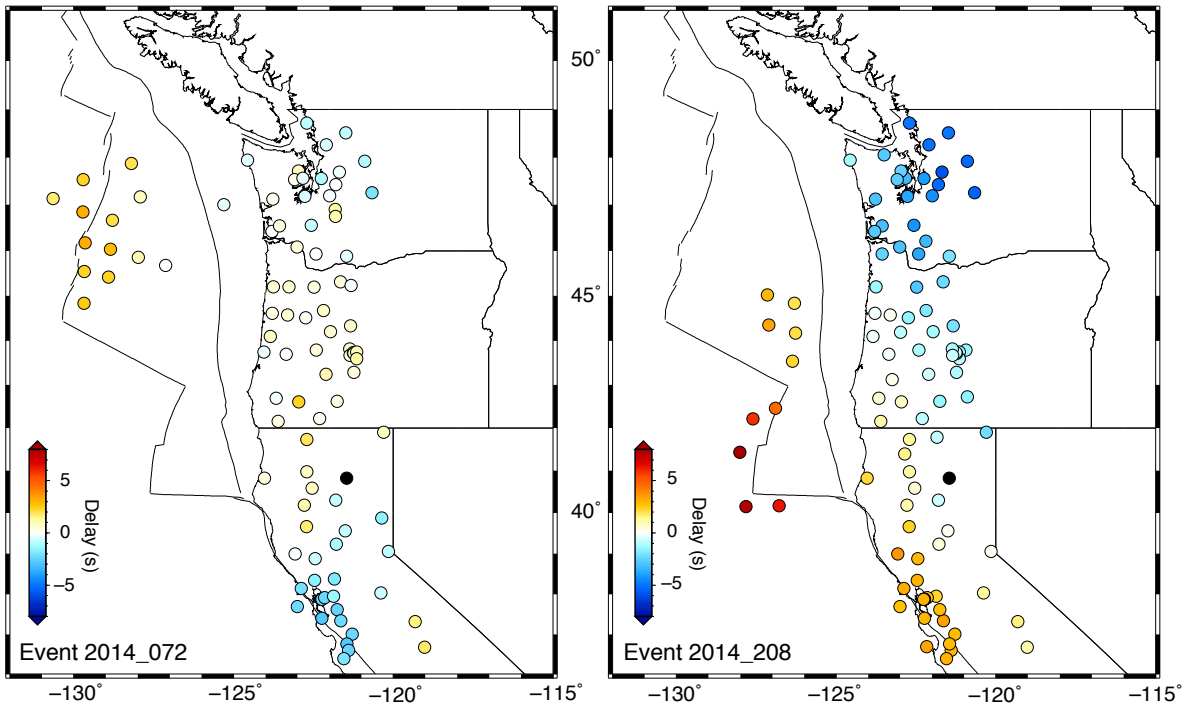

Figure 2.5: Examples of delays from two events. Colored circles represent the delay in seconds at each station for the event labeled in the lower left corner; all delays are plotted relative to BK.HATC, shown in black. The event on the left is a good event that is used in the inversion. The event on the right shows a suspicious linear pattern of increasing delays to the southwest, and was not used in the inversion.

would mitigate the need for station corrections, imposing incorrect shallow structure will generate artifacts in the model. Station corrections are an imperfect solution to this problem: in principle, station corrections may remove some signal from the mantle and attribute it to the station correction. This would tend to take the velocity structure toward the mean. Thus, our philosophy of including station corrections means that well-resolved structure in the model where the velocity deviates from 0% dV is unlikely to be an artifact due to shallow structure.

2.3 Tomographic Results

Our two tomographic models, Casc16-P and Casc19-S, are largely consistent with one another, and with other studies that have been performed in the region (Bodmer et al., 2018; Byrnes et al., 2017; James et al., 2011; Obrebski et al., 2010; Roth et al., 2008; Schmandt

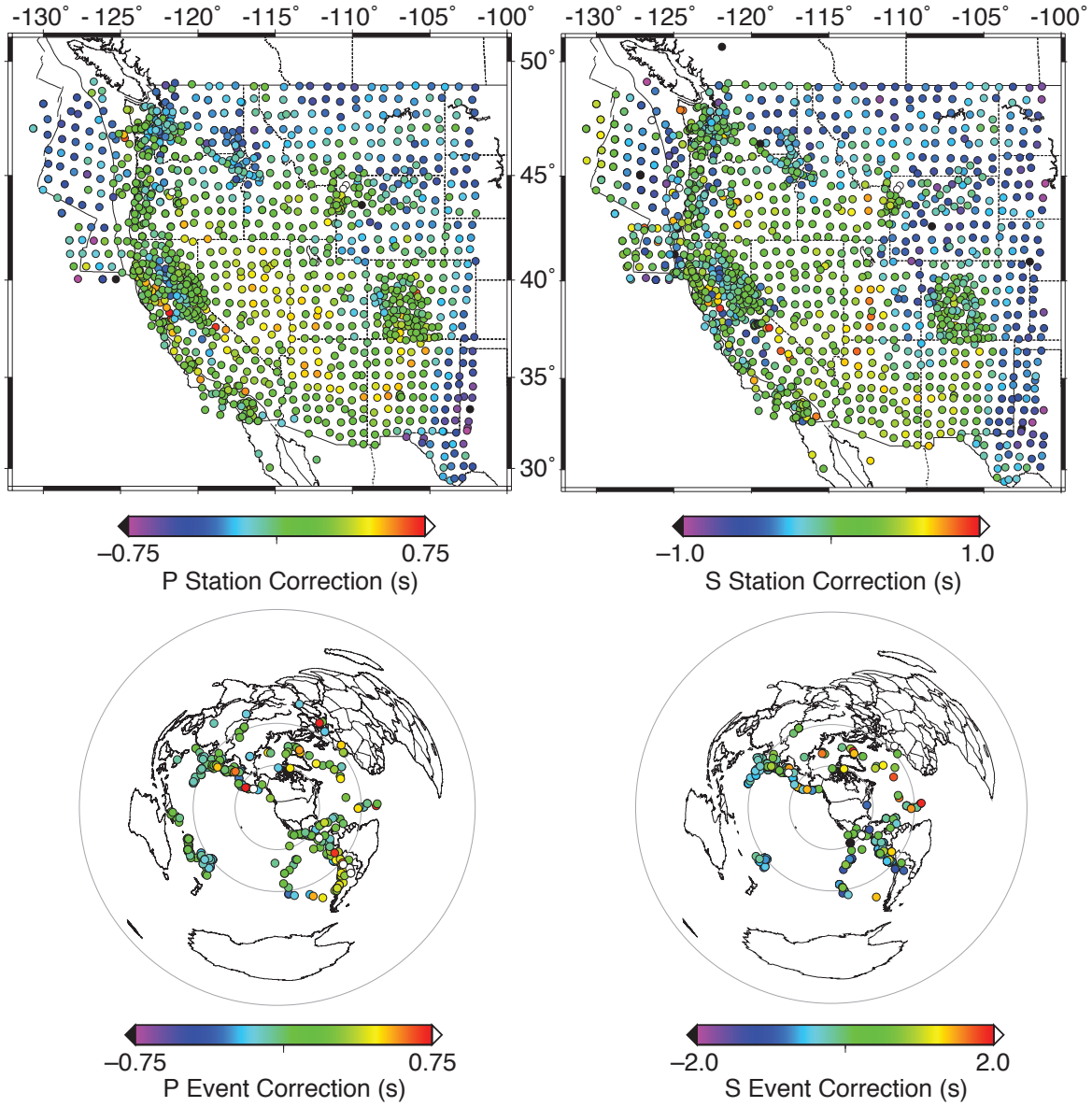

Figure 2.6: Station (above) and event (below) corrections for the P- (left) and S- (right) wave models.

and Humphreys, 2010; Schmandt and Lin, 2014). Most prior work has included only instruments onshore. The addition of data from ocean bottom seismometers in our models not only provides a wealth of new information about mantle structure beneath the Juan de Fuca plate, but also gives our models good resolution along the coastline, which is on the edge of land-based models, resulting in poor resolution. In addition to the two models presented here, only one model, the model of Bodmer et al. (2018), includes data that span

the coastline. Bodmer et al. (2018) use two surface wave models—one offshore (Bell et al., 2016) and one onshore (Schmandt and Lin, 2014)—to derive *a priori* starting crustal velocity models, and then solve for heavily damped station corrections. This represents a different and complimentary philosophy to our methodology, which uses no *a priori* constraints on crustal structure. Errors in an *a priori* crustal model could result in these errors being mapped into mantle depths. Our model, which uses underdamped station corrections, may pull signal out of the mantle and attribute it to station corrections, but it is unlikely to map crustal structure into mantle depths.

2.3.1 Offshore

The most marked difference between the P-wave and the S-wave models is offshore (Fig. 2.7). For almost the entire offshore section of the model domain, Casc16-P shows slightly fast velocities with relatively little variation, with the exception of a small patch of slightly low velocities underneath the Gorda ridge. Casc19-S, by contrast, shows pronounced low velocities beneath both the Gorda and the Juan de Fuca ridges, separated by a narrow region of nearly 0% dV_S. There is additionally a weaker low-velocity anomaly that underlies a section of the northern Juan de Fuca plate at about 48°N extending from the ridge in the west to the deformation front in the east. Casc19-S also shows a sharp transition from the low velocities under the Juan de Fuca ridge to a strong high velocity region in the central Juan de Fuca plate. While these two models are quite different from each other, they are qualitatively similar to two other body-wave models that incorporate Cascadia Initiative data. The top 150 km of the P-wave model of Bodmer et al. (2018) shows relatively uniform fast velocities across the Juan de Fuca plate, with lower velocities beneath the Gorda region. In contrast to Casc16-P and Bodmer et al. (2018), but similar to Casc19-S, the upper 200 km of the S-wave model of Byrnes et al. (2017) shows two strong low-velocity anomalies beneath the Juan de Fuca and Gorda ridges, separated by a narrow region of nearly 0% dV_S. The low velocities under the Juan de Fuca ridge are generally linear, but rotated counterclockwise relative to the orientation of the plate boundary. The active Axial Volcano sits on the ridge where the low-velocity feature crosses the ridge. Furthermore, the transition from low velocities under the Juan de Fuca ridge to fast velocities beneath the central Juan de Fuca plate is sharp, transitioning from -3% dV_S to $+3\%$ dV_S in $\sim$200 km.

Looking deeper in the upper mantle, Casc16-P transitions from slightly fast velocities as deep as 200 km depth to slightly slow velocities by 400 km. In Casc19-S, the S-wave velocities remain slow under the Gorda region, the Gorda ridge, and a small segment of the southernmost Juan de Fuca ridge. By 400 km depth, the slow anomalies beneath the Gorda region and the Gorda ridge have merged into one low-velocity anomaly, and the anomaly underneath the southernmost Juan de Fuca ridge has shifted northward, underneath Axial Volcano, and is perhaps connected to a much stronger low velocity feature to the east, under the subduction zone.

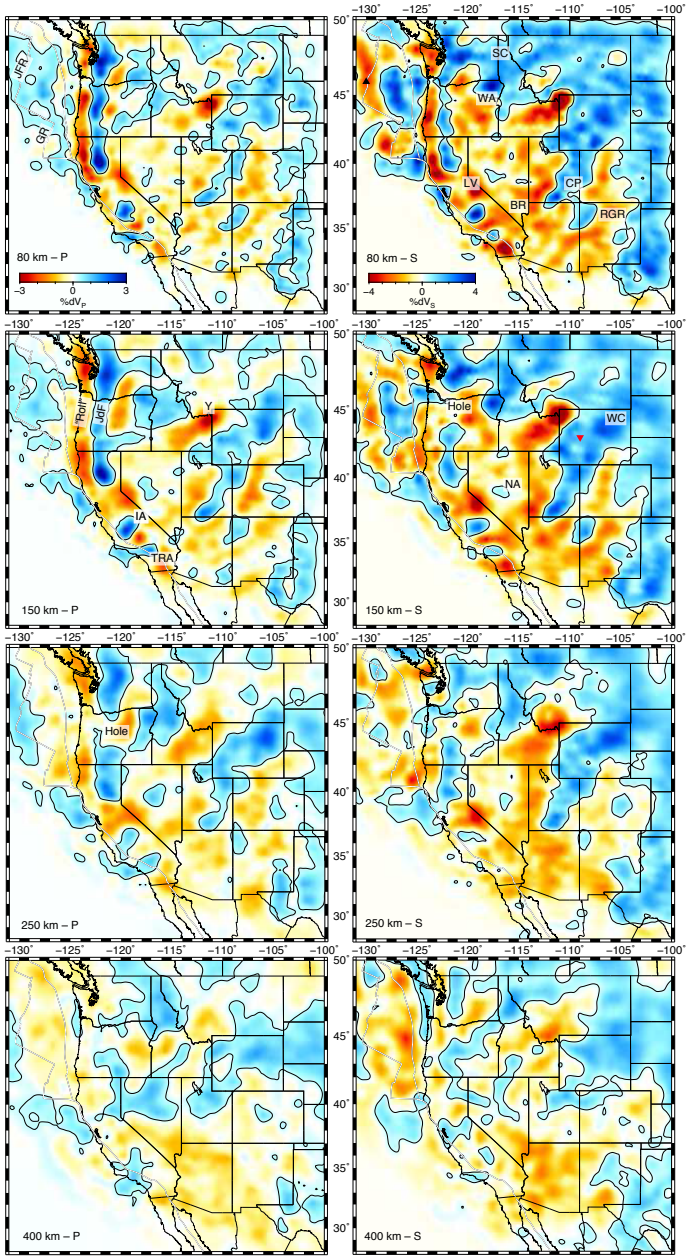

Figure 2.7: P (left) and S (right) models from 80 (top) to 400 (bottom) km depth. Features from the text are indicated: black triangle–Axial Volcano; red inverted triangle–deep WY earthquakes; JFR–Juan de Fuca Ridge; GR–Gorda Ridge; SC–Siletzia Curtain; WA–Wallowa Anomaly; LV–Long Valley Caldera; BR–Basin and Range; CP–Colorado Plateau; RGR–Rio Grande Rift; JdF–Juan de Fuca slab; Y–Yellowstone; IA–Isablla Anomaly; TRA–Transverse Ranges Anomaly; NA–Nevada Anomaly; WC–Wyoming Craton. Contours represent +0.25% $dV_{P/S}$.

2.3.2 Onshore

Onshore, Casc16-P shows three prominent anomalies at both 80 and 150 km depth: one high velocity feature that strikes north at 122°W, from approximately 40°N to the northern edge of our resolution at 50°N, consistent with the location of the Juan de Fuca slab. Second, there is a low-velocity feature with similar strike and longitude extent as the Juan de Fuca slab, offset to the west by approximately 1.5°, interpreted as a region of buoyant material in the asthenosphere (Bodmer et al., 2018; Hawley et al., 2016). Finally, a prominent low velocity feature is seen at 44.5°N, 111°W, interpreted as the Yellowstone hotspot (Obrebski et al., 2010; Schmandt and Humphreys, 2010; Waite et al., 2006). Two smaller high velocity anomalies appear in southern California: the Isabella Anomaly (Porritt et al., 2014; Zandt et al., 2004) at ∼36°N, 119.5°W; and the Transverse Ranges Anomaly (Nicholson et al., 1994) at ∼34°N, 121°W.

These same features appear in Casc19-S, but are not as prominent relative to other velocity anomalies. Other anomalies are visible in both models, but are more prominent in the S-wave model. The high velocity Siletzia Curtain underneath eastern Washington, northern Idaho, and the northeasternmost corner of Oregon, at ∼117°W, from ∼46°N to almost the Canadian border at 49°N, is interpreted to be a fragment of the Farallon slab that accreted at ∼50 Ma (Schmandt and Humphreys, 2010). The southwestern corner of these high velocities is a particularly anomalously fast region; it has been interpreted also as its own anomaly named after the Wallowa mountains at the surface (Darold and Humphreys, 2013; Hales et al., 2005). The Basin and Range province is underlain by low seismic velocities, beginning near the Siletzia Curtain in the north, extending southward through Nevada and into southern Arizona and southwestern New Mexico, as far southeast as ∼33°N, 107°W, where it transitions into the Rio Grande Rift. The slowest region in the Basin and Range province outside of the Snake River Plain is in eastern California, at ∼38°N, 119°W, consistent with the location of Long Valley Caldera. Just to the northeast of this low velocity anomaly is a slightly positive velocity anomaly, consistent with the location of the Nevada Anomaly (Roth et al., 2008). Farther to the east, a pair of high velocity anomalies (which are connected in the 80 km depth slice of Casc19-S) extend into the Basin and Range province from the northeast, at ∼37.5°N, 112°W and ∼36°N, 109°W. This feature is consistent with the location of the Colorado Plateau, a stable region of very little Cenozoic deformation immediately adjacent to the highly extended Basin and Range (Zandt et al., 1995), characterized by a steep lateral gradient in seismic velocity (Schmandt and Humphreys, 2010; Sine et al., 2008). Finally, high velocities to the northeast of the Colorado Plateau are consistent with the Archean age Wyoming Craton (Foster et al., 2006), which has been characterized by high velocities in seismic studies (Hopper et al., 2014; Wagner et al., 2010) and by the deepest earthquakes recorded outside of a subduction zone (Frohlich et al., 2015).

One striking difference between Casc16-P and Casc19-S at 150 km is that in the P-wave model, the Juan de Fuca slab is one continuous high-velocity feature along-strike, whereas

in the S-wave model, there is a gap in the high velocities from ∼44°N to 46°N. In the P-wave model, the signal from this central region is weaker at 200 km depth, but the P-wave model does not show a gap in the high-velocity signal from the slab until 250 km depth, significantly deeper than the feature appears in the S-wave model. This gap in high velocities is seen in virtually every tomographic study in the region that has resolution below 150 km depth (Bodmer et al., 2018; Hawley and Allen, 2019; Hawley et al., 2016; James et al., 2011; Obrebski et al., 2010; Roth et al., 2008; Schmandt and Humphreys, 2010; Schmandt and Lin, 2014; Xue and Allen, 2007), but these studies are not consistent in the depth at which they image this hole. For example, the hole appears in the P-wave model of James et al. (2011) by 150 km depth, in the S-wave model of Schmandt and Humphreys (2010) by 200 km, and in the P-wave model of Schmandt and Lin (2014) by 270 km. This hole also appears in discontinuity structure, as in the Kirchoff migration receiver function study of Cheng et al. (2017).

In both the P-wave and S-wave models, the upper mantle below ∼200 km is broadly characterized by high velocities to the north and east, with low velocities to the south and west. Unsurprisingly, the edges of the low velocity region at depth do not match precisely the boundaries of the Basin and Range province. Notable regions of high velocity include the Siletzia curtain (Schmandt and Humphreys, 2010) and the Wyoming Craton (Foster et al., 2006), both of which extend to 400 km depth in both the P-wave and the S-wave models. Finally a low velocity feature is seen beneath Yellowstone, particularly in Casc19-S, down to 400 km.

2.3.3 Resolution Tests

The resolution of our models is determined through standard checkerboard tests. The results of the checkerboard tests are shown in Fig. 2.8. These checkerboards show particularly good resolution near the subduction zone, down to ∼300 km depth for Casc19-S, and below 450 km in Casc16-P. Both models have good resolution underneath North America, but tend to lose resolution in the upper mantle beneath the Juan de Fuca plate. Casc19-S seems to have resolution that drops off more quickly with depth; this is likely a combination of the fact that the S-wave kernels are larger (Fig. 2.9), and there are simply fewer S-wave observations, particularly offshore.

We perform further resolution tests to assess specific geometries that are important for our interpretations. We present these tests when we discuss the interpretation of our seismic models.

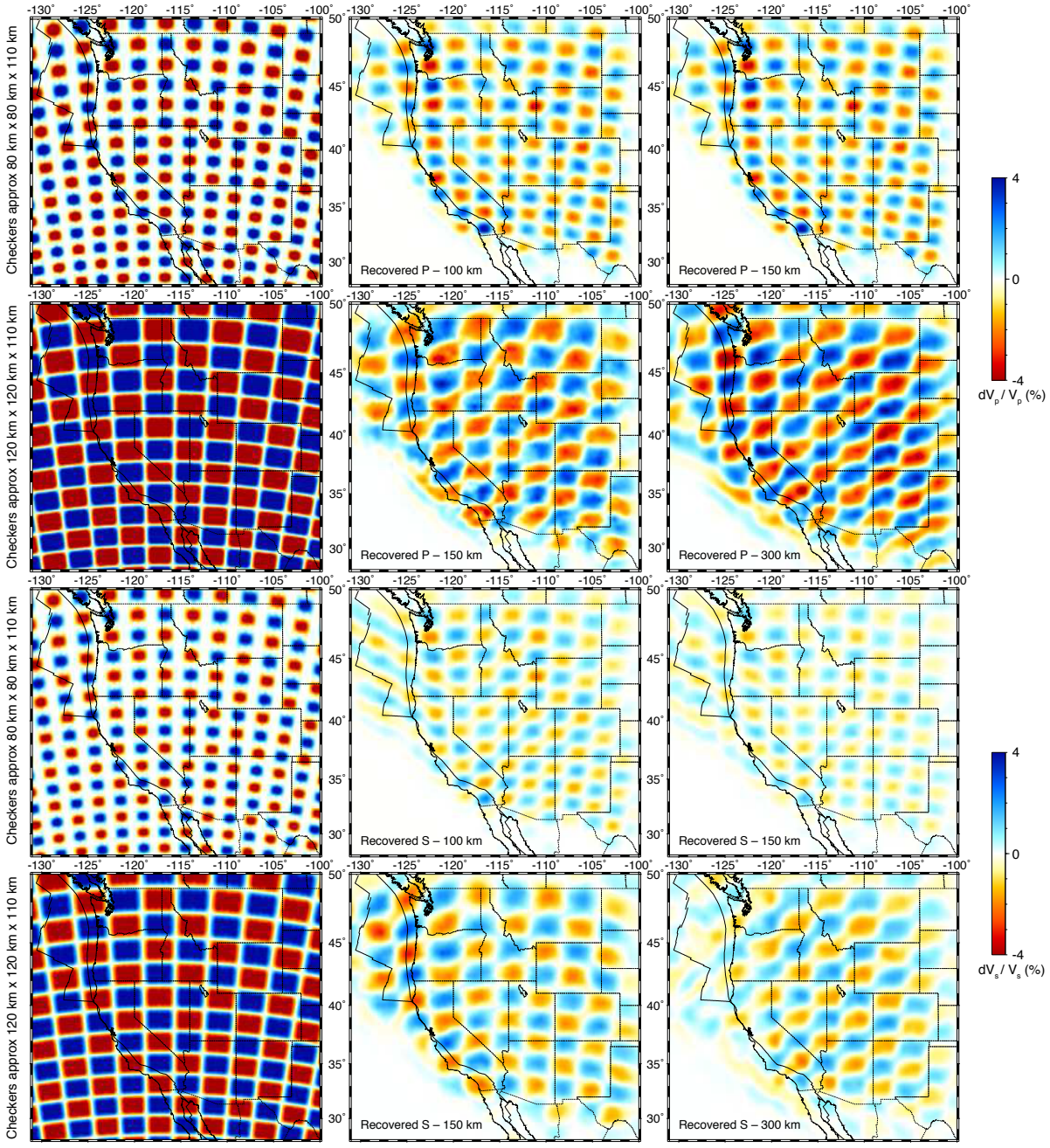

Figure 2.8: Checkerboard resolution tests for P (top two rows) and S (bottom two rows), at two different scales, indicated at the far left. Left column—input; center and right columns—recovery of the input model at the depth indicated in the lower left corner.

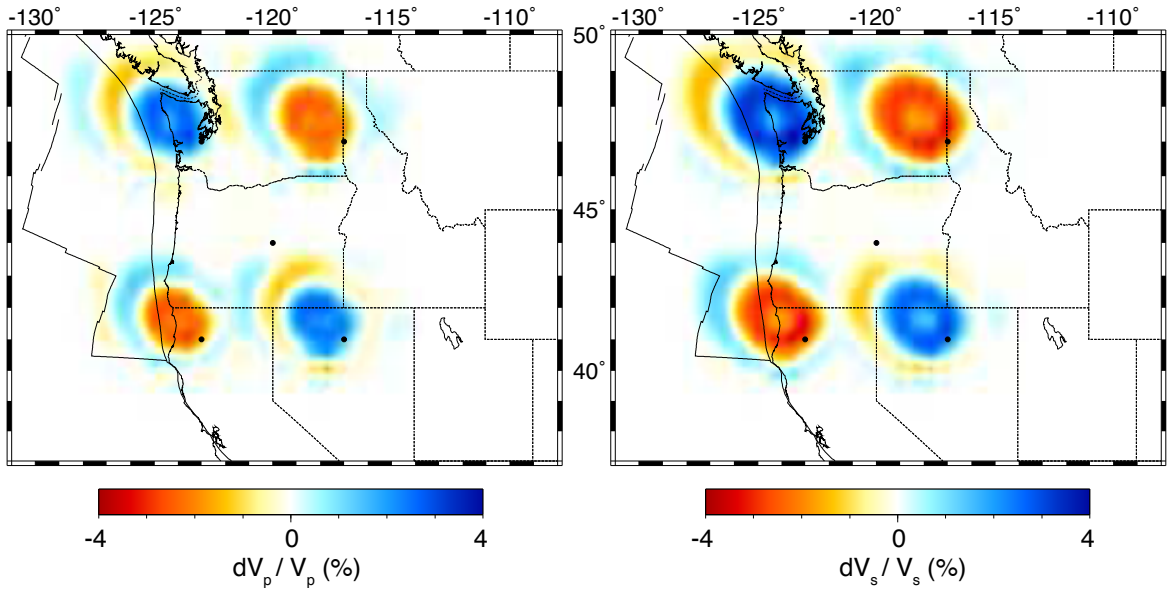

Figure 2.9: Demonstration of kernel size for offshore data in P (left) and S (right) models. Five dummy stations (black dots) have delays assigned to them: +0 s (center); −5 s (top left and bottom right); +5 s (top right and bottom left). Slice is at 150 km depth.

2.4 Discussion

The Western part of North America and the regions just offshore have abundant geophysical processes, and taken together, represents one of the most densely instrumented regions of the world. Correspondingly, there is no shortage of models and interpretations of those geophysical processes.

The tomographic models we show here are the first such models to cover this broad region, and offer an opportunity to explore how different phenomena interact across the model domain. We will discuss features generally in a pattern that goes from west to east, beginning with features offshore and in the Juan de Fuca mantle, continuing to processes related to the subducting slab. We then will discuss segmentation of the subduction zone, which will include features on and under both the Juan de Fuca plate and the North American plate, and will finally discuss the rest of the broad region to the east.

2.4.1 Offshore Features

Oceanic lithosphere comprises the majority of Earth's surface, and have plate velocities that are generally much faster than continental lithosphere. They are much more closely linked with mantle convection because unlike continents, they are formed out of the mantle at mid-ocean ridges, and return to the mantle at subduction zones. Understanding their formation,

evolution, and demise is critical for understanding plate tectonics, and ultimately building an accurate model for long-term Earth evolution. Oceanic plates are difficult to instrument, but the Cascadia Initiative presents the opportunity to image an oceanic plate in its entirety for the first time.

2.4.1.1 Juan de Fuca Ridge

The low shear wave velocities that we image beneath the Juan de Fuca ridge are consistent with the elevated temperatures and/or partial melt fraction that are expected from upwelling and decompression melting beneath mid-ocean ridges. Upwelling is required for the creation of new plates, but the cause of the upwelling remains debated, even though mid-ocean ridges are relatively simple volcanic settings. In particular, study of mantle flow underneath ridges has been focused on two endmember cases: passive and active. Passive models describe the upwelling flow in the mantle as being simply in response to divergent motion of two tectonic plates (e.g., McKenzie, 1969). Active models envision a large component of the upwelling to be driven by buoyancy forces within the mantle (e.g., Katz, 2010). Difficulties remain in determining which of these two models best fits global observations.

Two previous shear-wave tomographic studies of the Juan de Fuca ridge—one using Rayleigh waves (Bell et al., 2016), and the other using teleseismic body waves (Byrnes et al., 2017), similar to our model—have provided two pieces of evidence for active upwelling in this region: pronounced asymmetry about the ridge axis, and a strong lateral gradient in shear wave velocities with eastward distance from the ridge. The asymmetry describes a difference between the eastern and the western flanks of the ridge, primarily that the western (Pacific) side is characterized by slower shear wave velocities and more abundant seamounts. On the western flank of the Juan de Fuca ridge, shear wave velocities in the upper ∼75 km are as low as 4.0 km/s, a strong indication of partial melt (Bell et al., 2016). S-P receiver functions, which image discontinuities in velocity structure, are able to detect the base of the partial melt zone beneath the ridge, and the strongest signal of this impedance contrast also sits to the west of the ridge (Rychert et al., 2018). Neither the body wave model of Byrnes et al. (2017) nor Casc19-S report absolute seismic velocities, but both indicate that asymmetry in the low velocities extend well below 75 km, potentially as deep as 200 km. Furthermore, the lowest velocities in all three models shallower than ∼100 km appear to coincide with Axial Seamount (Fig. 2.10).

Similar asymmetry is not observed beneath the Gorda ridge. Byrnes et al. (2017) and our body wave model show slightly lower velocities beneath the western flank of the Gorda ridge, but low velocities extend to the east all the way to the deformation front. Bell et al. (2016) report velocities beneath the Gorda ridge that are nearly symmetric. This difference in seismic structure between the Gorda and Juan de Fuca ridges is indicative that asymmetry is not a trait shared by all ridges. Additionally, since the Gorda and Juan de Fuca ridges are migrating at a similar rate, the asymmetry is likely not due to ridge migration alone.

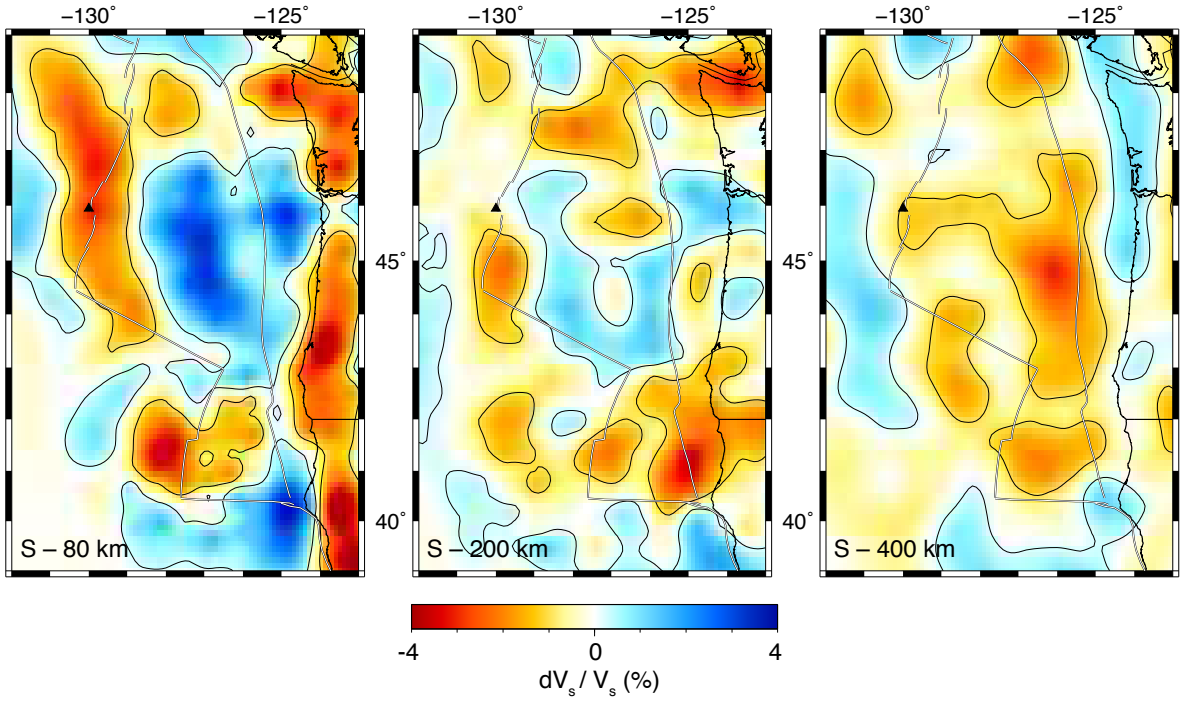

Figure 2.10: Juan de Fuca – Gorda ridge. Casc19-S shows at 80 km (left) a low velocity feature beneath the ridge, strongest at Axial volcano (black triangle), and oriented slightly counter-clockwise from the ridge. There is a rapid transition from low velocities beneath the ridge to high velocities to the east. At 200 km (center), the low velocity feature beneath Axial has shifted slightly southward; by 400 km (right), the low velocities are again situated beneath Axial, perhaps connected to low velocities to the east. Contours are -1% and $+0.25\%$ dV_S.

Akin to the Juan de Fuca ridge, an asymmetric pattern of shear wave velocity and seamount distribution was observed at the East Pacific Rise by the MELT experiment (Mantle Electromagnetic and Tomography; MELT Seismic Team, 1998). Geodynamic studies of that region determined that the migration of the ridge could not entirely explain the asymmetry in seismic velocities (Conder et al., 2002; Toomey et al., 2002). Instead, the asymmetry needs to be controlled by forces within the mantle, either a thermal anomaly, a compositional gradient, or pressure-driven flow (Conder et al., 2002; Katz, 2010; Toomey et al., 2002). In the case of the East Pacific Rise, Conder et al. (2002) suggest that the asymmetry is due to pressure-driven flow as a result of the Pacific Superswell. As Bell et al. (2016) note, there is no superswell close to the Juan de Fuca ridge, so a modest thermal anomaly is their preferred model. The Cobb hotspot provides a source for the thermal anomaly, but Bell et al. (2016) do not image deep enough to image the plume structure, and Byrnes et al. (2017) do not identify any plume-like structures.

Aside from being tomographically imaged, the Cobb hotspot has many features of a typical plume-fed hotspot track. Beginning at the locus of current volcanism, which is Axial Volcano on the Juan de Fuca ridge, a line of seamounts extend to the northwest on the Pacific plate, mirroring the direction of the Pacific absolute plate motion (DeMets et al., 2010). The age of the seamounts within ∼300 km of Axial are progressively younger as they near the active volcanism, indicating that the Pacific plate has been moving at ∼43 km/Ma relative to the source for the last ∼8 Ma (Desonie and Duncan, 1990). Geochemical analyses that extend the profile out beyond 1000 km from Axial volcano indicate that the erupted lavas become more depleted as they approach the ridge, interpreted as progressively shallower melting occurring beneath progressively younger and thinner lithosphere (Chadwick et al., 2014). S-P receiver functions show a velocity increase with depth at the base of the partial melt zone along the whole ridge at ∼90 – 115 km depth, but deeper beneath Axial, at ∼125 – 130 km depth, indicating either elevated temperatures by ∼50°C or elevated hydration by ∼100 ppm (Rychert et al., 2018). Finally, gravity and bathymetry data also suggest that the mantle temperature is 30 – 40°C higher underneath Axial than the rest of the ridge system (Hooft and Detrick, 1995).

Casc19-S shows that Axial Volcano is underlain from 50 – 150 km depth by the lowest velocities of anywhere along the ridge. At 200 km, most of the ridge is underlain by ∼0% dVs, with the exception of a region just south of Axial. By 400 – 500 km, a region of slightly low velocities again underlies Axial. Given the limited resolution of our model in this part of the domain, we cannot confidently identify the existence of a narrow conduit of low velocities in the upper mantle, as might be expected for a mantle plume. But the consistent low velocities that do appear in our model beneath Axial to ∼500 km depth, in contrast to other sections of the ridge, hints at a plume-like structure for the Cobb hotspot.

The second line of evidence for active upwelling comes from the sharp gradient between the low seismic velocities underneath the Juan de Fuca ridge and the high velocities beneath the plate within 200 km of the ridge axis. If the low velocities beneath and to the west of the ridge axis strongly suggest the presence of partial melts, the high velocities underneath the older sections of the plate are consistent with very little melt in the asthenosphere (Bell et al., 2016; Byrnes et al., 2017). This abrupt transition is faster than would be expected by a simple half-space lithospheric cooling model; the interpretation is that the gradient reflects a limb of convective downwelling in response to upwelling beneath the ridge. This downwelling without a significant temperature increase would cause the melt to freeze over a relatively small depth range, ∼10 km (Byrnes et al., 2017; Katz, 2010). In neither Casc19-S, nor in the previously published tomographic models (Bell et al., 2016; Byrnes et al., 2017) does a similarly strong gradient appear underneath the Gorda region, suggesting again that the upwelling is primarily a feature of the Juan de Fuca ridge.

Eilon and Abers (2017) show a strong gradient also in the seismic attenuation structure under the Juan de Fuca plate. They calculate attenuation from teleseismic events such that,

similar to our body-wave models, the absolute attenuation is not preserved, but the relative structure beneath the stations is robust. In their result, Juan de Fuca ridge is characterized by relatively high attenuation, but stations on older Juan de Fuca seafloor show significantly reduced attenuation over less than 200 km, similar to the S-wave velocity structure. This is consistent with narrowly focused melt beneath the ridge, where slightly off-axis teleseismic body waves would not sample, or with an asymmetric melt triangle that extends westward, underneath the Pacific plate. Both of these are consistent with dynamic upwelling beneath the Juan de Fuca ridge. Finally, Eilon and Abers (2017) find that, similar to the tomographic studies, the gradient in seismic attenuation structure is less pronounced beneath the Gorda deformation zone than beneath the Juan de Fuca plate.

The above evidence for active upwelling beneath the Juan de Fuca ridge is robust. The implications for ridge systems globally, however, may be limited. Since ample evidence suggests that there is a hotspot currently beneath the Juan de Fuca ridge, and a narrow conduit is suggested (though certainly not required, given our resolution) by our teleseismic model, we believe the upwelling may be caused, at least in part, by a plume that forms the Cobb hotspot. The presence of this plume implies that upwelling beneath the Juan de Fuca ridge may be driven in part by a local process, rather than being indicative of a global phenomenon beneath ridges.

2.4.1.2 Oceanic Lithosphere-Asthenosphere Boundary

Considering lithosphere farther from the ridge, one remaining question concerns what defines the bottom of the Juan de Fuca plate. Proper characterization of the lithosphere-asthenosphere boundary is of critical importance in understanding the dynamics of tectonic plates and long-term Earth evolution (Craig and McKenzie, 1986; Richards et al., 2001). Imaging the lithosphere-asthenosphere boundary in the oceans remains difficult (Kawakatsu, 2012), but the Cascadia Initiative data provide an opportunity to image this boundary, and to refine our understanding of the chemistry and physics that defines the base of a tectonic plate.

All of the tomographic models described above suggest that within ∼200 km of the ridge, very little melt remains in the asthenosphere (Bell et al., 2016; Byrnes et al., 2017). All of these models have fairly good lateral resolution, but structure that varies vertically is considerably less well constrained. S-P receiver functions, by contrast, image discontinuities in the seismic velocity structure, and are often used to characterize the vertical velocity structure. One such study observed a velocity decrease with depth, which they interpret to be the lithosphere-asthenosphere boundary (Rychert et al., 2018). The impedance contrast is ∼20 km deep beneath the Juan de Fuca and Gorda ridges, and deepens to ∼40 km beneath the oldest seafloor at ∼9Ma. The strength of the signal suggests that a small amount of melt is retained all the way to the deformation front of the subduction zone.

This observation appears consistent with a number of geophysical observations: Seismic reflection/refraction studies show similar discontinuities beneath other oceanic plates (Kawakatsu et al., 2009; Schmerr, 2012; Stern et al., 2015). Magnetotelluric studies show a region of high conductivity and strong anisotropy in the direction of plate motion (Evans et al., 2014; Naif et al., 2013). Surface wave observations from the central Pacific show asthenospheric anisotropy is consistent with a low-viscosity zone at the base of the Pacific plate (Lin et al., 2016). Post-seismic geodetic observations support a layer in the upper asthenosphere with a viscosity of $\sim 2 \times 10^{18}$ to 1×10^{19} Pa-s (Freed et al., 2017; Hu et al., 2016), lower than is estimated for the bulk asthenosphere (Becker, 2017). Geodynamic models show significant melting underneath mid ocean ridges is focused away from the ridge, and metasomatizes the mantle at depths between 20 and 60 km (Keller et al., 2017). Finally, it is consistent with the conceptual model based on Casc16-P (Fig. 3.3), in which a low velocity region beneath the hinge of the subducting plate is interpreted to be the accumulation of partially molten and/or hydrated mantle from the uppermost asthenosphere (Hawley et al., 2016). This low-velocity "roll" was suggested by land-based models (Obrebski et al., 2010; Porritt et al., 2014; Schmandt and Humphreys, 2010; Tian and Zhao, 2012), and may be visible in receiver functions (Rychert et al., 2018) and surface wave tomography (Bell et al., 2016). The existence of this feature would have implications for both global tectonics and local megathrust kinematics (Bodmer et al., 2018). A complete discussion of the nature and implications of the low-velocity roll we observe in the Casc16-P is given in Chapter 3.

Reconciling the hypothesized mechanically weak, seismically slow, and electrically conductive layer with the body-wave and surface-wave models is not problematic—a thin, low-velocity layer would be difficult to detect using these methods (Bastow, 2012). Reconciling the two conceptual models derived from these images, however, will require more careful analysis. One conceptual model envisions ridge flank downwelling leading to melt freezing within $\sim$200km of the ridge; the other envisions retained melt and/or volatiles maintaining a mechanically weak layer that defines the base of the tectonic plate.

More precise knowledge of the seismic anisotropy would help elucidate the properties of this mechanical boundary layer. Two shear wave splitting studies report azimuthally anisotropic fast directions that largely reflect the absolute plate motion beneath the Juan de Fuca plate, but beneath the Gorda section, the anisotropic fabric tends to align with the Pacific plate motion (Bodmer et al., 2015; Martin-Short et al., 2015). Martin-Short et al. (2015) and Bodmer et al. (2015) suggest that the Gorda section is too small to have an effect on mantle flow beneath it, while the broader Juan de Fuca plate is large enough. The anisotropy that is derived from surface waves has higher error, but suggests that much of the anisotropy is deeper than $\sim$150 km (Bell et al., 2016). A careful shear wave splitting analysis revealed two layers of anisotropy: one in the hinge that suggested trench parallel flow, and one deeper that was trench normal (Russo, 2009). The deep trench-normal component is similar to what was seen in these larger studies, but the shallower layer of trench-parallel flow is consistent with material in the roll being extruded laterally, to the north and south.

A fully three-dimensional model of the orientation and magnitude of seismic anisotropy may allow for a better characterization of the viscosity structure, and may elucidate the cause of the oceanic lithosphere-asthenosphere boundary.

2.4.2 Structure of the Juan de Fuca slab and surrounding mantle

One of the most unusual aspects of the Cascadia Subduction Zone is the lack of regular earthquakes on the interface. While the sediment record indicates that it is capable of generating magnitude ∼9 earthquakes (Goldfinger et al., 2012), very few small-to-intermediate magnitude earthquakes have been instrumentally recorded. I will briefly discuss four closely linked areas of research regarding the Cascadia Subduction Zone: the structure of the incoming plate, processes along the megathrust interface, morphology of the downgoing slab in the upper mantle, and the mantle flow induced by this system. Our tomographic models place direct constraints on only the final two, but all four are linked closely enough that we can infer details about the shallow processes as well. Describing and linking these different systems is of considerable value to seismic hazard and scientific communities.

2.4.2.1 Incoming Plate Structure

One of the most important unsolved questions about the incoming plate is the hydration state of the crust and lithospheric mantle. Hydration is thought to play a role in plate boundary processes (Audet and Kim, 2016; Bostock et al., 2002; Preston et al., 2003; Rogers and Dragert, 2003), so the amount of water that is delivered to the subduction zone by the incoming plate should have an effect on these processes.

Active source seismic studies have placed the tightest constraints on the amount of water bound in the subducting Juan de Fuca plate. Much of this hydration is expected to occur in the region just seaward of the deformation front, where the plate experiences faulting as it bends prior to being subducted. Seismic reflection studies show that these normal fault structures extend over a large area, more than 200 km from the deformation front (Han et al., 2016; Nedimović et al., 2009). Despite the lateral extent of faulting, both the spatial density of faults and the throw on each fault is comparatively low (Nedimović et al., 2009), and the faults are generally confined to the upper crust, with very limited faulting through the Moho (Han et al., 2016). This is perhaps unsurprising, given that prior to subduction, the oldest portions of the plate are only ∼9 Ma (Wilson, 2002), still quite warm, and therefore the brittle-ductile transition should still be quite shallow. Perhaps as a result, while the upper crust is mildly hydrated (up to 4 wt% water), deeper seismic velocities are consistent with an essentially dry (less than 0.5 wt% water) lower crust and lithospheric mantle (Canales et al., 2017; Horning et al., 2016).

Propagator wakes are a prominent exception to the low water content of the lower crust and mantle. Propagator wakes are structural complexities on the Juan de Fuca plate that

are inherited from segments of the ridge system where two spreading centers overlap (Hey, 1977; Wilson, 1990). Gravity suggests these regions have denser and thinner crust than the surrounding plate (Marjanović et al., 2011). Seismic reflection studies have found that these regions have seismic velocities that are consistent with more hydrated (up to 2 wt% water) lower crust and lithospheric mantle (Canales et al., 2017; Horning et al., 2016).

2.4.2.2 Intra-slab seismicity and megathrust interface

With no great earthquakes instrumentally recorded on the Cascadia Subduction Zone, we must investigate the interface through other methods. Through the analysis of turbidite deposits, Goldfinger et al. (2012) have determined that full-margin rupture events occur every ∼500 years, with smaller megathrust events happening more regularly on smaller sections of the interface. What controls the edges of the sections is not well understood. We will return to the issue of a segmented subduction zone in section 2.4.3. Plate structure globally has been seen to correlate with seismicity (Bilek, 2010), and data in Cascadia seem to fit in this picture. Smaller seismicity, though sparse, does appear to correlate both with features on the Juan de Fuca plate, such as inferred subducted seamounts (Tréhu et al., 2012), and with structure of the North American plate, like the Siletz terrane (Tréhu et al., 1994).

Study of seismicity has led also to independent constraints on the hydration of the incoming Juan de Fuca plate. Episodic tremor and slip is the coincident occurrence of nonvolcanic tremor and geodetically observed slip on the plate interface, just downdip of where megathrust earthquakes take place (Rogers and Dragert, 2003). It is thought to be driven by increased pore fluid pressure driven by water that is brought into the subduction zone by the incoming oceanic plate (Audet and Kim, 2016). Farther downdip, intermediate-depth intraslab seismicity is also hypothesized to be the result of dehydration of the subducted slab, where two clearly separate groups of seismicity reflect two dehydration processes: serpentinization of the mantle and eclogitization of the crust (Preston et al., 2003). The simple fact that these types of events occur is evidence that the incoming Juan de Fuca plate is somewhat hydrated (Abers et al., 2009).

Work to image the plate interface has also revealed evidence for a hydrated Juan de Fuca slab. Scattered seismic phases show a zone of low seismic velocity along the plate interface, which is interpreted to be a region of high pore fluid pressure and hydrated mineral assemblages (Audet et al., 2009; Delph et al., 2018; Hansen et al., 2012; Janiszewski and Abers, 2015). This zone matches low velocities observed in surface wave studies (Bell et al., 2016; Gao, 2016, 2018). Scattered wave imaging farther inland suggests a cold and highly serpentinized mantle wedge (Bostock et al., 2002), caused by dehydration of the Juan de Fuca plate. Similarly, a strong aeromagnetic anomaly that is not coincident with a gravity anomaly suggests a serpentinization in the mantle wedge, a process that lowers the density and creates magnetite (Blakely et al., 2005). Finally, a region of high electrical conductivity

matches low velocities along the interface and within the mantle wedge (Evans et al., 2014), further supporting the idea of hydration throughout this area.

It is possible that a hydrated upper crust as seen in offshore active source seismic studies (Canales et al., 2017; Han et al., 2016; Horning et al., 2016) is enough to cause elevated pore pressures along the entire Cascadia margin. Additionally, regions of elevated intermediate depth seismicity lie along the expected locations of hydrated propagator wakes (Nedimović et al., 2009). But reconciling deeper and large-scale hydration signatures (Bostock et al., 2002; Chen et al., 2015; Gao, 2018) with a dry Juan de Fuca lithospheric mantle (Canales et al., 2017; Horning et al., 2016), and linking that hydration signature with the chemistry of lavas erupted at arc volcanic centers (Plank et al., 2013; Walowski et al., 2015) will require significant future study. The hydration state of the slab and mantle wedge play an important role not only in seismicity in this region, but also in the structure of the downgoing slab and the dynamics of the interaction of the slab and the surrounding mantle.

2.4.2.3 Juan de Fuca slab morphology

It has long been recognized that the shape of the subducted Juan de Fuca slab is unusual, and can reveal aspects of the history of subduction along the Cascadia margin (van der Lee and Nolet, 1997; Obrebski et al., 2010; Roth et al., 2008; Sigloch et al., 2008; Xue and Allen, 2007). Two aspects of the slab are of particular note: nowhere does the slab clearly extend deeper than 600 km, or eastward of ∼118°W; and in the central portion from roughly 44°N to 46°N, the slab terminates shallower than 250 km depth, perhaps as shallow as 150 km (Fig. 2.7). Although these have been given various, and sometimes overlapping, names in the literature, here we will call the former the "slab gap" and the latter the "slab hole."

Subduction along the western margin of North America has been continuous for the last ∼150 Ma (Severinghaus and Atwater, 1990). It would not be unreasonable to expect a correspondingly long high-velocity body beneath North America, reflecting the subducted Farallon slab, extending all the way to the current Cascadia Subduction Zone. Indeed, high velocities are imaged beneath eastern North America, interpreted to be the remnant Farallon slab (van der Lee and Nolet, 1997; Porritt et al., 2014; Schmandt and Lin, 2014). But these high velocities are not connected to the Juan de Fuca slab. The gap that exists between the Juan de Fuca slab and the remnant Farallon slab must follow from either a complexity in subduction at ∼20 – 40 Ma (Obrebski et al., 2010; Sigloch et al., 2008), or a fragmentation of the slab post-subduction.

Given its proximity to ongoing subduction, the slab hole is likely a more recent phenomenon. Although some authors argued that the hole was an artifact of tomographic inversions due to low velocities in the mantle wedge that were situated immediately adjacent to the high-velocity slab (Roth et al., 2008), consensus has been built that this is a real feature. It is worth noting that a scattered wave imaging study also resolves the hole (Cheng

et al., 2017); since this method is sensitive to sharp vertical velocity gradients, the low velocities in the mantle wedge above the plate would be imaged as a strong impedance contrast. A lack of impedance contrast further supports the hole as a real absence of high-velocity slab. Authors have interpreted this hole as either a section of the slab that was destroyed by the Yellowstone plume (Obrebski et al., 2010), "complex subduction" (James et al., 2011; Schmandt and Humphreys, 2010), and dynamic pressure gradients in the mantle beneath the slab (Liu and Stegman, 2011). Whatever the cause, the lack of slab in this region will reduce the "slab pull" force, and affect seismicity along the Juan de Fuca–North America plate interface.

While we do not speculate about the initial cause of the hole in the slab, we do remark that two features are spatially coincident with the southern edge of the hole. First, a propagator wake, generally viewed as a region of weakness in an oceanic plate (Canales et al., 2017; Horning et al., 2016; Nedimović et al., 2009), extends from the Gorda deformation zone to the southernmost edge of the slab hole (Wilson, 2002). Second, anomalous age-progressive volcanism in Oregon, known as the High Lava Plains (Jordan, 2005), are situated above the southernmost portion of this hole. We suggest that the hole in the slab is a tear that is migrating updip along this zone of weakness, and that the age-progressive High Lava Plains volcanism is the result of mantle flow focused through the tear. This causes the southernmost portion of the slab to rotate clockwise, and accelerates the deformation in the Gorda deformation zone. We will discuss this process and its implications for the demise of oceanic plates in more detail in Chapter 4.

2.4.2.4 Subduction-induced mantle flow

The subducting Juan de Fuca slab plays an important role in the geometry of mantle flow underneath western North America. To first order, the coherent Juan de Fuca slab is undergoing rollback, meaning that the trench is migrating westward, toward the Juan de Fuca ridge.

Shear-wave splitting patterns to the south and east of the subduction zone show a large-scale arcuate pattern centered under Nevada, roughly coincident with the southeasternmost edge of the Gorda slab (Zandt and Humphreys, 2008). This has been interpreted as toroidal flow around the edge of the sinking slab, and has been observed in numerical simulations (Jadamec and Billen, 2012; Stegman et al., 2006). It has also been interpreted as flow induced by a lithospheric drip (West et al., 2009), but the high P-wave velocity feature hypothesized to be the sinking lithosphere is of limited extent in other models (Porritt et al., 2014; Schmandt and Humphreys, 2010) and in Casc16-P and Casc19-S, so we prefer an origin that does not originate with the sinking North American lithosphere.

Shear-wave splitting directly to the east of the subduction zone shows a pattern that is largely perpendicular to the Cascadia deformation front. Close to the coast, the mantle

wedge is so thin that the splits are thought to reflect entrained mantle flow beneath the slab as it descends into the mantle toward the east (Eakin et al., 2010). This is consistent with splits offshore showing mantle flow that reflects absolute Juan de Fuca plate motion (Bodmer et al., 2015; Martin-Short et al., 2015), but is in contrast to other subduction zones that are undergoing rollback, where the slab forces flow in the sub-slab mantle that is parallel to the trench (Russo and Silver, 1994). Farther inland, the east-west splits are believed to reflect flow in the mantle wedge (Long et al., 2009). The flow here is interpreted to be toward the west in the shallow part of the wedge, filling in the region in the corner of the mantle wedge as the slab retreats to the west, and then toward the east where it is entrained by the slab at the bottom of the wedge (Druken et al., 2011). This flow geometry has been used to explain the dry basalts and age-progressive rhyolites in the High Lava Plains (Ford et al., 2013; Long et al., 2012; Till et al., 2013).

While it is clear that the Juan de Fuca slab is undergoing rollback, and this is a primary driver on mantle flow in the region, the fragmented nature of the Juan de Fuca slab in the upper mantle led us to reconsider the exact nature of its influence. As we mentioned in section 2.4.2.3, and will discuss in chapter 4, flow in the mantle could be focused up through the hole in the central part of the slab, leading to decompression melt and volcanism. A full description of how holes in slabs affect flow in the mantle, both in Cascadia and elsewhere (e.g., Portner et al., 2017) will require fully three-dimensional numerical modeling, which is outside the scope of this work.

In addition to the ways in which the slab may affect flow in the mantle, it is worth considering the ways in which the mantle may affect the dynamics and morphology of the slab. For example, the Yellowstone-Snake River Plain age-progressive volcanic track has been interpreted as a mantle plume (Camp and Ross, 2004). It has long been recognized that the mantle plume must have interacted with the subducting Juan de Fuca plate before it arrived at the surface of the North American plate (Geist and Richards, 1993; Xue and Allen, 2007). Indeed, some authors have argued that the Yellowstone plume is the cause of the hole in the Juan de Fuca slab (Obrebski et al., 2010). Others still have argued that the Yellowstone/Snake River Plain volcanism is not due to a plume at all, but rather is driven by upwelling around the edges of sinking Juan de Fuca slab fragments (James et al., 2011). Placing the fate of the Juan de Fuca slab in the larger regional context of a complicated and active mantle is the subject of significant ongoing debate. We will discuss this more in section 2.4.4.

There exist many unsettled problems over a range of scales in regards to the present-day interaction between the Juan de Fuca and North American plates, and the role that the mantle plays in that interaction. The tomographic models shown here, with improved resolution to the west as a result of offshore observations, have allowed us to characterize in particular two major features: a low-velocity "roll" beneath the slab hinge, and a hole in the slab itself. Both of these features are important for constraining global-scale tectonics. But

they are also both important for understanding the local dynamics that govern this complicated region, from regional-scale phenomena like mantle plumes, to small-scale phenomena like stress on the megathrust interface.

2.4.3 Segmentation of the Cascadia Subduction Zone

One of the themes that underlies many of the observations discussed in section 4.2 is that of variability along the strike of the subduction zone. In many datasets, the characteristics can be divided into three segments, with boundaries at roughly 43°N and 46.5°N (Fig. 2.11). It is worth considering whether the segments in different datasets are related, and if they are, what is the underlying cause of these boundaries.

It is sensible to begin this exploration at the surface, in our case, at the megathrust interface. Turbidite deposits record the history of the last ∼10,000 years of large earthquakes on the Cascadia megathrust, and suggest that there are three distinct rupture modes (Goldfinger et al., 2012). Although there is significant inherent uncertainty in the precise rupture extent of each event, the 41 recorded turbidites fall into three categories: 19 – 20 events of full margin rupture, three to four events that rupture the margin south of roughly 46°N, nine that rupture the margin south of ∼44°N, with the remaining events being restricted to the extreme southern end of the interface. Based on the number of events in each segment, the southern segment boundary at ∼44°N appears to be more significant. Goldfinger et al. (2012) note that the time scale is long enough to consider these segments structurally controlled. We can imagine four possible factors that would affect the frictional environment on the plate interface: the structure of the incoming plate, the structure of the overriding plate, sedimentary or fluid structures that mediate the contact between the two plates, and forces that act on the interface. I will address these observations in three sections: those that originate from offshore, those that detail segmentation on the plate interface itself, and those that suggest segmentation beyond the interface.

2.4.3.1 Offshore segmentation

Juan de Fuca seamounts at the plate interface have been shown to affect smaller ($M < \sim 5$) seismicity (Tréhu et al., 2012), so it follows that these could encourage or inhibit rupture of larger earthquakes. The inferred locations of these seamounts, approximately 44.5°N, are approximately coincident with the southern boundary reported by Goldfinger et al. (2012), but no inference has been made about seamounts at 46°N. It is possible, therefore, that the existence of a seamount at ∼44.5°N creates a barrier that inhibits ruptures. Given that the seismogenic zone is likely not wider than 80 km (e.g., Audet and Kim, 2016), and the plate convergence rate is ∼35 km Ma^{-1} (Wilson, 1993), a seamount would cause a segmentation boundary for only 1 – 2 Ma.

The Blanco Fracture Zone has very little bathymetric expression at the deformation front,

and is not coincident with either segment boundary, so likely plays little role in segmentation at present. Subducted pseudofaults may also cause heterogeneity along the interface, by virtue of either their thinner and denser crust (Marjanović et al., 2011) or higher water content (Canales et al., 2017; Horning et al., 2016; Nedimović et al., 2009), or both. The largest of these runs roughly between 44°N and 45°N at seismogenic depths (Wilson, 2002), and so could be related to the southern segment boundary. There is, however, no obvious correlation between the other two subducted pseudofaults, at roughly 42.5°N and 47°N at seismogenic depths (Wilson, 2002), and the suggested boundaries.

Furthermore, a seismic reflection profile crosses the Juan de Fuca plate parallel to the deformation front just offshore of the northern segment boundary, from roughly 44°N to 48°N, but along-strike variations in the hydration states of either the crust or the mantle are not obviously associated with this boundary (Canales et al., 2017). In general, faulting internal to the Juan de Fuca plate seems to decrease northward. The Gorda plate experiences regular intraplate earthquakes, and is highly deformed and likely faulted (Chaytor et al., 2004; Wilson, 1989). Seismic reflection profiles also show more pervasive faulting off the coast of Oregon (∼45°N to 46°N) than Washington (∼47°N to 48°N) (Han et al., 2016). The northern limit of the highly faulted Gorda deformation zone is only ∼42°N (Wilson, 1989), and the data off Oregon and Washington are inadequate to identify an abrupt transition in faulting style there (Canales et al., 2017; Han et al., 2016; Horning et al., 2016).

Two offshore datasets do show segment boundaries roughly aligned with those inferred from turbidite data: sediment thickness and gravity. Sediment thickness generally increases from south to north, but two large sediment packages—more than 1.5 km thick, and potentially as thick as 3 km—are associated with the Astoria and Nitinat fans (Bell et al., 2016; Divins, 2003; Goldfinger et al., 2012). The Astoria fan in particular is situated directly in between these segment boundaries; the southern edge is around 44°N, and the northern edge is ∼46.5°N. Sediment could affect the interface in three ways: they could insulate the incoming plate, so that it is less hydrated (Bell et al., 2016); they could insulate the slab so that it dehydrates deeper (Delph et al., 2018), or it could smooth out asperities on the interface and lead to a more homogeneous stress state (Ruff, 1989).

In a number of subduction zones worldwide, including Nankai, the Aleutians, and Chile, prominent free-air gravity lows coincide with bathymetric lows situated just inboard of the subduction zone, and coincide with regions of large coseismic slip (Wells et al., 2003). Wells et al. (2003) propose that the bathymetric lows are indicative of permanent subsidence (i.e., subsidence that is not recovered coseismically) caused by subduction erosion. Although these features are offshore, they imply that the overriding plate largely controls the rupture modes of the megathrust. Five of these so-called 'deep sea terrace lows' exist in the Cascadia Subduction Zone. The largest extends from 45°N to 47°N, centered on the northern segmentation boundary. The southern boundary sits just between the two southernmost gravity lows. It is worth noting that just east of these gravity lows sits a region of very high free-air

gravity, corresponding to the Siletz terrane (Tréhu et al., 1994). We discuss terranes of the overriding plate in the following section.

2.4.3.2 Interface segmentation

In addition to the extent of rupture of large magnitude earthquakes, other processes on the subduction interface exhibit similar segmentation boundaries. Just downdip of the locked seismogenic zone is where episodic tremor and slip occurs (Rogers and Dragert, 2003). While episodic tremor and slip events happen all along the strike of the Cascadia Subduction Zone, the recurrence intervals of the events fit neatly into three geographic regions: south of ∼43°N, the recurrence interval is ∼10 months; north of ∼46.5°N, the recurrence interval is ∼14 months, and in between, the recurrence interval is ∼19 months (Brudzinski and Allen, 2007). Since these slip events occur at about 40 km depth on the interface, Brudzinski and Allen (2007) also show that the North American topography above the 40 km depth contour of the slab exhibits variability in the same scale—high topography in the north and south, and low topography in between the segmentation boundaries seen in the recurrence intervals. The topography largely correlates with geologic terranes, so Brudzinski and Allen (2007) have termed these sections, from south to north, Klamath, Siletzia, and Wrangellia.

The central structure, the Siletz terrane, is the most noteworthy because it exhibits very different seismic characteristics from the other two. Siletzia is an accreted oceanic terrane, with much higher seismic velocities than the forearc structures to the north or the south (Delph et al., 2018; Porritt et al., 2011; Tréhu et al., 1994). It is thicker and stronger than the other forearc crust, which likely plays a role in decreased forearc seismicity recorded in central Oregon (Tréhu et al., 1994), and it may extend deep enough to reach the plate interface. This could lead to along-strike differences in thermal structure, porosity structure, or both.

Indeed, along the interface where episodic tremor and slip occurs, a low velocity zone has been observed by scattering wave techniques, generally interpreted to be the result of fluids along the interface (Audet et al., 2010; Bostock, 2013; Hansen et al., 2012). This zone is much thinner beneath Siletzia, and seems to correlate better with the extent of Siletzia than with anything offshore (Delph et al., 2018). Delph et al. (2018) suggest that the thicker forearc crust hinders subduction of sediments, and allows for lower pore fluid pressures. The state of fluids along the interface is important not just for episodic tremor and slip, but ultimately also for megathrust earthquakes (Tan et al., 2012).

Finally, GNSS observations (Schmalzle et al., 2014) and tidal and leveling observations (Burgette et al., 2009) show along-strike variations in the uplift as a result of interseismic strain. In the Klamath and Wrangellia sections, vertical velocities along the coast tend toward 4 mm yr^{-1} of uplift; in Siletzia, uplift is 1 mm yr^{-1} or less. Thus it appears likely

that Siletzia directly controls segmentation of forearc topography, seismicity, and interseismic deformation, episodic tremor and slip, and plate interface structure.

2.4.3.3 Deeper segmentation

Segmentation of the subduction zone does not end at the downdip edge of the plate interface. Just downdip of the interface, scattered wave imaging shows a strong impedance contrast along the interface, representing the low velocity oceanic crust underlying the faster forearc lithosphere. This impedance contrast disappears beneath the continental Moho discontinuity, implying a seismically slow, and likely serpentinized forearc mantle (Bostock et al., 2002). An aeromagnetic study also determined that the strongest aeromagnetic anomaly was situated to the east of the largest gravity anomaly (Blakely et al., 2005), which is unusual, since most rocks that produce a strong magnetic signal are also relatively dense. Blakely et al. (2005) concluded that a region that is characterized by low densities and high magnetic anomaly was likely due to a highly serpentinized mantle wedge, since serpentinization both lowers densities and produces magnetite. This signal is observed in both the Wrangellia and Siletzia regions, but not in the Klamath.

The dehydration reactions that lead to serpentinization also lead to intermediate depth intraslab earthquakes (Preston et al., 2003). It follows that intermediate depth earthquakes should correlate with the aeromagnetic evidence for serpentinization, but they do not. Intraslab earthquakes are frequent in the northern Wrangellia section, and have been associated with a large propagator wake (Nedimović et al., 2009). But intraslab events are virtually nonexistent in the central section, where extensive serpentinization is inferred. Furthermore, intraslab seismicity again increases in density south of ∼42°N or 43°N, but the aeromagnetic anomaly decreases in amplitude significantly in this region. Blakely et al. (2005) argue that this may be the result of a difference in the 'slab pull' force along strike.

As discussed in section 2.4.2.3, there is a gap in the high velocities that define the slab, whose northern and southern edges roughly coincide with the segmentation boundaries identified in so many other datasets. It is possible that the absence of slab would drive a reduction in seismicity, although given the oblique subduction angle of the Juan de Fuca plate, it is not immediately obvious where the reduction in seismicity would be: would it be immediately updip, as might be expected if the negative buoyancy of the slab were the controlling factor on the seismicity? Or would it be along the direction of plate motion, centered updip and southwest of the hole, as might be expected if traction and the strength of the slab played an important role in the process of generating seismicity? Modeling the stress field within the subducted lithosphere is beyond the scope of this work, but it is within the realm of possibility that the slab hole drives at least some of the segmentation observed farther updip in the subduction zone. The geometry of subduction does, however, make it more difficult to envision how the observed segmentation at the megathrust interface could have contributed to the hole. When the slab at ∼200 km depth was at the surface, it was situated signif-

icantly to the south relative to the segmentation boundaries as observed in the overriding North American plate.

Four-way segmentation in arc chemistry has been reported using strontium and neodymium isotopes (Schmidt et al., 2008). The south segment, south of 42°N, is characterized by basalts that reflect high melt and high flux, associated with the slab window. The central segment, which extends from 42°N to just south of Newberry volcano (Mitchell and Asmerom, 2011) at ∼43.5°N, reflects extension and high heat flow from the Basin and Range province, while the Columbia segment, from ∼43.5°N to Mount Rainier just south of 47°N, largely reflects a mantle signature from oceanic terranes. The final section to the north of Mount Rainier reflects small degrees of flux melting.

Heat flow data collected from thermal springs throughout the Pacific Northwest display significant along-strike variability, as well (Ingebritsen and Mariner, 2010). The forearc to the south of ∼42.5°N and north of ∼47°N is characterized on average by ∼40 – 60 W m^{-2}, but in between these segmentation boundaries, largely consistent with the Siletz terrane, heat flow is everywhere less than 40 W m^{-2}. Within the United States section of the Cascade Arc itself, fully 95% of heat flow (∼1000 out of 1050 W m^{-2}) occurs south of 45.25°N, i.e., between northern California and northern Oregon. This is ∼150 km south of the morphological change in volcanic edifices that occurs north of Mount Rainier, but is generally consistent with a step in back arc heat flow, which is characterized by ∼50 – 70 W m^{-2} to the north, and ∼70 – 100 W m^{-2} to the south. Ingebritsen and Mariner (2010) attribute the changes in heat flow in the arc and backarc to the Basin and Rage province, while the forearc is presumably due to the nature of the different terranes.

Surface wave imaging shows velocity variations in the backarc consistent with the heat flow and segmentation boundaries. A transition from low velocities in the south to high velocities in the north occurs at ∼46°N to 47°N (Gao, 2018; Porritt et al., 2011), likely also owing to Basin and Range extension.

Finally, the mantle beneath the subducting slab has also been argued to show variability along strike (Bodmer et al., 2018). This is the same low-velocity anomaly that was observed by Hawley et al. (2016), who observe little along-strike variation. Bodmer et al. (2018) suggest that these low velocities, which are strongest south of 43.5°N and north of 46°N, are caused by two separate regions of upwelling beneath the Juan de Fuca plate. They contend that the increased buoyancy from these features changes the state of stress on the megathrust interface, influencing locking of the megathrust and tremor occurrence. Delph et al. (2018) further argue that this buoyancy may change the shape of the slab, increasing bend faulting in the northern and southern regions, creating more fluid pathways and affecting episodic tremor and slip recurrence intervals.

While this is an interesting hypothesis, we question whether the segmentation in the

model of Bodmer et al. (2018) is real, or is in fact an artifact of their inversion technique. As discussed in section 2.2.3, teleseismic body wave models cannot resolve structure immediately beneath the stations that are used in the inversion. In the models presented here, Casc16-P and Casc19-S, we solve for a station correction that attributes as much signal as possible to the crust beneath the station, removing that signal from every delay, and only inverting for signal that is required by the data to be in the mantle. Bodmer et al. (2018) take a different, complementary approach—they use a crustal model *a priori* to remove these crustal signals, and solve for the remaining delay at each station. If the crustal model is correct, then this approach will give a more accurate view of velocities in the mantle. If, however, the crustal model has any inaccuracies built into it, those inaccuracies will be mapped to mantle depths, and misinterpreted as structure. It is difficult to quantify the uncertainty in a starting crustal velocity model.

The gap in low velocities as imaged by Bodmer et al. (2018) sits directly beneath the Siletz terrane. If the crustal model underestimates the velocities in Siletzia, body waves will pass through the forearc crust faster than expected, and that negative delay will be mapped to shallow mantle depths. It is surprising that our model, whose artifacts should tend toward 0% dVP, shows a largely consistent low-velocity anomaly along strike, while Bodmer et al. (2018) show a gap in these low velocities that is coincident with a known region of high crustal forearc velocity.

2.4.3.4 What causes segmentation?

Sorting through this immense list of datasets that show along-strike segmentation to try to find a single cause has proven to be a challenging exercise. We do not believe there to be one single cause. What follows is a summary of what we believe to be plausible segmentation cause and effect.

We begin by acknowledging that variations in the incoming plate structure do not seem to be a strong candidate. Propagator wakes are not large enough or oriented properly to account for variability of processes on the interface, and outside of the propagator wakes, the lower crust and upper mantle of the incoming plate appear uniformly exceptionally dry (Canales et al., 2017; Han et al., 2016; Horning et al., 2016). Seamounts are not long-lived enough to have altered signatures in the mantle wedge, arc, and back arc.

It is possible that one propagator wake has become a tear in the subducting slab (Hawley and Allen, 2019), that this feature causes variability in the intraslab seismicity (Blakely et al., 2005), and conceivably on the state of stress along the plate interface. Upwelling through this hole could also partially explain the distribution of low velocities in the backarc (Gao, 2018; Porritt et al., 2011), and the enhanced heat flow in the central segment of the Cascade arc (Schmidt et al., 2008). But ultimately we cannot identify a model in which this tear could explain many of the forearc and offshore segmented datasets, such as deep sea terrace

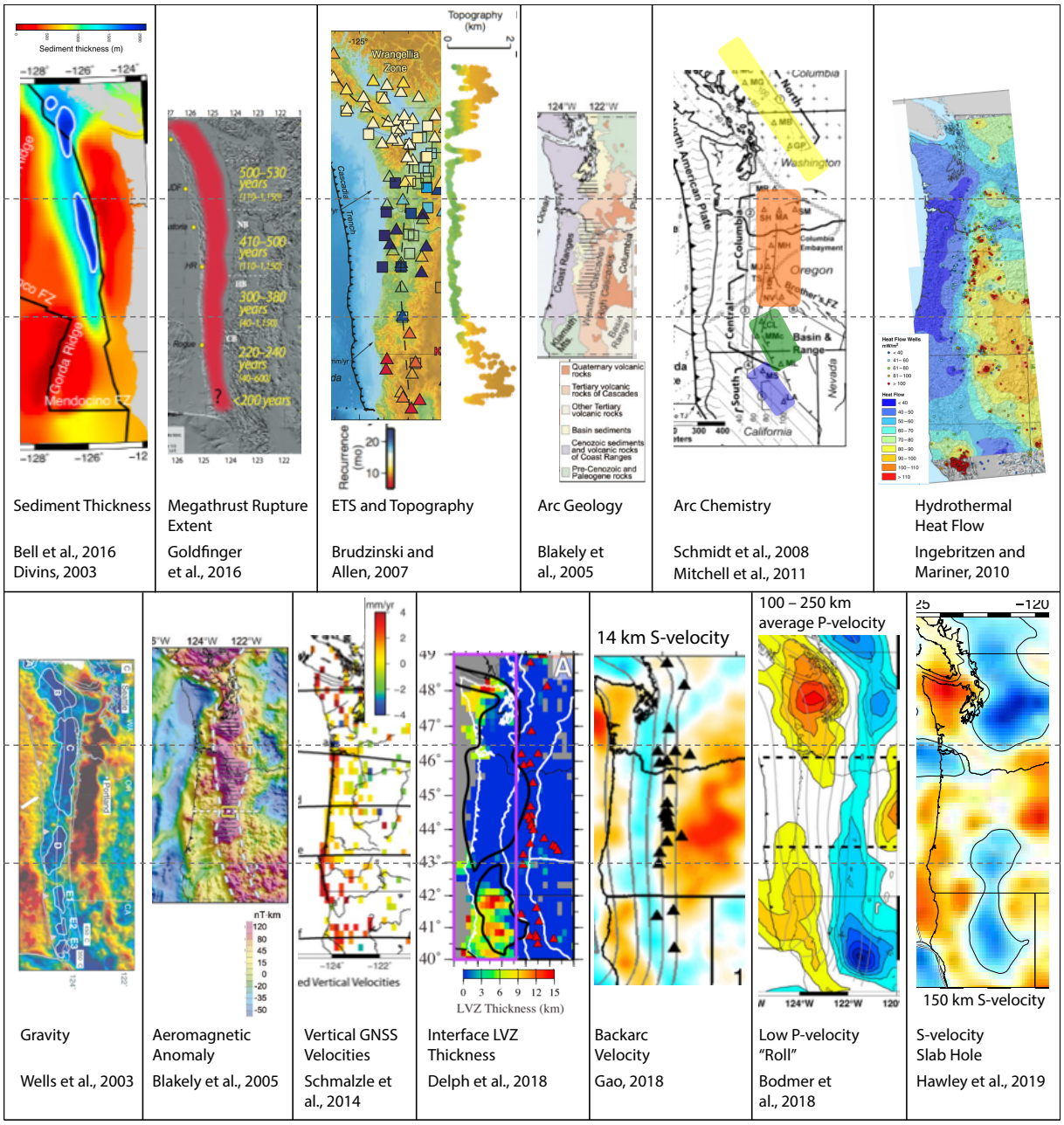

Figure 2.11: Segmentation of the Cascadia Subduction Zone. We present previously published datasets, discussed in the text, that show segmentation boundaries along strike of the Cascadia Subduction Zone. Two segmentation boundaries at roughly 43°N and 46.5°N (grey dashed lines) can be seen in almost every dataset. The data presented in each panel is labeled below the figure. For a complete discussion of the features in each panel, the reader is directed to the references in which the figures were originally published.

lows (Wells et al., 2003), vertical GNSS velocities (Schmalzle et al., 2014), forearc heat flow (Ingebritsen and Mariner, 2010) and topography (Brudzinski and Allen, 2007), and offshore sediment structure (Divins, 2003).

Ultimately, we believe that segmentation of the subduction zone is likely a coincidental alignment of two phenomena: the Siletz terrane, and the Basin and Range province. Two additional unrelated phenomena may play a secondary role: the deep slab structure, and low velocities in the slab hinge.

The Siletz terrane is a thick, strong crustal forearc block extending nearly to the plate interface, and its internal structure and its interaction with the subducting plate could easily account for all the offshore datasets; the interface structure, seismicity, and episodic tremor and slip recurrence; and the chemistry of arc volcanos. The Basin and Range must play a major role in the segmentation of the arc and backarc by nature of its high temperature and high melt content (Schmandt and Humphreys, 2010).

The hole in the slab is a robust feature, and it is intriguing that its segmentation boundaries coincide with the boundaries considered above. It is not obvious how any of the above processes could cause the hole or an artifact that looks like the hole. It is possible that the hole contributes to the stress state within the slab and on the slab interface, though perhaps only a second-order effect.

The segmentation of the low velocity anomaly in the slab hinge could also contribute to segmentation of the interface stress state (Bodmer et al., 2018; Delph et al., 2018). Similar to the hole, there is no reason to expect its segmentation to reflect that of the other datasets presented here. Unlike the slab hole, however, the segmentation in the low velocity "roll" may reflect improperly mapping forearc structure—where segmentation is documented—to mantle depths. More work will need to be done to resolve whether this is a real feature.

2.4.4 Mantle beneath western US

An impressive number of tomographic models have been made of the western United States in the last decade (e.g., Ekström, 2014; James et al., 2011; Obrebski et al., 2010, 2011; Porritt et al., 2014; Schmandt and Humphreys, 2010; Schmandt and Lin, 2014; Sigloch, 2011; Tian and Zhao, 2012; West et al., 2009). The tomographic models Casc16-P and Casc19-S are significant advances over these models in that they include data from offshore—leading to better resolution of subduction zone processes, and the ability to resolve at all the offshore structure. They do not change our knowledge of present seismic velocity structure west of the subducting Juan de Fuca slab. But we will discuss this region briefly, both because our model extends into this region, and because the Cenozoic evolution of the western United States has been driven in no small part by the Farallon/Juan de Fuca subduction system.

The largest and most significant feature in the western United States is the large swath of anomalously low velocity that underlies virtually the entire Basin and Range province. While P-wave and S-wave velocities are both low, the S-wave velocities are particularly low, such that V_P/V_S is relatively high, which has been interpreted as pervasive high temperatures and partial melt (Schmandt and Humphreys, 2010). This observation, along with uplift that continues to the present (Karlstrom et al., 2012), is strong evidence for an actively convecting mantle. Whether this convection is small scale, in response to lithospheric processes (Levander et al., 2011), or whether this is the result of a deep-seated, long-term feature of active convection within the mantle (Moucha et al., 2009; Rowley et al., 2016) remains a subject of debate.

Within and surrounding this low-velocity Basin and Range province are numerous small high velocity features. All of these features have been interpreted variously as either remnant slabs, or as lithospheric delaminations/drips. If the latter is the case, it provides important constraints on the evolution of continental lithosphere—specifically under what ambient mantle conditions old, cold, dense continental lithosphere weakens enough to become gravitationally unstable, and sink through the mantle. If, however, these are all slab remnants, it would simply be further evidence for complex Cenozoic era subduction in the western United States.

Two features to the west, the Transverse Ranges anomaly and the Isabella Anomaly, have been interpreted as lithospheric instabilities (Humphreys and Hager, 1990; Zandt et al., 2004), but because offshore magnetic lineations that suggest captured microplates line up with these anomalies, a reasonable null hypothesis for these high velocity features is that they represent stagnant slabs (Nicholson et al., 1994; Wang et al., 2013). The Wallowa anomaly is immediately adjacent to the Siletzia Curtain to the north of the Basin and Range, and these two high-velocity bodies cannot be easily discerned from one another in some velocity models (e.g., Roth et al., 2008), including ours. The Wallowa anomaly has been interpreted as a lithospheric instability (Darold and Humphreys, 2013; Hales et al., 2005), but the Siletzia has been interpreted to be either a remnant slab (Schmandt and Humphreys, 2010) or an intact batholith (Roth et al., 2008). Lastly, the Nevada Anomaly has been interpreted as a lithospheric drip due to its high velocities and the circular pattern of shear wave splits centered on the anomaly (West et al., 2009).

A pair of high velocities extend into the Basin and Range from the northeast near the Four Corners region, consistent with the location of the Colorado Plateau. This is a remarkably stable feature in a region that is defined by a large amount of extension (Zandt et al., 1995). There is a sharp transition from low Basin and Range velocities to high Colorado Plateau velocities (Sine et al., 2008). Additionally, there exists an abrupt transition on the surface from deformed metamorphic mountain ranges and broad alluvial valleys, characteristic of the Basin and Range, to relatively undeformed sedimentary sequences of the Colorado Plateau. Together, these suggest a sharp contrast in lithospheric strength. The Colorado Plateau

is undergoing uplift to this day, either the result of active mantle upwelling beneath it (Karlstrom et al., 2012; Liu et al., 2010; Moucha et al., 2009), heating of the strong lithosphere (Roy et al., 2009), or due to a lithospheric delamination of the plateau (Levander et al., 2011).

The final significant feature in our model is the low velocity body beneath Yellowstone. Debate continues to this day (Sigloch, 2018) whether Yellowstone magmatism represents a mantle plume (e.g., Camp and Ross, 2004; Darold and Humphreys, 2013; Obrebski et al., 2010), or upwelling from either a lithospheric instability (Hales et al., 2005) or the subducting Farallon/Juan de Fuca slab (James et al., 2011; Liu and Stegman, 2012; Zhou et al., 2018a). Our model provides no significant, new insight into this debate, but Yellowstone magmatism is invariably tied to the fragmented Juan de Fuca plate in the mantle. Resolving which is the cause, and which is the effect remains a fundamental question regarding the last ∼20 Ma of evolution of the western United States, and is of considerable geodynamic importance.

Finally, the Laramide orogeny, forming the Rocky Mountains at ∼70 Ma (Burchfiel et al., 1992), appears to have been caused by a period of Farallon flat slab subduction induced by the Hess and Shatsky oceanic plateaus (Liu and Gurnis, 2010). Much of the lithosphere created in this orogeny has been extended and thinned in the Basin and Range province. One possibility for the transition to Basin and Range is the cessation of subduction along the western margin of North America (Humphreys and Coblentz, 2007). In this model, the change in the plate boundary from subduction of the Farallon plate to translation of the Pacific plate would reduce compressive stresses, the thickened North American lithosphere would collapse, and as a result of that collapse and thinning, the mantle would respond by passively upwelling beneath the lithosphere, producing widespread thermal anomalies and significant magmatism. In contrast, some authors argue that mid-ocean ridge systems in general represent regions of active mantle upwelling (e.g., Rowley et al., 2016), and that Laramide collapse was caused by the westward migration of North America over the East Pacific Rise (Moucha et al., 2009). In this model, the relatively stable region of upwelling causes lithospheric uplift and extension when North America passes over it. These two models make fundamentally different predictions about how North America will evolve through geologic time, and ultimately paint very different pictures about the role of mantle convection in plate tectonics: one in which plate motions are primarily driven by the convective downwellings at subduction zones, and the other in which active downwellings and upwellings play a role in plate motions.

2.5 Conclusion

The tectonics of western North America show a remarkable diversity over a relatively small geographic area. Using seismic data from onshore and offshore seismic arrays, we have generated two tomographic models of seismic velocity beneath the western United States, extending offshore to image the mantle beneath the Juan de Fuca plate in its entirety.

Through these models, we have been able to better constrain the dynamics of both the mantle beneath the Juan de Fuca plate, and the interaction between the Juan de Fuca plate and North America.

Offshore, we observe evidence for active upwelling beneath the Juan de Fuca ridge. There is a hint that a plume supplying the heat for the Cobb Hotspot plays a role in the upwelling beneath the ridge here, so we cannot infer global dynamics through this observation. A low-velocity feature is consistent with a lithosphere that is defined at its base by melt or hydrated minerals. Because of the young age of the Juan de Fuca plate, it is difficult to extend this result with certainty to the all the world's ocean basins, but observations of a sharp lithosphere-asthenosphere boundary in other locations are consistent also with this model.

We image a hole in the central section of the subducting Juan de Fuca plate that is challenging to dismiss as an artifact. This hole appears to be correlated to a weak zone on the Juan de Fuca plate and with volcanism in North America, and implies that the fragmentation of the plate in the subsurface is (a) driven by a structure that is inherited from its formation at the ridge, and (b) able to transmit stresses updip, all the way to sections of the plate that have yet to subduct.

The subduction zone displays segmentation along strike, and the boundaries defined by this segmentation are remarkably consistent across a wide range of unrelated geophysical datasets, including both the deep structure of the slab and the shallower mantle wedge imaged in our tomographic models. While no conceivable mechanism could control the segmentation in every dataset, it appears likely that the primary control is the structure of the overriding North American plate, both in the form of the oceanic terranes that define the forearc, and in the form of Basin and Range extension that occurs in the southern part of the backarc.

Finally, the demise of the Juan de Fuca plate, and the interaction between it and North America, is happening within a mantle that appears to be very active on a range of scales. How that activity affects plate motions, and vice versa, is of critical importance to understanding plate tectonics, and ultimately to understanding the evolution of the earth through geologic time.

Chapter 3

Tomography reveals buoyant asthenosphere accumulating beneath the Juan de Fuca plate

Coauthors: Richard M. Allen, Mark A. Richards

3.1 Introduction

The physical causes of the lithosphere-asthenosphere boundary (LAB), possibly representing a zone that mechanically decouples tectonic plates from the asthenospheric mantle beneath (Richards et al., 2001; Craig and McKenzie, 1986), remain poorly understood (Fischer et al., 2010). The LAB beneath continents appears deep and somewhat obfuscated by other discontinuities (Rychert and Shearer, 2009; Yuan et al., 2011), so discerning the LAB has been hindered by the complicated nature of deep continental structure. The oceans are tectonically simpler than continents, so both the observation and description of the LAB should be simpler there, but because oceans are poorly instrumented, serious difficulties remain in resolving the LAB beneath oceanic lithosphere (Kawakatsu, 2012). Of particular interest is this lithosphere-asthenosphere interaction at convergent margins. The geometry of an oceanic plate changes as it dips into the mantle at a subduction zone, and the response of the uppermost mantle remains debated (Song and Kawakatsu, 2012; Long and Silver, 2008, 2009). New constraints on processes beneath a dipping plate may provide insights into not only subduction zone dynamics, but also large-scale asthenospheric flow and its role in the evolution of tectonic plates.

3.2 Method and Tomographic Model

First arrivals of P-waves from distant earthquakes recorded on large seismic arrays can be used to illuminate large parts of the mantle. One such array, the Cascadia Initiative (Toomey

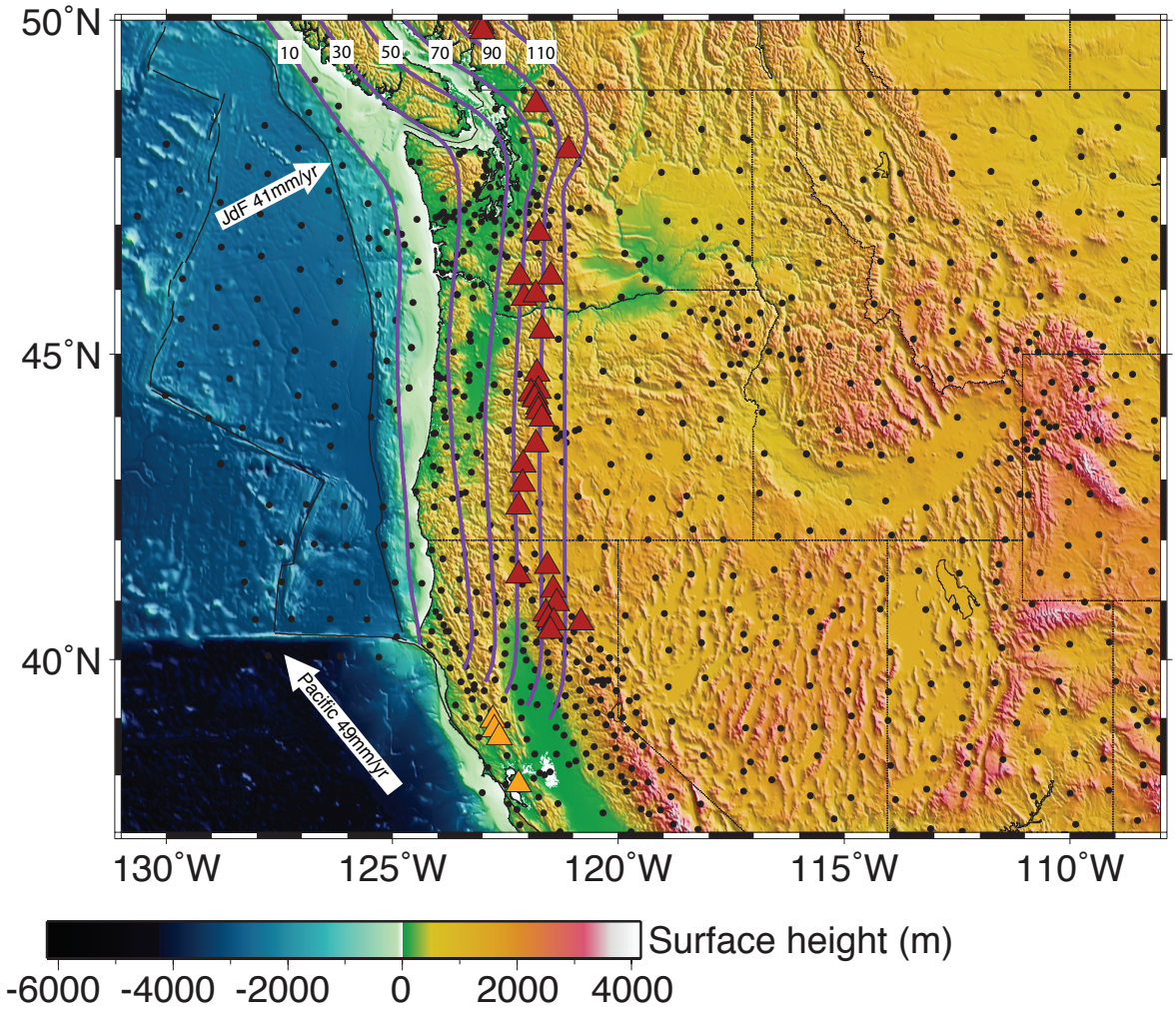

Figure 3.1: Stations used in our inversion (black dots) overlain on topography. Cascade volcanoes are red triangles, and northward age-progressive California Coast Ranges volcanism is shown by orange triangles. White arrows indicate plate motions relative to North America. The estimated depth of the top of the subducting slab is shown by the purple contours labeled in km (McCrory et al., 2012)

et al., 2014), was a four-year (2011 – 2015) amphibious seismic deployment that covered the Juan de Fuca plate and the Cascadia Subduction Zone (Fig. 3.1). Using 61,559 P-wave arrivals observed on this array, the TransportableArray, and other regional seismic networks, we generated a P-wave velocity model of the region through finite-frequency tomographic inversion following the method of Obrebski et al. (2010). Our application of finite-frequency sensitivity kernels means that our inversion takes into account the frequency-dependent

volume that is sampled by a P-wave traveling from the source to the seismometer, and obviates the need to smooth the final model. The noise characteristics of the ocean bottom seismometers (OBS) require that we use long-period ($9.1 - 12.5$ seconds) arrivals.

Our model (Casc16-P) shows an expected north-striking, east-dipping, high-velocity (+3% P-wave velocity change, dV_P/V_P) Juan de Fuca slab, seen at 150 km depth as a continuous north–south structure at about 122°W between 40°N and the northern edge of our model at 50°N (Fig. 3.2A). Vertical cross-sections at 47°N (Fig. 3.2B) and 41°N (Fig. 3.2C) show the slab is continuous down to the transition zone at 410 km, or deeper, consistent with previous land-based studies in the region (Obrebski et al., 2010; Schmandt and Humphreys, 2010; Tian and Zhao, 2012; Porritt et al., 2014). A previously unidentified strong low-velocity anomaly (-2 to -3% dV_P/V_P) is seen at 150 km depth with similar strike as the Juan de Fuca slab, just to the west. Vertical cross sections through the models and synthetic tests (Figs. 3.5, 3.6) indicate that this feature is restricted to the top 300 km of the model directly beneath the Juan de Fuca slab, meaning that it does not follow the slab all the way down to the transition zone. Further tests with various station correction terms (Fig. 3.4) indicate that this feature is not shallow structure being incorrectly mapped to depth. This truncated feature appears to take the shape of a horizontal cylinder, slightly elongated vertically in cross-section beneath the high-velocity slab. The addition of data from the Cascadia Initiative has provided the offshore resolution needed to confidently identify the full extent of this feature, though evidence exists for the feature in previous land-based tomographic models of the region (Obrebski et al., 2010; Schmandt and Humphreys, 2010; Tian and Zhao, 2012; Porritt et al., 2014).

3.3 Interpretation

We propose this low dV_P feature is related to previously reported observations of a layer of partial melt beneath the oceanic lithosphere. A range of techniques, including receiver functions from borehole OBS on the Pacific and Philippine Sea plates (Kawakatsu et al., 2009), precursors to teleseismic SS arrivals spanning the Pacific ocean (Schmerr, 2012), magnetotelluric inversion on the Nazca plate (Naif et al., 2013), and explosion-generated reflected P-waves offshore of New Zealand (Stern et al., 2015), resolve a narrow (10 – 25 km) region immediately below oceanic lithosphere characterized by low seismic wave velocities (-6 to -10% dV_S/V_S and dV_P/V_P) and high conductivity (4 to 6 Ω m). The interpretation for each of these studies is slightly different, but they all report that partial melt fractions of $\sim$1 to 4% in the uppermost asthenosphere are consistent with their findings, with variations arising due to different geometries of melt layers, composition of the melt, and the crystal structure of the materials in the layer. The slow seismic feature we observe in Casc16-P similarly coincides with a region of high conductivity. This thin layer is not resolvable in tomographic studies that use relative travel times from teleseismic events (Obrebski et al., 2010; Schmandt and Humphreys, 2010; Tian and Zhao, 2012), because such variations affect

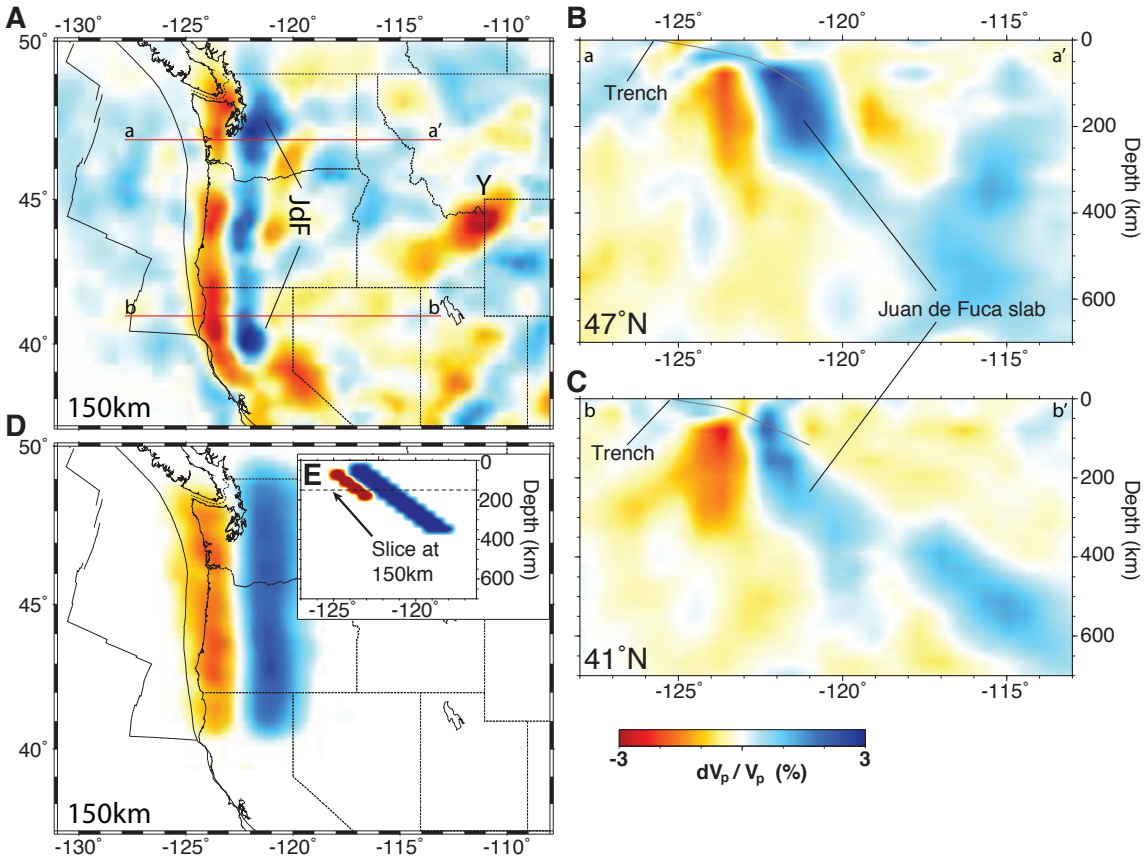

Figure 3.2: Slices through Casc16-P. (A) Slice at 150 km depth. The slow Yellowstone (Y) and the fast Juan de Fuca (JdF) slab anomalies are indicated. A strong low-velocity anomaly is seen west of the Juan de Fuca slab. Vertical slices through Casc16-P at 47°N (B) and 41°N (C) show the slab extending through the transition zone, while the low-velocity anomaly is confined to shallower depths (< 300 km). The top of the slab (McCrory et al., 2012) is shown with a grey line that begins at the trench. There is no vertical exaggeration in the vertical slices. (D) A slice at 150 km depth shows the recovery of a synthetic test with a 120-km thick +4% slab anomaly underlain by a 40-km thick −10% layer anomaly; the input synthetic velocity model is shown in (E). The recovery of synthetic features (D) is similar to that observed (A).

each ray path in the same way (Bastow, 2012). At a subduction zone, however, this layer might become observable where it changes geometry with the slab as it descends, and thus becomes detectable via teleseismic body wave tomography.

Predicting *a priori* how this layer might behave beneath a subduction zone requires

knowledge of its physical properties. Because we cannot resolve the layer to the west of the subduction zone, Casc16-P does not provide a direct observation of the source of the material in this layer. Previous reports (Kawakatsu et al., 2009; Schmerr, 2012; Naif et al., 2013; Stern et al., 2015) attribute the layer to volatiles and/or hydrated mantle increasing partial melt fraction in the uppermost asthenosphere, decreasing density and viscosity, separating into lenses (Hirschmann, 2010) or channels (Kawakatsu et al., 2009; Zhu et al., 2011), and ponding beneath the rigid, impermeable lithospheric lid (Hirth and Kohlstedt, 1996). Our observations, as well as the land-based observation of a high-conductivity region that roughly coincides with our low velocities (Evans et al., 2014), could be explained by the accumulation of material from this horizontal layer due to its own buoyancy and low viscosity.

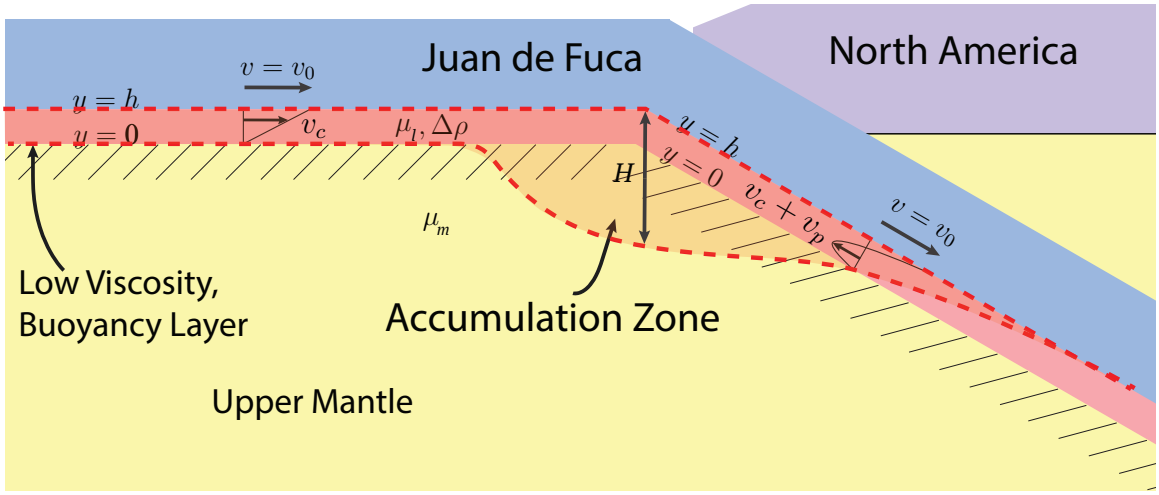

Figure 3.3: Geodynamical Model Setup. The low-velocity layer in red (not to scale) lies between the Juan de Fuca plate in blue and the asthenosphere in yellow. Comparing the Couette and Poiseuille velocity terms (v_c and v_p), yields an estimate for the viscosity of this layer, μ_l. In reality, this structure may take the shape outlined by the red dashed lines and tinted orange—thicker beneath the trench, and thinning out with depth. The extent of this feature depends on the density difference, $\Delta\rho$, and the upper mantle viscosity, μ_m. The features in this model are not to scale.

3.4 Geodynamic Scaling Relationships

Here we use two straightforward fluid-mechanical scaling calculations to demonstrate the plausibility of the accumulation hypothesis: First, for a thin, buoyant, low viscosity layer to accumulate beneath the downgoing slab the ratio of the upward mass flux due to the layer buoyancy (Poiseuille flow) must exceed the downward flux due to drag from the downgoing

slab (Couette flow) (e.g., Turcotte and Schubert, 2002). Referring to the notation in Figure 3.3, this means that

$$\frac{\Delta\rho \sin(\theta) h^2}{6 v_0 \mu_l} \leq 1 \tag{3.1}$$

The second condition (e.g., Feighner and Richards, 1995) is that the horizontal gravitational spreading velocity of the accumulated low-velocity volume due to its own buoyancy cannot exceed the horizontal advection velocity due to plate motion, otherwise the accumulating low-viscosity body would spread out instead of accumulating to the observed thickness of $H \approx 50 - 100$ km, as inferred from our tomographic images. This means that

$$\frac{\Delta\rho g H^2}{v_0 \mu_m} \leq 1 \tag{3.2}$$

In obtaining equations 3.1 and 3.2 we assumed that the thin layer viscosity controlling return flow is much smaller than the underlying mantle viscosity governing gravitation spreading, i.e., $\mu_l \ll \mu_m$ (see section 3.8 for a more detailed explanation).

Assuming that $\Delta\rho \approx 5 - 20$ kg/m^3 ($1 - 4\%$ partial melt, with 500 kg/m^3 density contrast between melt and solid (Karato and Jung, 1998)), gravitational acceleration $g = 9.8$ m/s^2, dip angle $\theta = 40°$, plate velocity $v_0 = 40$ mm/yr, and layer thickness $h \approx 10 - 25$ km, condition 3.1 implies that the viscosity of the thin, weak layer falls in the range $\mu_l \approx 0.04 - 1.0 \times 10^{19}$ Pa-s, which is reasonable for partially molten uppermost mantle (Doglioni et al., 2011). Similarly, with a low-velocity feature thickness of $H \approx 50 - 100$ km, condition 3.2 yields an underlying mantle viscosity that falls in the range $\mu_m \geq 0.1 - 1.5 \times 10^{21}$ Pa-s, which is also reasonable (Doglioni et al., 2011; Paulson and Richards, 2009). Furthermore, a convergence rate of ∼40 mm/year suggests that about $100 - 400$ km of continuous subducted lithosphere would be required to form the observed feature from accumulation of a thin buoyant, sublithospheric layer, a condition consistent with the ∼400 km of continuous slab observed in our tomographic model.

A more sophisticated treatment of this interesting mantle flow problem is beyond the scope of this paper, requiring a full numerical solution as well as consideration of other complicating factors, such as trench-parallel extrusion of buoyant material toward the slab edges (Höink and Lenardic, 2010), relaxing the assumption that $\mu_l \ll \mu_m$, etc. However, satisfaction of the two necessary conditions above for accumulation and maintenance of the low-velocity feature demonstrates that our hypothesis is plausible. More precise knowledge of the geometry of the feature will help constrain critical physical parameters, but Casc16-P provides a 'maximum extent' of the feature. The grid we used in the inversion and the smoothing due to finite-frequency sensitivity kernels make a strong, thin velocity anomaly appear thicker and weaker (Fig. 3.2D,E). Further studies with higher resolution will enable more detailed geodynamical models.

3.5 Implications and Conclusions

The material we observe could be important for "petit spot" volcanism in the forearc bulge east of the Japan trench. Samples from these young (∼5 million year old, Ma), alkalic volcanoes in the 120 − 150 Ma Pacific plate (notably much older than any part of the Juan de Fuca plate) are highly vesicular, suggesting the presence of CO_2, and isotopically similar to basalts found at mid-ocean ridges. One explanation for the presence of these volcanos in such an unusual region of the ocean floor is that the volcanism is due to partial melt rising through flexure-induced fractures in the lithosphere, and that it lends credence to the idea that the asthenosphere is a zone of partial melt (Hirano et al., 2006). Other studies (Karato and Jung, 1998; Faul and Jackson, 2005) argue that the entire asthenosphere need not be a zone of partial melt. The proposed low-viscosity layer could provide a source for enigmatic volcanism without requiring any assumptions of partial melt throughout the asthenosphere. Additionally, the chemistry of such basalts may help contextualize the composition of the low-viscosity layer.

This potentially partially molten feature may also explain the anomalous heat flow and volcanism of the Coast Ranges of California (orange triangles in Fig. 3.1). Lachenbruch and Sass (1980) proposed that as the southern edge of the Juan de Fuca slab migrates northward with the Mendocino Triple Junction, the "window" that opens beneath the margin of North America is filled with asthenosphere which undergoes decompression melting, leading to high heat flow and volcanism. Seismic observations (Hole et al., 1998; Furlong and Schwartz, 2004) reveal a high-velocity layer at the base of the North American crust beneath the California Coast Ranges. The thickness of this inferred mafic structure requires more melt than standard asthenospheric upwelling models predict. Both the lack of high-grade metamorphism inferred from the same seismic studies as well as the heat flow observations of Lachenbruch and Sass (1980) indicate less heat than predicted from the same asthenospheric upwelling models (Hole et al., 1998). A mechanism to generate more melt at lower temperatures has been elusive, but the accumulated low-velocity, partially molten and/or high volatile content material that we have imaged may provide that mechanism; i.e., decompression of the accumulated, already partially molten feature as it emerges toward the south through the slab window would provide more melt at lower temperatures.

3.6 Resolution Tests

We input specific geometries motivated by our interpretation of the model to test its resolution. Fig. 3.4 shows that introducing only high-velocity anomalies does not induce a low-velocity artifact that might account for our observed low-velocity feature. Fig. 3.5 demonstrates that the observed limited westward extent of the low-velocity roll in Casc16-P is not an artifact of the inversion. Fig. 3.6 shows various configurations of low-velocity features beneath the subducting slab. Figs. 3.6A–B show that a weak low-velocity feature

beneath the slab that extends to the transition zone is not recovered well at greater depths, however the strength of the signal beneath the hinge of the subducting slab is weaker than the feature in Casc16-P. Figs. 3.6C–D show that a stronger low-velocity feature beneath the slab matches the strength of the signal of that seen in Casc16-P, but is also resolved down to 400 km, in contrast with Casc16-P. Figs. 3.6E–H show low-velocity features that extend only to 150 km and 200 km appear to extend to 250 km and 400 km respectively, and match Casc16-P reasonably well.

3.7 Model Parameters

Additional inversions were performed with different station correction damping terms; these models are shown in Fig. 3.7. We show three inversions: one for which the station corrections are highly damped, which results in almost all of the travel-time delay for each station to be attributed to the mantle (Fig. 3.7A–C), an intermediate damping that is our preferred model (Fig. 3.7–F), and one with negligible damping, which allows for the largest individual station corrections supported by the data. Further reduction of the damping results in negligible changes to the station corrections. These models demonstrate that the low-velocity feature we interpret is a robust feature of the model across the range of station correction terms, and cannot be attributed exclusively to shallow slow structure being incorrectly mapped to depth.

3.8 Scaling Relationships

Channel flow driven by plate motion and resisted by channel buoyancy The conditions under which the buoyancy of the low-density, low-viscosity channel material can effectively resist being advected downward into the mantle by the subducting slab can be understood as a simple competition between Couette-type flow driven by the slab and Poiseuille-type flow driven by the buoyancy of this material. In the coordinate system indicated in Fig. 3.3, the Couette flow velocity in the channel parallel to the slab motion is given by $v_c = v_0 \, \frac{y}{h}$ where the y coordinate is zero at the bottom of the channel and h at the top. The buoyancy-driven Poiseuille flow resisting this motion is given by $v_p = -\frac{\rho g \sin(\theta)}{2\mu_l} \, y \, (y-h)$ where the negative sign indicates motion opposing the plate-driven flow. The approximate condition for accumulation of the buoyant layer material beneath the subduction zone is that the integral of the Poiseuille flow velocity over the channel depth ($y = 0, h$) is larger than or comparable to the integrated Couette flow,

$$\frac{\Delta\rho g \sin(\theta) h^2}{6 v_0 \mu_l} \geq 1 \tag{3.3}$$

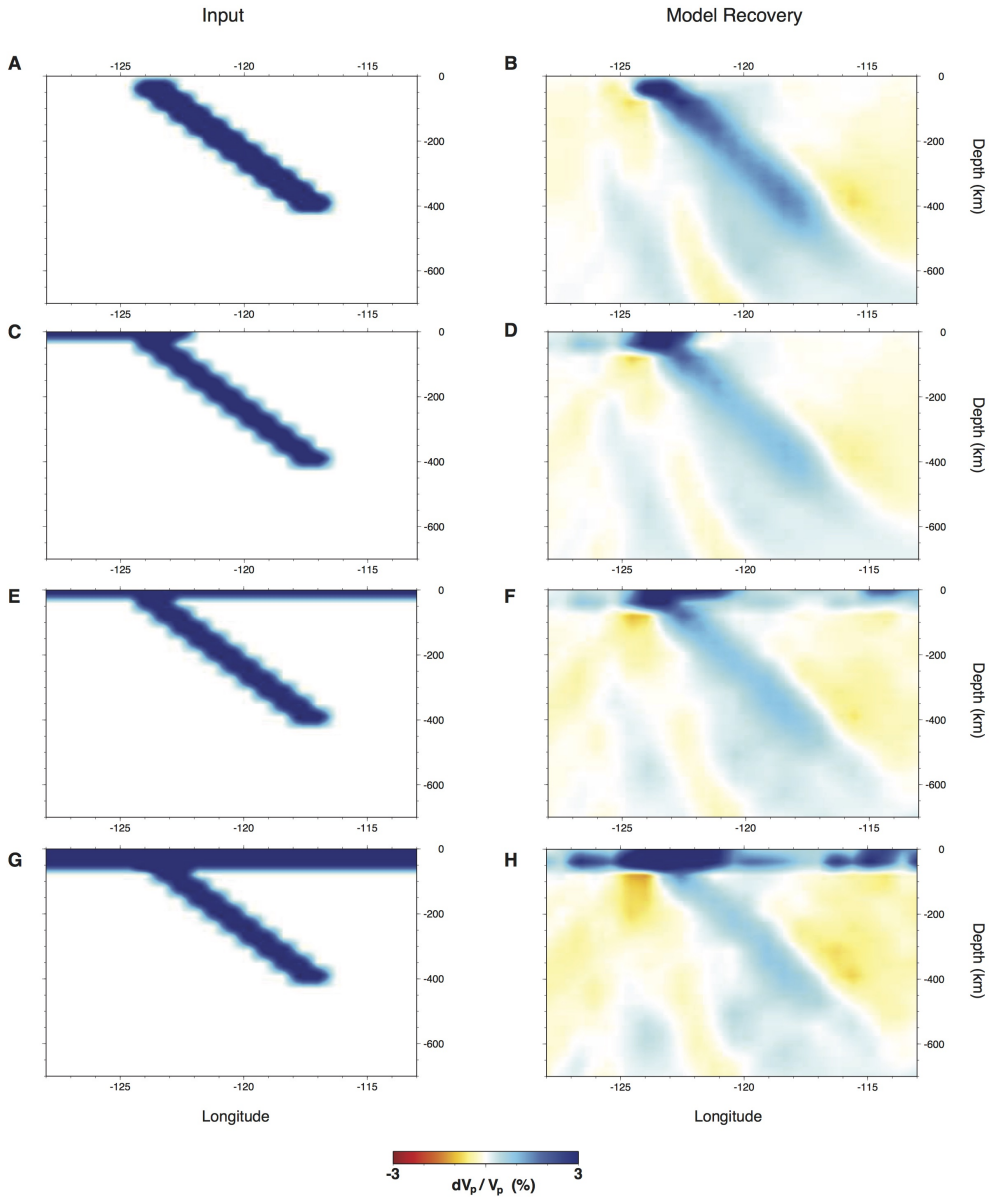

Figure 3.4: Synthetic models that include only high-velocity anomalies are unable to produce artifacts of the amplitude observed in Casc16-P, as in Fig. 3.2. (A–B) A 100 km-thick, +6% high-velocity feature was used as an input synthetic velocity model. (C–D) An 80km-thick, +4% slab is attached to a 20km-thick lithospheric lid that extends to the west. (E–F) An 80km-thick, +4% slab is attached to a 20km-thick lithospheric lid that extends to the east and the west. (G–H) An 80km-thick, +4% slab is attached to a 60km-thick lithospheric lid that extends to the east and the west. All configurations generate low-velocity artifacts that are low-amplitude, small scale, and not continuous.

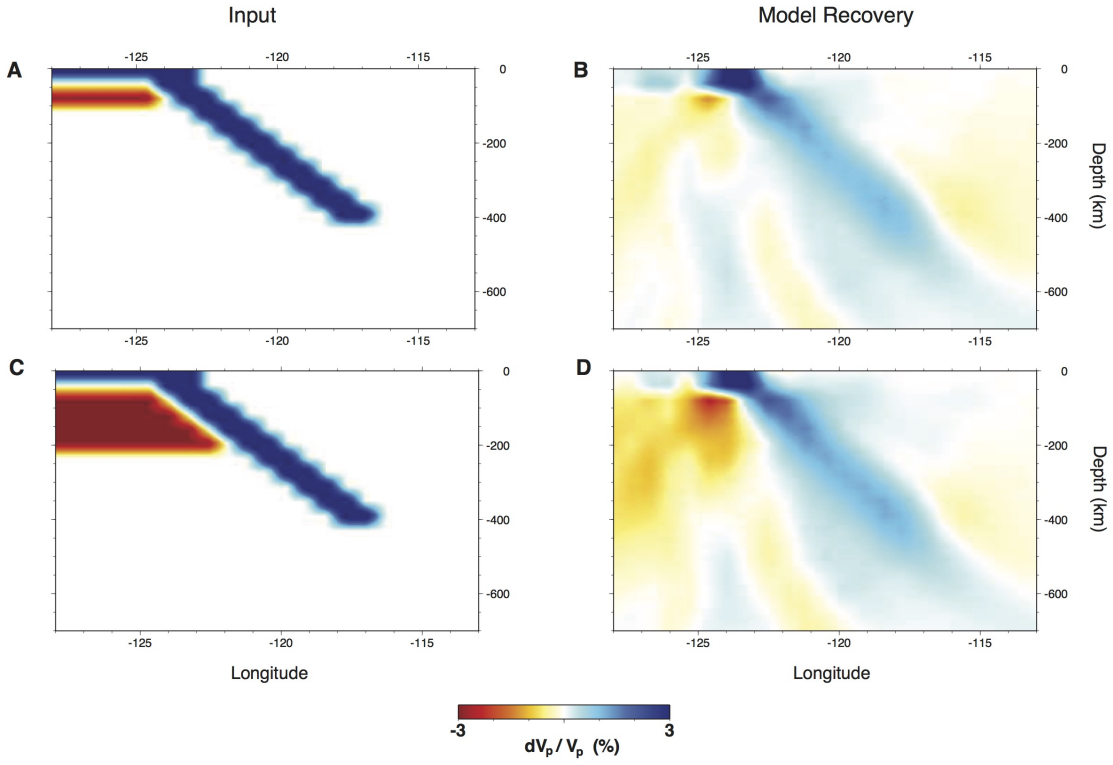

Figure 3.5: Synthetic models test our resolution of the western edge of the sub-slab low velocities. (A) An 80 km-thick, +4% slab is connected to a lithospheric lid that extends to the east and the west. A 40 km-thick, −4% horizontal feature lies under the lithospheric lid to the west. (B) Recovery shows that the strongest low-velocity signal comes from the eastward edge of the low-velocity feature, but it is low in amplitude, and low velocities are continuous well to the west, in contrast with Casc16-P. (C) A similar 80 km-thick, +4% slab is connected to a lithospheric lid that extends to the west. A 160 km-thick, −3% region lies under the lithospheric lid. (D) The strongest low-velocity recovery is in the slab hinge, but low velocities are pervasive under the lithospheric lid down to the transition zone, in contrast with Casc16-P.

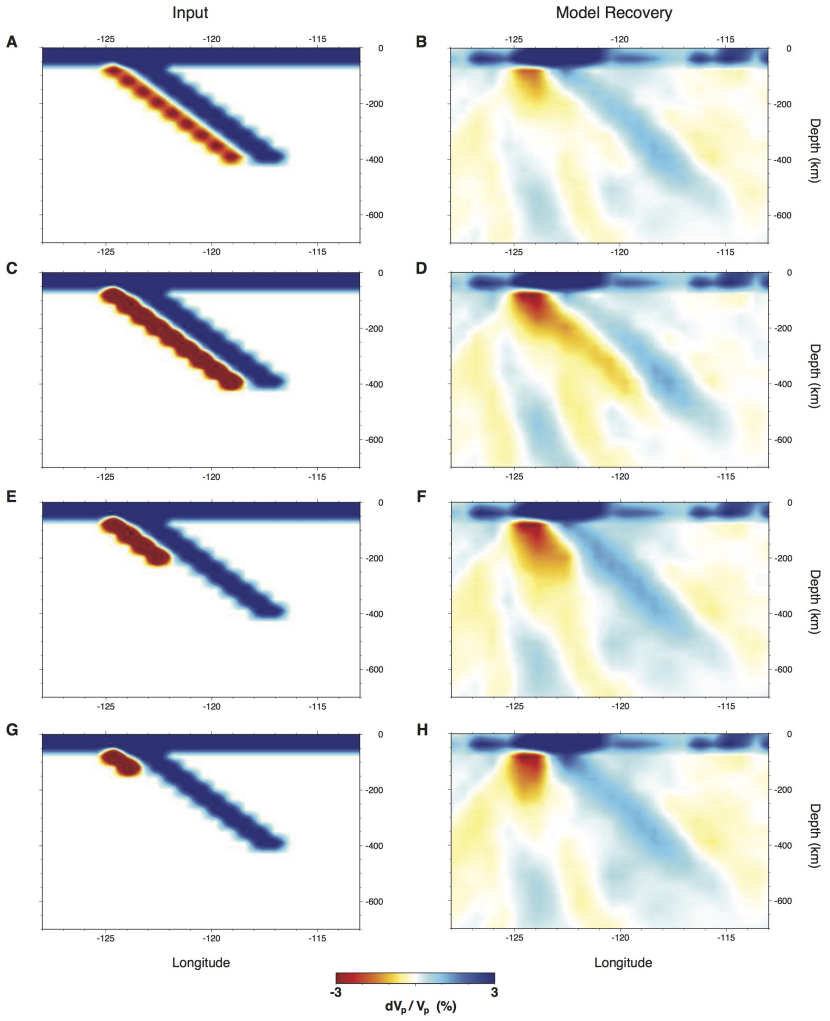

Figure 3.6: Synthetic models test optimal depths to which the low velocities can extend. All four models have an 80km-thick, +4% slab connected to a 60 km-thick, +4% lithospheric lid that extends to the west. All four input low-velocity features are 30 km thick. (A) The high-velocity slab is underlain by a −6% low-velocity feature that extends to 400 km depth. (B) Recovery of the feature in the hinge is weaker than observed in Casc16-P, and sensitivity drops off rapidly with depth. (C) The slab is underlain by a −10% low-velocity feature that extends to 400 km depth. (D) Signal in the hinge matches that observed in Casc16-P, but low velocities are recovered down to 400 km depth, in contrast to Casc16-P. (E) The slab is underlain by a −10% low-velocity feature that extends to 200 km depth. (F) Signal in the hinge is slightly stronger than that observed in Casc16-P, but the two are similar. The feature appears to extend down to 300km. (G) The slab is underlain by a −10% low-velocity feature that extends to 140 km depth. (H) Signal in the hinge closely matches Casc16-P, and appears to extend down to 250km.

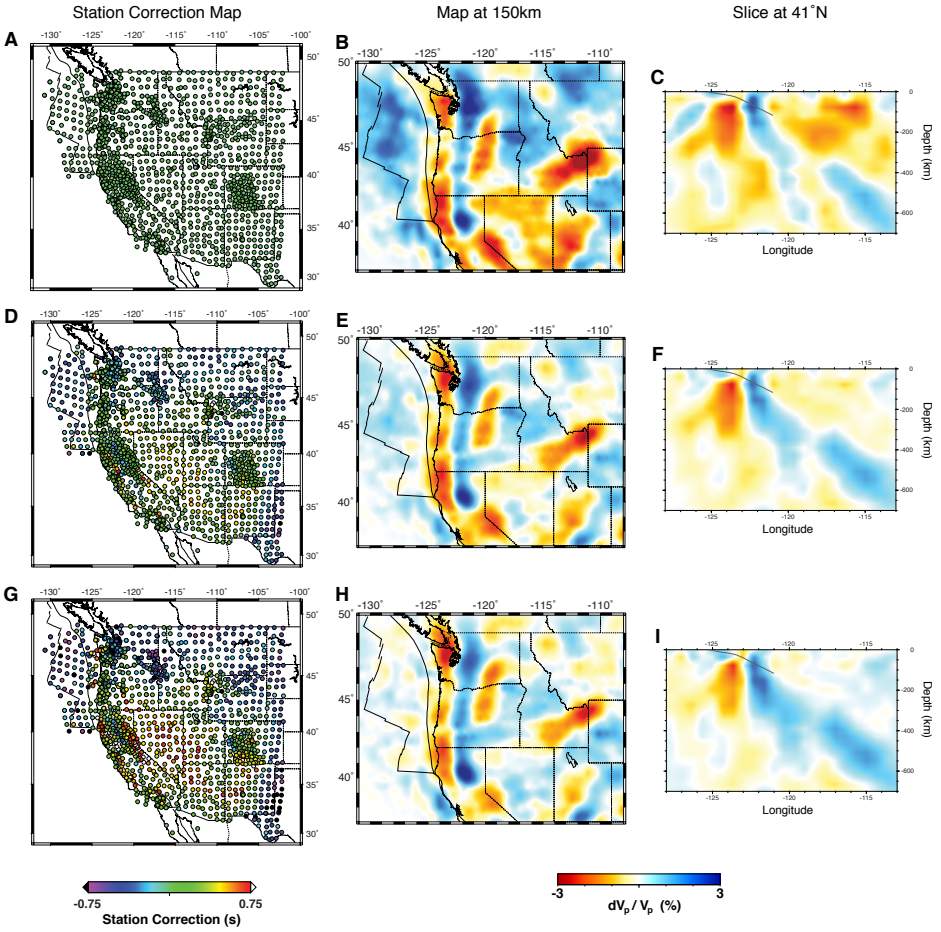

Figure 3.7: Three inversions with various station correction parameters. (A–C) Inversion result where the station corrections are highly damped, resulting in small station corrections and more of the signal being pushed into the (deeper) velocity model. (A) A map of station corrections determined in the inversion. (B) A horizontal slice at 150 km depth of the same inversion. (C) A vertical slice through the same model at 41°N. (D–F) As with (A–C), but with less damping of station corrections, thus allowing for larger station corrections. This is the model we have used for interpretation. (G–I) As with (A–C), but negligible damping; this allows for the largest individual station corrections that the data can support. Despite more of the travel-time delay being attributed to the geology directly beneath the station, i.e., accommodated in the station correction, the major geologic features observed in the velocity model remain strong elements in the model. Further reduction in the damping of the station correction terms results in negligible changes to the values of the corrections, meaning that the station correction terms have absorbed as much signal as they are able in the inversion shown in (G–I).

Gravity flow of accumulated channel material resisted by overlying plate-driven advection The above condition describes the conditions under which low-density, low-viscosity channel material may begin to accumulate beneath the subduction zone. However, this calculation does indicate how much material (what thickness H) can accumulate until its own buoyancy causes it to spread horizontally as fast as it can accumulate. The latter condition is obtained by setting the gravity flow velocity approximately equal to the overlying horizontal plate motion. Following the analysis of Feighner and Richards (1995) for a blob or "pancake" of thickness H of low-density, low-viscosity material spreading beneath a plate, and being resisted by a much higher-viscosity surrounding mantle, we can approximate the horizontal gravity force acting over an area Dh as $\Delta\rho g H^2 D$, where D is the surface area of the accumulated blob of channel material. (In our case D and H are, in fact, comparable, but this is of no consequence as D drops out of the calculation below.) The retarding viscous force is given by $\mu_m v_g D$, where v_g is the horizontal gravity flow velocity. Requiring that the gravity flow velocity not exceed the overlying plate velocity ($v_g \leq v_0$) as a condition for maintaining a roll of thickness H yields

$$\frac{\Delta\rho g H^2}{v_0 \mu_m} \leq 1 \tag{3.4}$$

We note that condition 3.3 above involves the relatively low channel viscosity μ_l, whereas condition 3.4 involves the relatively high underlying mantle viscosity μ_m. This is consistent with our conceptual model in which the sublithospheric channel thickness is smaller (perhaps much smaller) than the dimension of the accumulated material beneath the subduction zone, that is, $h < H$. In fact, these two conditions together reveal that the ratio of the mantle viscosity and the layer viscosity is proportional to the ratio of the square of the accumulation zone thickness and the layer thickness, or

$$\frac{H^2}{h^2} \sim \frac{\mu_m}{\mu_l} \tag{3.5}$$

Two plots that explore the relationships between the thicknesses and the relevant viscosities are shown in Fig. 3.8.

The full published version of this chapter was published in Science (Hawley et al., 2016) and can be found through doi: 10.1126/science.aad8104.

3.9 Acknowledgements

Support for this work was provided by the National Science Foundation to W.B.H under the Graduate Research Fellowship Program (DGE-1106400) and to W.B.H. and R.M.A under grant OCE-1139701. The seismic data used in this study are archived by the IRIS Data Management Center (`http://ds.iris.edu/ds/nodes/dmc/`) and the Northern California Earthquake Data Center (`http://www.ncedc.org;doi:10.7932/NCEDC`). Data are provided

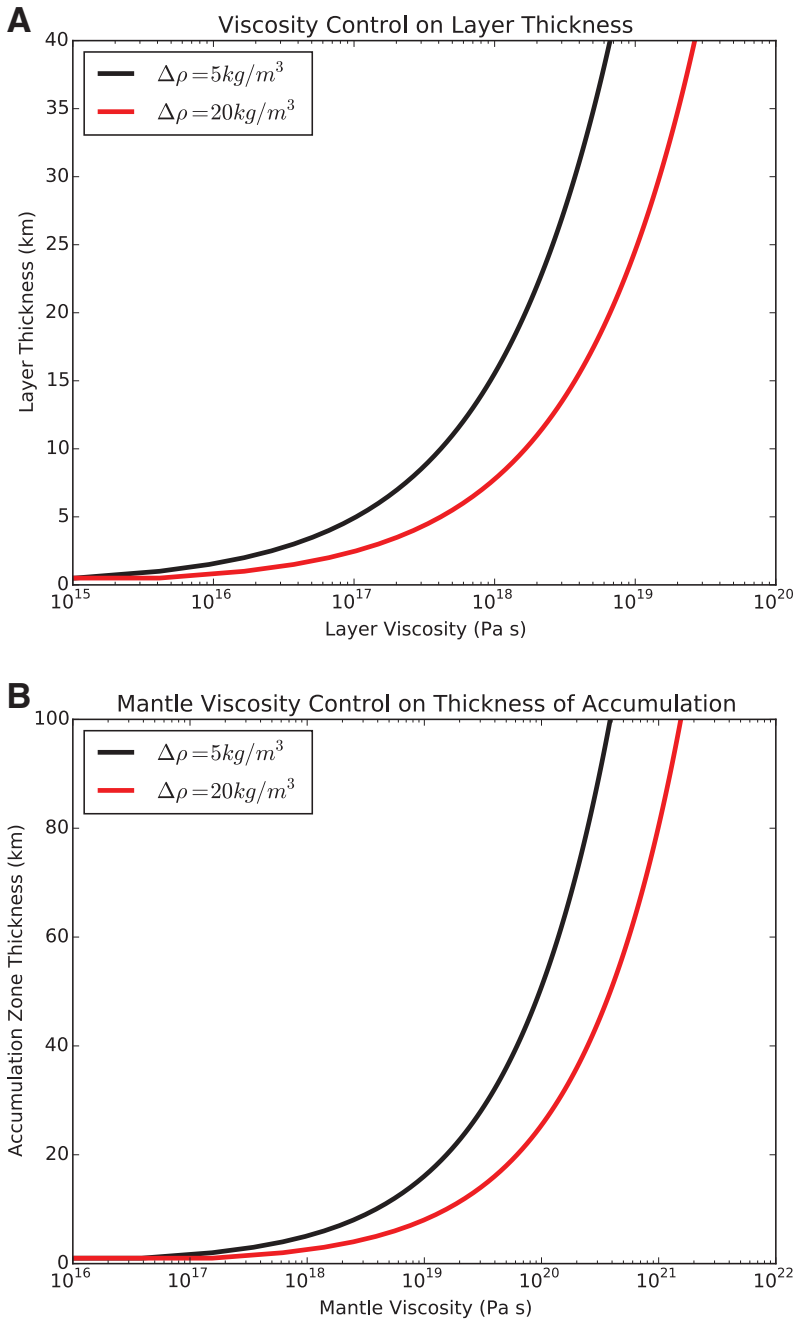

Figure 3.8: (A) Plot of the thickness of the horizontal layer h vs. its viscosity μ_l, from condition 3.3. For a layer thickness of $10 - 25$ km, the viscosity should fall in the range of $\sim 5 \times 10^{17} - 1 \times 10^{19}$ Pa-s. (B) Plot of the thickness of the accumulation zone H vs. the viscosity of the underlying mantle μ_m, from condition 3.4. For an accumulation zone thickness of $50 - 100$ km, the viscosity falls in the range of $\sim 1 \times 10^{20} - 1.1 \times 10^{21}$ Pa-s.

by many networks (see Supplementary Materials), but of particular note is the Cascadia Initiative ocean bottom data collected by OBSIP (`http://www.obsip.org/`) and funded by NSF (OCE-1112722). GMT (Wessel et al., 2013) was used to create the figures.

Chapter 4

The Fragmented Death of the Farallon Plate

Coauthor: Richard M. Allen

4.1 Introduction

In principle, the natural end of an oceanic plate's life is when the ridge that creates that plate reaches a subduction zone. Exactly how this occurs in practice, and what geophysical phenomena might accompany it, remains poorly understood. The Cascadia Subduction Zone, where the young Juan de Fuca (JdF) plate subducts beneath the western margin of North America, provides an ideal location to study this process. The JdF plate is the northern remnant of the Farallon plate, and represents the final stages of tens of millions of years of continuous subduction beneath the western margin of North America (Atwater, 1970). Furthermore, unsubducted fragments of the Farallon plate remain off the coast of western North America (Atwater, 1970; Wang et al., 2013), having been incorporated into the Pacific plate. These fragments provide a different snapshot in time of the same system, and evidence for how the final state of the Pacific–North America–JdF system might look. In this study, we present an S-wave velocity model using seismic data from arrays both onshore and offshore in this region to illuminate the link between subduction zone architecture, subduction dynamics, deformation, and volcanism, both in the subducting and the overriding plates, to shed light on the mechanisms that accompany the death of an oceanic plate.

Two key features that we will address are the internal deformation of the Gorda section of the JdF plate and the High Lava Plains (HLP) volcanic province (Fig. 4.1). The Gorda region, which is the southernmost section of the JdF plate, is undergoing intense deformation, primarily in the form of strike-slip faults that trend NE-SW near the ridge, transitioning to NW-SE farther from the ridge (Wilson, 1989, 2002). This deformation is thought to be because the Mendocino Transform, which bounds the Gorda region to the south, has not

reoriented as the Gorda and JdF ridges have rotated clockwise since 10 Ma. The Pacific plate just south of the transform was created at approximately 30 Ma (Atwater, 1970), and is thus colder and stronger than the much younger Gorda region, whose oldest unsubducted fabric was created at only 6 Ma (Wilson, 2002). Furthermore, the rotation of the ridge system has generated propagator wakes (Hey, 1977; Wilson, 1990), which are formed by overlapping segments of the ridge that migrate along the ridge axis. Propagator wakes extend down into the lithospheric mantle, and are locally more highly fractured—and likely weaker—than the rest of the plate (Han et al., 2016; Horning et al., 2016; Nedimović et al., 2009). These features can be seen as offsets in the magnetic anomalies. Propagator wakes have been linked to increased intermediate-depth seismicity due to dehydration (Nedimović et al., 2009)

The HLP is a volcanic province that extends from southeastern to central Oregon. Bimodal volcanism has occurred in the HLP since the mid-Miocene, marked in particular with rhyolitic features that show a distinct age progression, starting in southeastern Oregon, and migrating toward W15°N, at a rate of 33 mm yr^{-1} from 10 to 5 Ma, and 13 mm yr^{-1} from 5 Ma to the present (Jordan, 2005). This age progression makes the HLP unique from the other significant volcanism that has occurred in the region in Tertiary time, and thus implies a different mechanism. Current volcanism lies approximately 40 km east of the central Cascade arc axis. The age-progressive rhyolitic volcanism, accompanied by widespread basaltic volcanism, resembles in many ways the Yellowstone Snake River Plain, generally considered to be the result of a mantle plume (Camp and Ross, 2004; Pierce and Morgan, 1992). Furthermore, the origin of the age progression for these two provinces appear to be very similar in time and space: the Columbia River Basalt eruptions, at ∼17 Ma. While the mantle plume model fits many observations of the Yellowstone volcanic track, it is not consistent with other observations in the HLP, including the direction of age progression (Ford et al., 2013; Jordan, 2005) and helium isotope analysis (Graham et al., 2009). The most complete explanations for the HLP involve the JdF slab, either by a lateral tear in the slab at depth (Liu and Stegman, 2012), by large-scale Farallon-induced mantle flow (Zhou et al., 2018b), or by asthenospheric flow induced and focused by rollback of the strong, coherent JdF slab in the upper mantle (Ford et al., 2013; Long et al., 2012).

We generate a tomographic model from teleseismic S-wave data that shows that the slab below ∼150 km depth is discontinuous along strike, consistent with other models of the region (Bodmer et al., 2018; Hawley et al., 2016; James et al., 2011; Obrebski et al., 2011, 2010; Roth et al., 2008; Schmandt and Humphreys, 2010). We argue that the discontinuous slab may be driving volcanism in the HLP, similar to results of geodynamic simulations of the region (Liu and Stegman, 2012; Zhou et al., 2018b). We further contend that the fragmentation of the JdF slab at depth is driving deformation on the surface, and that the final stages of the life of an oceanic plate are dominated by bottom-up disintegration, rather than a simple cessation of subduction when the ridge meets the trench.

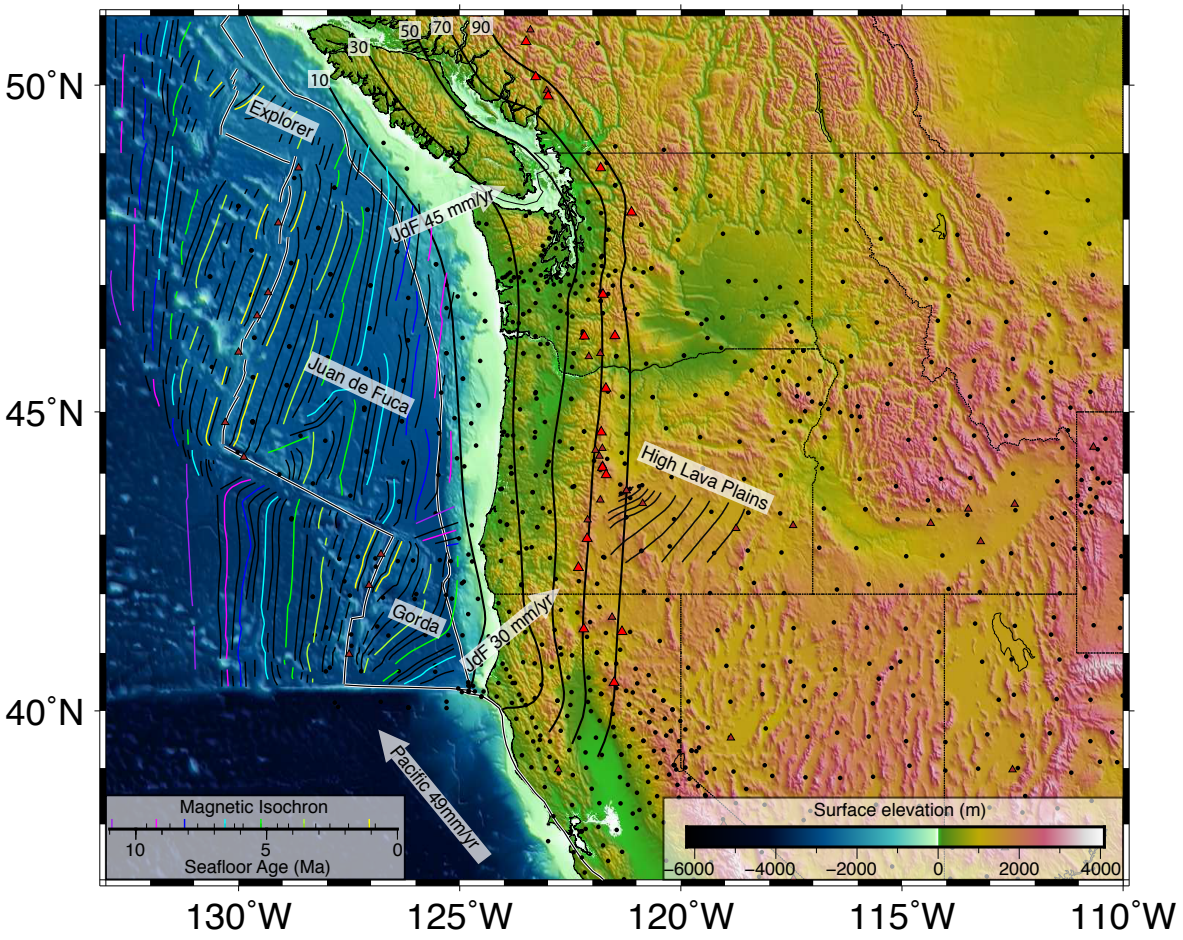

Figure 4.1: Regional tectonic map with seismic stations used in this study marked as dots. Double white lines indicate plate boundaries; plate motions of the Juan de Fuca and Pacific plates are shown as white arrows relative to North America. Magnetic isochrons offshore are from Wilson (2002). Thick contours east of the subduction zone indicate depth to the Juan de Fuca slab in km (McCrory et al., 2012). Thinner contours in southern Oregon represent 1 Ma isochrons of westward-propagating High Lava Plains volcanism (Jordan, 2005)

4.2 Data and Methods

We construct large-scale 3D images of the interior structure of the Earth using observations of seismic phases generated by distant earthquakes. Two seismic arrays, the Cascadia Initiative (Toomey et al., 2014) and EarthScope's TransportableArray, provide excellent coverage of the Cascadia Subduction Zone (Fig. 4.1). Using observations of 34,670 direct teleseismic S-wave arrivals from 217 events on these two arrays and other regional arrays, we have constructed an S-wave isotropic velocity model of the regional mantle through finite-frequency tomographic

inversion. The methodology is detailed in Obrebski et al. (2010). Our model domain is a spherical cap that extends from 27°N to 50°N, from 133°W to 101°W, and from the surface to 2500 km depth, with 65 nodes in each dimension. The model box is larger than the region in which we expect to have good resolution; delays that are not easily accounted for within the model domain will be absorbed at the edges of the model.

Horizontal components of ocean bottom seismometers (OBS) are plagued both with uncertainty in orientation and with higher noise, so we have picked the arrivals on the vertical component. The noise characteristics of the OBS also require that we filter in a narrower bandpass (20 – 40 seconds) than is commonly performed for onshore body-wave tomographic studies. We calculate the frequency-dependent sensitivity kernels (Dahlen et al., 2000). Our inversion minimizes the misfit in delay times by solving simultaneously for the isotropic velocity perturbation at each node, and a single correction term for each station and each event. The station corrections remove delays associated with the sediments and crust immediately beneath the station, minimizing contamination of the mantle velocity structure. Although station correction terms can absorb some of the real signal from the mantle, we choose to incorporate them because imposing crustal and lithospheric velocities introduces uncertainties that are difficult to quantify.

4.3 Tomographic Model

Our model, Casc19-S, is broadly consistent with Casc16-P, our previous P-wave model of the region (Hawley et al., 2016), as well as other tomographic models of the Pacific Northwest (Bodmer et al., 2018; James et al., 2011; Obrebski et al., 2010; Roth et al., 2008; Schmandt and Humphreys, 2010). The Juan de Fuca slab appears as a high seismic velocity feature that trends north and dips to the east (Fig. 4.2). At 80 km depth, this feature is continuous from about 40°N to the edge of our model at 50°N. By 150 km depth, the high velocity slab is not visible from roughly 44°N to 46°N. While the precise depth of this gap differs from model to model, it is a robust feature of virtually every tomographic model that has been produced in this region, with resolution beneath ∼150km depth, since the deployment of the TransportableArray here in 2006. Most of the models that do have resolution at this depth are teleseismic body-wave tomographic models, which generally have lateral resolution on the order of the station spacing; in this case ∼70 km. The vertical resolution of this type of model is not as good. Since the rays are traveling nearly vertically in the upper mantle, velocity anomalies tend to be smeared vertically, along the path of the incoming rays. Thus, again, while the depth of the hole is different in the models we reference here, the fact that there is a gap in the high velocities is robust.

The hole has been noted and interpreted by previous authors. Initially, it was proposed to be an artifact owing to significantly reduced velocities in the mantle wedge (Roth et al., 2008). Since then, there has generally been consensus that the hole is not an artifact, but

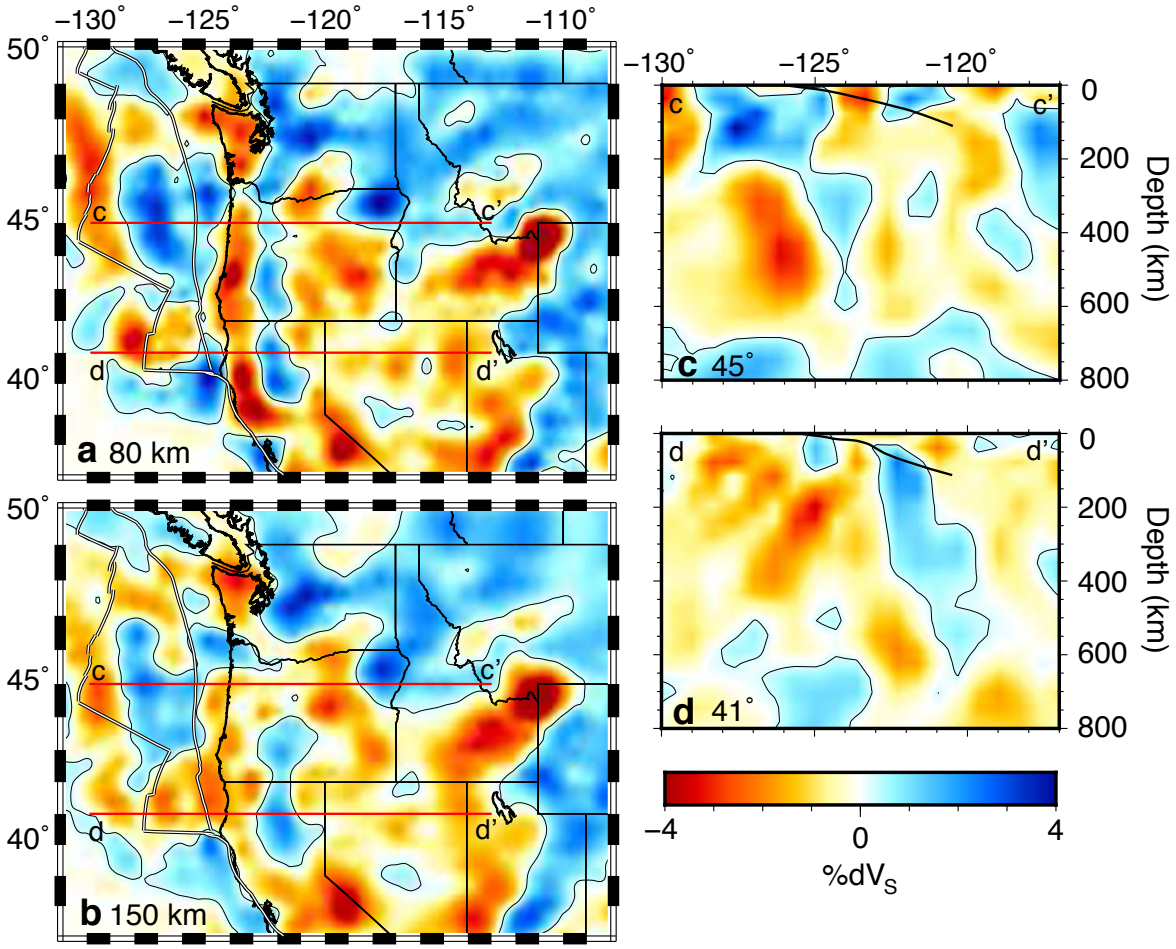

Figure 4.2: Slices through the tomography model, Casc19-S. Contours represent +0.25% dV_S. In the slice at 80 km depth (a), the slab is continuous north-south, with variations along strike in the strength of the recovered signal. By 150 km depth (b), the slab has a prominent gap between ∼44°N and 46°N. The depth extent of the slab is shown in two vertical slices, with a bold slab contour from (McCrory et al., 2012). The slice through the hole at 45°N (c) shows no high-velocity slab feature coincident with the McCrory et al. (2012) slab surface. The other shows that the Gorda slab at 41°N (d) extends at least to 400 km, and possibly 600km depth.

the creation of the hole has been attributed to a range of processes, including Yellowstone plume-induced slab destruction (Obrebski et al., 2010), along-strike variations in dynamic pressure from the mantle beneath the slab (Liu and Stegman, 2011), and simply evidence for complex subduction (James et al., 2011; Schmandt and Humphreys, 2010).

To reiterate that the apparent hole is not an artifact due to low velocities in the overlying mantle wedge, we point to a recent receiver function study (Cheng et al., 2017) that was able to resolve impedance structure between 100 and 200 km, where the hole appears in the tomographic models. A strong high-velocity feature situated immediately beneath a strong low-velocity feature would be difficult to resolve using teleseismic body wave tomography. Because, however, receiver functions are sensitive to sharp vertical velocity gradients, such a scenario would be detectable using that method. The fact that the size and depth extent of the hole is similar in both tomographic images and receiver function images makes an artifact an unlikely explanation for the feature.

4.4 Interpretation

The active expression of the HLP trend lies directly above the southern edge of the slab hole we image in Casc19-S. Slab holes have been inferred in other subduction zones (Obayashi et al., 2009; Portner et al., 2017), sometimes accompanied by anomalous volcanism (Berk Biryol et al., 2011; Rosenbaum et al., 2008). Dry basalts in the HLP have been explained by upwelling mantle in the back-arc due to rollback of the coherent JdF slab (Ford et al., 2013; Long et al., 2012; Till et al., 2013), but as the tomography models do not show a coherent slab, we explore the possibility that the volcanism is generated by asthenospheric flow through the hole and subsequent decompression melting.

4.4.1 Causes of the hole

The distinct age progression in the HLP suggests that if the volcanism is due to a tear in the slab, that tear is propagating updip. We can then estimate the speed and direction of this tear on the JdF slab by subtracting the JdF motion from the HLP motion, both of which are known with respect to North America. (vector sum in Fig. 4.3a). The JdF plate is subducting at $\sim$35 mm yr^{-1} toward N55°E relative to North America (Wilson, 1993), indicating that the tear velocity in the JdF plate has been, on average, approximately 50 mm yr^{-1} toward S75°W. This trend closely matches that of a prominent propagator wake in the northern Gorda region (Wilson, 2002) (Fig. 4.3a). Since propagator wakes are thought to be weaker than the rest of the plate (Canales et al., 2017; Horning et al., 2016; Nedimović et al., 2009), a tear along this pre-existing zone of weakness is a possible scenario. The precise depth of the hole is difficult to locate using teleseismic body-wave tomography, and appears at different depths in different models. Since, however, the resultant volcanism lies to the east of the arc, we can be reasonably confident that the tear is below 100 km depth. We stress that the depth of this deformation will preclude brittle failure—there are no earthquakes clearly associated with the tearing. The slab would instead thin along this weak region, eventually pulling apart.

At first glance, it seems unexpected that the volcanism would rest over the southern edge

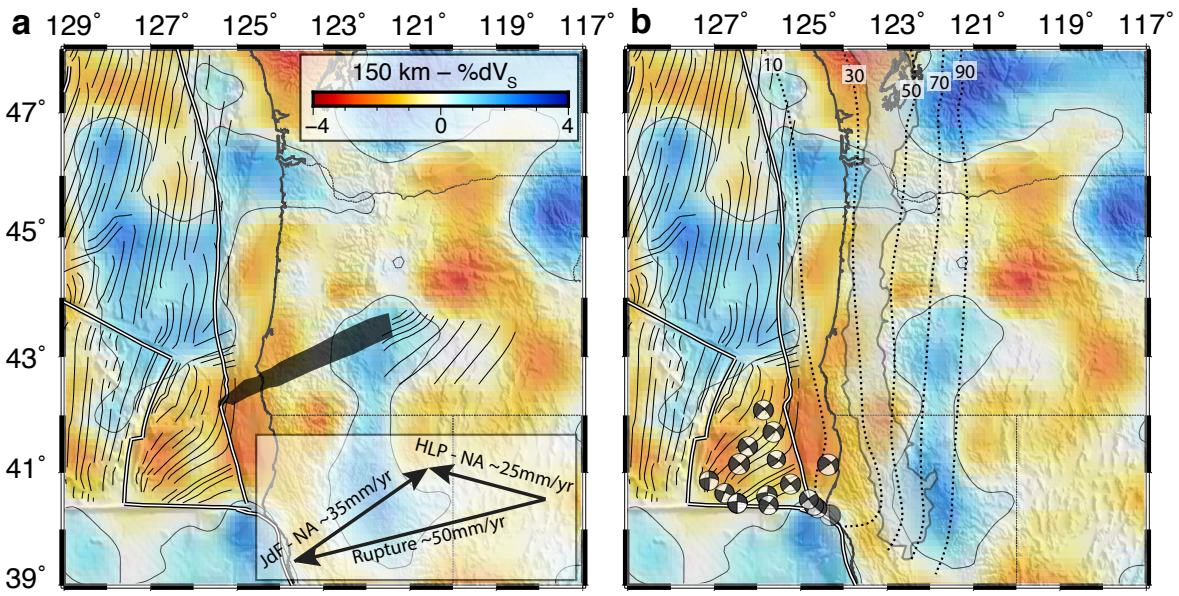

Figure 4.3: Detailed maps showing the causes and effects of the hole in the Juan de Fuca slab. A slice at 150 km depth through Casc19-S is shown with surface topography in both images. In (a), we focus on the relationship of the hole as seen in tomography with the propagator wake on the Juan de Fuca slab (grey shaded region; Wilson, 2002) and High Lava Plains 1 Ma isochrons (Jordan, 2005). The inset shows the proposed trace of the rupture on the Juan de Fuca slab, calculated by subtracting Juan de Fuca plate motion from the propagation of HLP volcanism, both with respect to North America. In (b), we focus on the resultant deformation of the Juan de Fuca plate. The southern extent of tremor activity (grey shaded region; Wech, 2010) and slab surface contours (dotted lines, labeled in km; McCrory et al., 2012) match the slab extent in Casc19-S, extending well south of the Mendocino Transform. Focal mechanisms are all offshore earthquakes from the GCMT catalogue south of 43°N, with $M_W > 6.3$.

of the hole, rather than in the middle. Carefully considering the geometry of the slab and propagator wake, and uncertainty in the precise shape of the hole as imaged with seismic tomography, helps to explain why the volcanism is over the southern end of the imaged hole. Shear wave splitting measurements (Long et al., 2009) and recent geodynamical modeling (Zhou et al., 2018a) indicate the horizontal component of mantle flow is largely east-west, and we thus expect little north-south flow between the tear and the volcanism on the surface. The NE-SW orientation of the propagator wake means that the deeper parts of the feature are situated farther to the north. The southern edge of the hole, then, would extend generally toward the east with depth, while the northern edge of the hole would trend generally to the northeast with depth. Thus the entirety of a hole resulting from this propagator wake will be to the north and east of the shallow tear, and any vertical smearing in the tomographic

images will result in low velocities being imaged to the north, but not to the south. We suggest that this is the reason the propagator wake aligns with the southern edge of the imaged hole.

A number of other propagator wakes are mapped in Wilson (2002). Only one of these propagator wakes is larger than the one we show in Fig. 4.3, and it has additionally been associated with increased seismicity (Nedimović et al., 2009). At depth, this propagator wake is not associated with a region of low velocities, and thus does not appear to be related to a similar tear in the slab. All of the other (smaller) propagator wakes are well north of our model domain by the time they reach ∼100km depth, and we will not speculate about whether similar tears may be happening elsewhere.

The existence of a propagator wake may not be a necessary condition at all. A tear has developed in the subducting slab in various geodynamic models of the region, both those that use as a starting condition a density field derived from seismic tomography (Zhou et al., 2018b), and those that use only surface constraints to define the boundary conditions (Liu and Stegman, 2011). In particular, these recent geodynamical studies have suggested that both the HLP and the Snake River Plain age-progressive volcanic tracks are a result of hot oceanic asthenosphere intruding into the mantle beneath North America (Zhou et al., 2018a,b), and do not explicitly model a hole in the downgoing slab. Thus, while the propagator wake is not necessary for anomalous HLP volcanism in the western United States, it is a specific and striking explanation that connects a structural feature inherited from creation at a mid-ocean ridge with an unusual but robust hole imaged in seismic tomography, and with anomalous volcanism on the overriding North American plate.

4.4.2 Effects on the subducting Juan de Fuca plate

We have argued, as have other authors, that slabs can tear in the mantle, and that this process can generate volcanism above the tear. We also show that the fragmentation of the slab in the mantle may be responsible for deformation within the JdF plate. The disintegration of the slab would allow a clockwise rotation of the southern fragment, which is connected to the Gorda section of the JdF plate. Clockwise rotation of this southern fragment is consistent with the observed southern edge of the subducting slab (Fig. 4.3b). This edge can be seen trending southeastward in a number of datasets, including the extent of non-volcanic tremor (Wech, 2010), a slab model constrained by microseismicity and active source seismic studies (McCrory et al., 2012), as well as our own tomographic model. This edge traces back to the Mendocino Transform between the JdF and Pacific plates, which trends east-west. The conjugate fracture zone on the Pacific plate is remarkably straight for more than 1000 km, also trending east-west. Absent deformation, it would be expected that the southern edge of the JdF slab would maintain the same strike. Wilson (2002) suggests that this is due to the stability of the Mendocino transform despite the rotation of the JdF ridge system. While this "snowplow" effect could generate the observed deformation, it also can be easily explained

by clockwise rotation of the southern slab fragment as it moves through the subduction zone and in to the mantle.

Furthermore, the process we propose is consistent with deformation within the Gorda region. This deformation manifests primarily as left-lateral strike-slip faulting on northeast-southwest trending faults. These are found in Gorda crust older than 2 Ma and south of the propagator wake (focal mechanisms in Fig. 4.3b). We suggest these are en-echelon faults as a result of clockwise rotation of the Gorda section relative to the Pacific and central Juan de Fuca plates. Again, while this deformation could be partially explained by the "snowplow" effect from the rotation of the JdF ridge relative to the Mendocino Transform, the process of slab fragmentation as we describe it here would have the same effect.

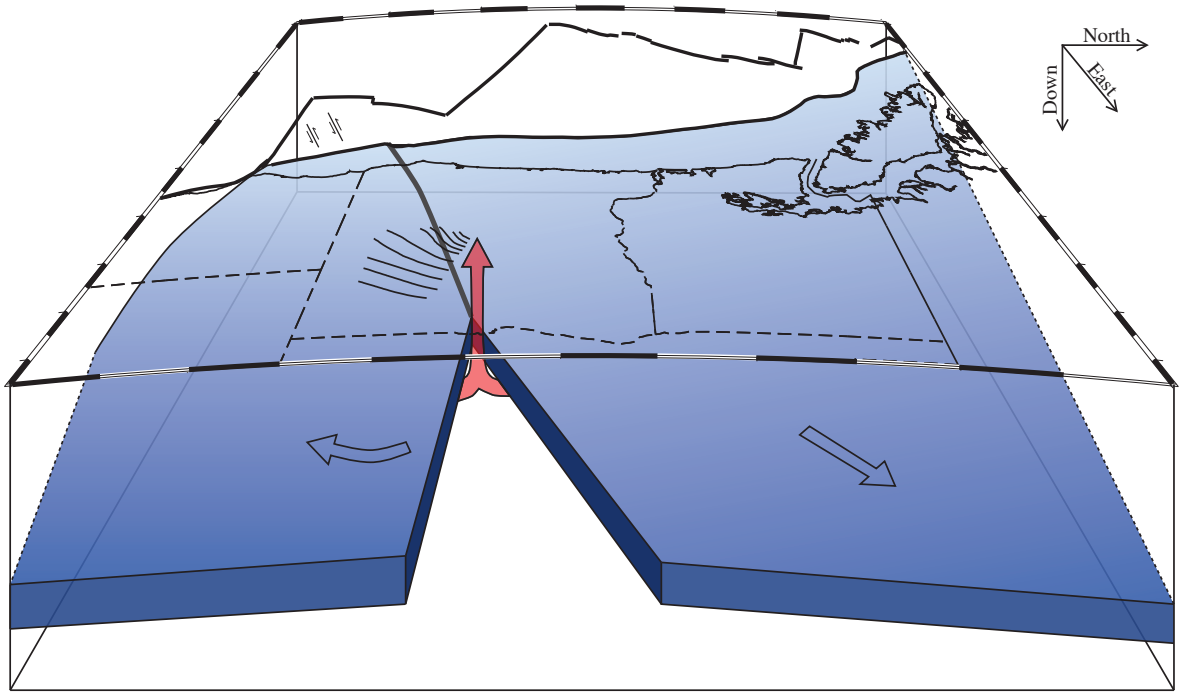

Figure 4.4: A schematic model that links the slab hole with other physiographic features. The view is from the east, and the JdF slab is shown in blue. The propagator wake (bold grey line underneath Oregon) causes a weakness in the slab along which a tear is propagating. The High Lava Plains (contours in Oregon) lie above the southern edge of the slab hole. The Gorda slab rotates clockwise, causing intraplate seismicity in the Gorda region.

4.4.3 Implications for subduction termination

Our connection of non-rigid behavior in the Gorda lithosphere with the fragmentation of the JdF slab at depth suggests that the death of an oceanic plate is a bottom-up process. Instead of subducting normally until the ridge meets the trench, a plate may begin to break apart on the surface as the ridge approaches the trench, driven by fragmentation of a weak slab in the mantle. This should not be surprising, given that, for example, there is significantly more plate surface-area that is slab attached to the Gorda section of the JdF plate than there is Gorda lithosphere on the surface. Burkett and Billen (2009) describe numerical models in which slab detachment occurs before ridge subduction; our conceptual model differs from this in two distinct ways: first, the deformation occurs on a pre-existing zone of weakness inherited from the formation of the plate; and second, the tear is not occurring laterally, parallel to the trench, but is originating from much deeper in the subducting slab.

If subduction ends before the ridge arrives at the trench, the surviving plate fragment will attach to one of the two plates that is bounding it—in the case of JdF, either the Pacific plate or the North American plate. Older fragments, such as the Magdalena, Guadalupe, and Monterey microplates, are seen in seafloor magnetic data, having been incorporated into the Pacific plate (Nicholson et al., 1994). It has been suggested that these plate fragments have stagnant slabs attached to them, extending into the mantle as deep as 200 km (Wang et al., 2013).

Alternatively, slabs can accrete onto the overriding plate, becoming the building blocks of a new continent. Old terranes, accreted onto North America, may still have visible slab fragments attached to them, such as the Llano and the Cheyenne slabs (Porritt et al., 2014). It is possible that the Gorda, followed by the rest of the JdF, will accrete onto North America in a similar fashion. Regardless of which plate the fragments of the JdF will accrete onto, our analysis suggests that the capture of these oceanic plate fragments is driven by processes in the mantle, which may, in turn, be driven by along-strike variations in the lithospheric structure inherited at the ridge.

4.5 Conclusions

A holistic analysis of seismic, geologic, petrologic, and marine geophysical data suggests that as the Juan de Fuca plate nears the end of its life, disintegration of the slab in the mantle drives deformation on the surface. A hole in the subducting JdF slab as seen in seismic tomography is coincident with age-progressive volcanic activity in the HLP, and closely matches a weak zone in the JdF plate, raising the possibility that these three phenomena are related. We suggest that a tear along the weak propagator wake encourages asthenospheric flow through the hole in the slab, generating volcanism in southeastern and central Oregon. The resulting fragmentation of the slab in the mantle affects the stress state on the surface,

leading to non-rigid motion in the Gorda section of the JdF plate. Furthermore, comparing with magnetic and seismic studies elsewhere, we suggest that this surficial fragmentation will persist as highly deformed geologic features, and the resulting fragments of the slab, unable to subduct, may accrete onto either the Pacific or the North American lithosphere. If our interpretation is correct, the Gorda section of the Juan de Fuca plate provides an excellent ongoing example of the processes that govern the demise of a long-lived oceanic plate.

4.6 Resolution Tests

We input two synthetic geometries to demonstrate confidence in our ability to image the slab hole. The first (Fig. 4.5) demonstrates the difficulty in generating an artifact with low-velocity anomalies that could be interpreted as a hole in the slab. The second (Fig. 4.6) indicates that determining the depth extent of the hole through our tomographic model may be difficult, but that we expect it is shallower than 175 km depth.

The full published version of this chapter was published in Geophysical Research Letters (Hawley and Allen, 2019) and can be found through doi: 10.1029/2019GL083437.

4.7 Acknowledgements, samples, and data

We thank M.A. Richards for discussions and comments on the manuscript. Generic Mapping Tools software (Wessel et al., 2013) was used to create the figures. Support for this work was provided by the NSF under Graduate Research Fellowship Program (grant DGE-1106400 to WBH). The data used in this study are archived by the Data Management Center of the Incorporated Research Institutions for Seismology (`http://ds.iris.edu/ds/nodes/dmc/`) and by the Northern California Earthquake Data Center (`www.ncedc.org;doi:10.7932/NCEDC`). The seismic velocity model may be downloaded from the Earth Model Collaboration repository of the Incorporated Research Institutions for Seismology (`http://ds.iris.edu/ds/products/emc/`).

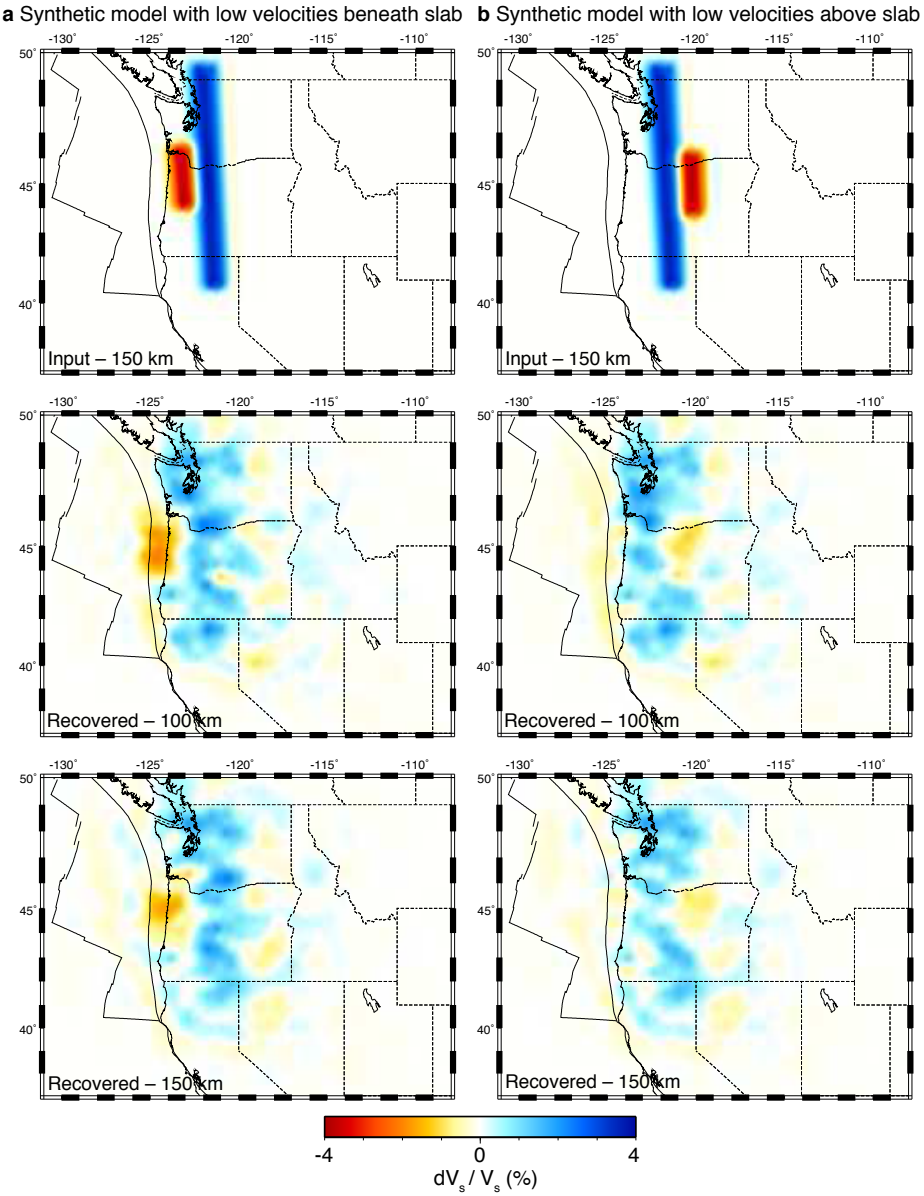

Figure 4.5: Synthetic tests with low-velocity anomalies. A synthetic model with a low velocity (-6% dV_S) anomaly below (a) and above (b) the slab ($+6\%$ dV_S) is used to create synthetic travel-times. We add noise to the data by adding a delay randomly selected from a Gaussian distribution with standard deviation 10% of the delay. In both cases, inverting these data is unable to generate an artifact that resembles a hole in the slab at 100 km or 150 km depth.

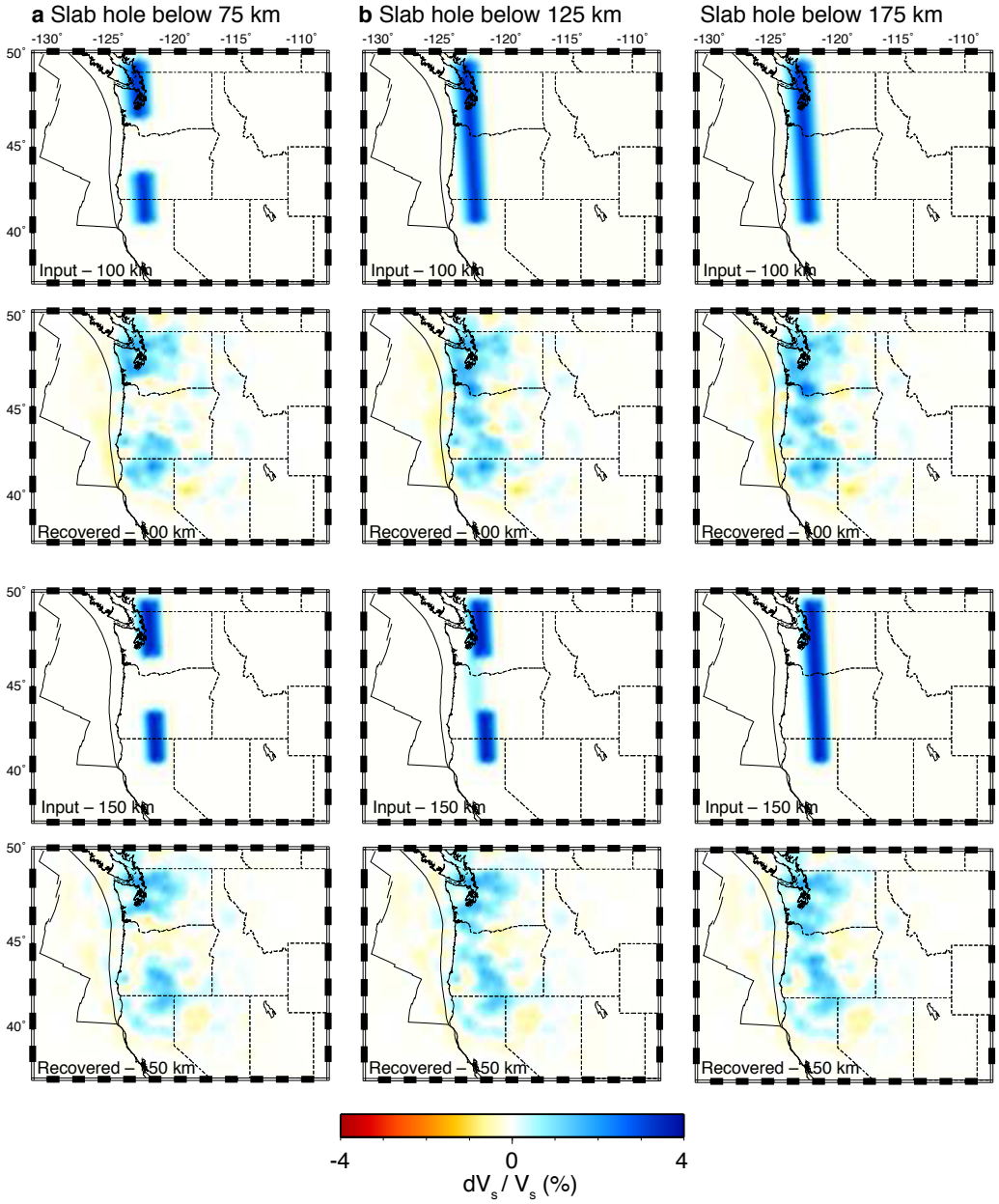

Figure 4.6: Synthetic tests varying the depth to the slab hole. Three synthetic models were created where a 300 km-long segment of the subducting slab (+6% dV_S) was removed below 75 km (a), 125 km (b), and 175 km (c). We show the input and recovered models at 100 km and 150 km depth, additionally adding 10% Gaussian noise to the synthetic travel-time delays. These tests show that the models cannot indicate the precise depth at which the hole appears, but it is likely shallower than 175 km.

Chapter 5

Conclusion

The Cascadia Initiative ocean bottom seismometer array has allowed new images of the mantle beneath an oceanic plate in striking detail. The two tomographic models presented in this dissertation, constructed using data derived from a combination of offshore and onshore instruments, have helped to sharpen our understanding of the Juan de Fuca plate, and its interaction with North America and the mantle beneath. Because of the uniqueness of the Cascadia Initiative, these models not only help to uncover the interactions between the Juan de Fuca plate, the North American plate, and the upper mantle. These models have also refined our understanding of plate tectonics, pushing forward in key areas where significant uncertainty remains: how are plates created, and how do they die? How does the convecting mantle, the only reservoir with adequate energy to drive plate motions, affect the lithosphere? In this dissertation, we have used these two models to explore the entire life cycle of an oceanic plate, from its birth at a ridge to its demise, either in the mantle or in accretion to surrounding plates.

At the Juan de Fuca ridge, we show in Chapter 2 that the evidence for active upwelling is robust. The western flank of the ridge is characterized by more seamounts, lower seismic velocities in the upper mantle (Bell et al., 2016), and a stronger impedance contrast at the base of the partial melt zone (Rychert et al., 2018). Modeling studies suggest that asymmetry is likely due to a thermal or compositional gradient, or pressure driven flow (Conder et al., 2002; Katz, 2010; Toomey et al., 2002). Additionally, a sharp increase in seismic velocity (Byrnes et al., 2017) and decrease in seismic attenuation (Eilon and Abers, 2017) with eastward distance from the ridge further supports active upwelling. The asymmetry and seismic velocity gradient are all imaged in Casc19-S, but our model also shows hints of a low velocity conduit through the upper mantle, coincident with Axial Volcano, the current expression of the Cobb hotspot. The Cobb hotspot is characterized by many of the features of a classic mantle plume: age progressive volcanism that extends away from current volcanism in the direction of plate motion (Desonie and Duncan, 1990), inferred melting depths that are consistent with eruption on progressively younger oceanic lithosphere (Chadwick et al., 2014), and seismic velocities, gravity, and bathymetry that all suggest elevated mantle temperatures

beneath Axial Volcano (Hooft and Detrick, 1995; Rychert et al., 2018). Thus, while it appears reasonable to conclude that active upwelling plays an important role at the Juan de Fuca ridge, the possibility that this is controlled by the local Cobb hotspot and potential plume makes it difficult to draw conclusions about mid-ocean ridges generally.

The precise nature of the oceanic lithosphere-asthenosphere boundary is of critical importance in understanding the role that the convecting mantle plays in the motions of tectonic plates. In Chapter 2, and in great detail in Chapter 3, we discuss the implications of a low-velocity "roll" beneath the hinge of the subducting plate. While we do not image the oceanic lithosphere-asthenosphere boundary directly, we show that a thin, weak layer at the base of a tectonic plate—a layer suggested in other studies (Hu et al., 2016; Kawakatsu et al., 2009; Lin et al., 2016; Naif et al., 2013; Stern et al., 2015)—will accumulate in the hinge, unable to descend as a result of its own buoyancy. Not only does this layer have consequences for the nature of the plate interface (e.g., Bodmer et al., 2018), but it also suggests that the base of the Juan de Fuca plate may be defined by this weak layer. Such a layer has profound implications for plate dynamics, and so determining the thickness, viscosity contrast, and global extent of this layer is of key importance to the Earth Science community in the coming years.

The Cascadia Subduction Zone is where the Juan de Fuca plate sinks below the surface of the earth, and where it interacts most directly with North America. It has produced in the past—and will produce again in the future—earthquakes as large as magnitude 9 (Goldfinger et al., 2012). We discuss in Chapter 2 the intriguing pattern of segmentation along the subduction interface, which may offer clues to the nature of large magnitude earthquakes on the megathrust interface. The segmentation is visible in an extraordinary range of datasets, that span from the sediment structure to the west of the subduction zone (Divins, 2003) to the back arc basin to the east of the Cascade Volcanos (e.g., Casc19-S), and from the surface of North America (Tréhu et al., 1994), through the mantle beneath North America (Mitchell and Asmerom, 2011; Schmidt et al., 2008) and beneath Juan de Fuca (Bodmer et al., 2018), to the structure of the plate at depth (e.g., Casc19-S). We are unable to find a single cause that explains the segmentation in each and every dataset, but we suggest that the segmentation is likely caused by the coincidental alignment of two key features—the Siletz terrane in the North American forearc, and the Basin and Range province east of the Cascades.

Finally, the interaction of the subducted slab with the surrounding mantle, and its effect on the overriding North American plate are mentioned in Chapter 2, and detailed in Chapter 4. We show how a hole observed in the tomographically imaged Juan de Fuca slab is coincident with the High Lava Plains, a region of anomalous age-progressive volcanism in eastern and central Oregon (Jordan, 2005). We show that this progression, when mapped to the Juan de Fuca plate, closely aligns with a pseudofault (Wilson, 2002), a known zone of weakness in the Juan de Fuca plate (Canales et al., 2017; Horning et al., 2016; Nedimović

et al., 2009). We suggest that tearing of the slab as it undergoes rollback causes upwelling in the mantle, and produces volcanism on the surface. This tearing also causes clockwise rotation of the southern portion of the slab, and contributes to the deformation of the Gorda region of the unsubducted Juan de Fuca plate (e.g., Wilson, 1989). This feedback process—that a weak zone in a plate, inherited from its creation at the ridge, can result in fragmentation in the mantle, and that fragmentation can, in turn, drive deformation back at the surface—is a new and complicated story. It implies that the fragmentation and capture, and potentially the accretion, of oceanic plates is a process that is controlled from the bottom up, rather from the top down.

Each of these research topics, in their own right, paint a more complete picture of the Juan de Fuca plate, and how it interacts with the North American plate. But the small size of the Juan de Fuca plate, and the >150 Ma history of the interaction between it and the North American plate, has allowed us to gain new insight on fundamental questions of plate tectonics. In this work, we have advanced, but not solved these problems. But it is clear that seismic data from large swaths of the ocean floor have opened the door to a whole new understanding of Earth dynamics, and represents an exciting, fruitful new direction for Earth Science.

Bibliography

G. A. Abers, L. S. MacKenzie, S. Rondenay, Z. Zhang, A. G. Wech, and K. C. Creager. Imaging the source region of Cascadia tremor and intermediate-depth earthquakes. *Geology*, 37(12):1119–1122, Dec 2009. ISSN 0091-7613. doi: 10.1130/G30143A.1. URL http://geology.gsapubs.org/cgi/doi/10.1130/G30143A.1.

K. Aki and W. H. K. Lee. Determination of three-dimensional velocity anomalies under a seismic array using first P arrival times from local earthquakes: 1. A homogeneous initial model. *Journal of Geophysical Research*, 81(23):4381–4399, Aug 1976. ISSN 01480227. doi: 10.1029/JB081i023p04381. URL http://doi.wiley.com/10.1029/JB081i023p04381.

T. Atwater. Implications of Plate Tectonics for the Cenozoic Tectonic Evolution of Western North America. *Geological Society of America Bulletin*, 81(12): 3513, 1970. ISSN 0016-7606. doi: 10.1130/0016-7606(1970)81[3513:IOPTFT]2.0.CO;2. URL http://gsabulletin.gsapubs.org/cgi/doi/10.1130/0016-7606(1970)81[3513:IOPTFT]2.0.CO;2.

P. Audet and Y. Kim. Teleseismic constraints on the geological environment of deep episodic slow earthquakes in subduction zone forearcs : A review. *Tectonophysics*, 670:1–15, 2016. ISSN 0040-1951. doi: 10.1016/j.tecto.2016.01.005. URL http://dx.doi.org/10.1016/j.tecto.2016.01.005.

P. Audet, M. G. Bostock, N. I. Christensen, and S. M. Peacock. Seismic evidence for overpressured subducted oceanic crust and megathrust fault sealing. *Nature*, 457(7225): 76–78, 2009. ISSN 0028-0836. doi: 10.1038/nature07650. URL http://dx.doi.org/10.1038/nature07650.

P. Audet, M. G. Bostock, D. C. Boyarko, M. R. Brudzinski, and R. M. Allen. Slab morphology in the Cascadia fore arc and its relation to episodic tremor and slip. *Journal of Geophysical Research*, 115(B00A16):1–15, 2010. doi: 10.1029/2008JB006053.

I. D. Bastow. Relative arrival-time upper-mantle tomography and the elusive background mean. *Geophysical Journal International*, 190(2):1271–1278, 2012. ISSN 0956540X. doi: 10.1111/j.1365-246X.2012.05559.x.

T. W. Becker. Superweak asthenosphere in light of upper mantle seismic anisotropy. *Geochemistry, Geophysics, Geosystems*, pages 1–18, May 2017. ISSN 15252027. doi: 10.1002/2017GC006886. URL http://doi.wiley.com/10.1002/2017GC006886.

T. W. Becker, C. P. Conrad, A. J. Schaeffer, and S. Lebedev. Origin of azimuthal seismic anisotropy in oceanic plates and mantle. *Earth and Planetary Science Letters*, 401:236–250, 2014. ISSN 0012821X. doi: 10.1016/j.epsl.2014.06.014. URL http://dx.doi.org/10.1016/j.epsl.2014.06.014.

S. W. Bell, Y. Ruan, and D. W. Forsyth. Ridge asymmetry and deep aqueous alteration at the trench observed from Rayleigh wave tomography of the Juan de Fuca plate. *Journal of Geophysical Research: Solid Earth*, 119:8132–8153, 2016. ISSN 21699313. doi: 10.1002/2016JB012990. URL http://doi.wiley.com/10.1002/2016JB012990.

C. Berk Biryol, S. L. Beck, G. Zandt, and A. A. Özacar. Segmented African lithosphere beneath the Anatolian region inferred from teleseismic P-wave tomography. *Geophysical Journal International*, 184(3):1037–1057, 2011. ISSN 0956540X. doi: 10.1111/j.1365-246X.2010.04910.x.

S. L. Bilek. Invited review paper: Seismicity along the South American subduction zone: Review of large earthquakes, tsunamis, and subduction zone complexity. *Tectonophysics*, 495(1-2):2–14, Nov 2010. ISSN 00401951. doi: 10.1016/j.tecto.2009.02.037. URL http://dx.doi.org/10.1016/j.tecto.2009.02.037.

R. J. Blakely, T. M. Brocher, and R. E. Wells. Subduction-zone magnetic anomalies and implications for hydrated forearc mantle. *Geology*, 33(6):445, 2005. ISSN 0091-7613. doi: 10.1130/G21447.1. URL https://pubs.geoscienceworld.org/geology/article/33/6/445-448/103771.

M. Bodmer, D. R. Toomey, E. E. E. Hooft, J. Nábělek, and J. Braunmiller. Seismic anisotropy beneath the Juan de Fuca plate system: Evidence for heterogeneous mantle flow. *Geology*, 43(12):1095–1098, 2015. ISSN 19432682. doi: 10.1130/G37181.1.

M. Bodmer, D. R. Toomey, E. E. E. Hooft, and B. Schmandt. Buoyant Asthenosphere Beneath Cascadia Influences Megathrust Segmentation. *Geophysical Research Letters*, pages 6954–6962, 2018. ISSN 19448007. doi: 10.1029/2018GL078700.

M. G. Bostock. Tectonophysics The Moho in subduction zones. *Tectonophysics*, 609:547–557, 2013. ISSN 0040-1951. doi: 10.1016/j.tecto.2012.07.007. URL http://dx.doi.org/10.1016/j.tecto.2012.07.007.

M. G. Bostock, R. D. Hyndman, S. Rondenay, and S. M. Peacock. An inverted continental Moho and serpentinization of the forearc mantle. *Nature*, 417(6888):536–538, May 2002. ISSN 0028-0836. doi: 10.1038/417536a. URL http://www.nature.com/articles/417536a.

M. R. Brudzinski and R. M. Allen. Segmentation in episodic tremor and slip all along Cascadia. *Geology*, 35(10):907–910, 2007. ISSN 00917613. doi: 10.1130/G23740A.1.

B. C. Burchfiel, D. S. Cowan, and G. A. Davis. Tectonic overview of the Cordilleran orogen in the western United States. In B. C. Burchfiel, P. W. Lipman, and M. L. Zoback, editors, *The Cordillerian Orogen: Conterminous U.S.*, pages 422–431. Geological Society of America, Boulder, CO, 1992.

R. J. Burgette, R. J. Weldon II, and D. A. Schmidt. Interseismic uplift rates for western Oregon and along-strike variation in locking on the Cascadia subduction zone. *Journal of Geophysical Research*, 114(B01408):1–24, 2009. doi: 10.1029/2008JB005679.

E. R. Burkett and M. I. Billen. Dynamics and implications of slab detachment due to ridge-trench collision. *Journal of Geophysical Research: Solid Earth*, 114(12):1–16, 2009. ISSN 21699356. doi: 10.1029/2009JB006402.

J. S. Byrnes, D. R. Toomey, E. E. E. Hooft, J. Nábělek, and J. Braunmiller. Mantle dynamics beneath the discrete and diffuse plate boundaries of the Juan de Fuca plate: Results from Cascadia Initiative body wave tomography. *Geochemistry, Geophysics, Geosystems*, 18 (8):2906–2929, 2017. ISSN 15252027. doi: 10.1002/2017GC006980.

V. E. Camp and M. E. Ross. Mantle dynamics and genesis of mafic magmatism in the intermontane Pacific Northwest. *Journal of Geophysical Research: Solid Earth*, 109 (B08204):1–14, aug 2004. ISSN 01480227. doi: 10.1029/2003JB002838. URL `http://doi.wiley.com/10.1029/2003JB002838`.

J. P. Canales, S. M. Carbotte, M. R. Nedimović, and H. Carton. Dry Juan de Fuca slab revealed by quantification of water entering Cascadia subduction zone. *Nature Geoscience*, 10(11):864–870, 2017. ISSN 17520908. doi: 10.1038/NGEO3050.

J. Chadwick, R. Keller, G. Kamenov, G. Yogodzinski, and J. Lupton. The Cobb hot spot: HIMU-DMM mixing and melting controlled by a progressively thinning lithospheric lid. *Geochemistry, Geophysics, Geosystems*, 15(8):3107–3122, Aug 2014. ISSN 15252027. doi: 10.1002/2014GC005334. URL `http://doi.wiley.com/10.1002/2014GC005334`.

J. D. Chaytor, C. Goldfinger, R. P. Dziak, and C. G. Fox. Active deformation of the Gorda plate: Constraining deformation models with new geophysical data. *Geology*, 32(4):353–356, 2004. ISSN 00917613. doi: 10.1130/G20178.2.

C. Chen, D. Zhao, and S. Wu. Tomographic imaging of the Cascadia subduction zone: Constraints on the Juan de Fuca slab. *Tectonophysics*, 647-648:73–88, Apr 2015. ISSN 00401951. doi: 10.1016/j.tecto.2015.02.012. URL `http://dx.doi.org/10.1016/j.tecto.2015.02.012`.

C. Cheng, T. Bodin, B. Tauzin, and R. M. Allen. Cascadia subduction slab heterogeneity revealed by three-dimensional receiver function Kirchhoff migration. *Geophysical Research Letters*, 44(2):694–701, Jan 2017. ISSN 00948276. doi: 10.1002/2016GL072142. URL `http://doi.wiley.com/10.1002/2016GL072142`.

J. A. Conder, D. W. Forsyth, and E. M. Parmentier. Asthenospheric flow and asymmetry of the East Pacific Rise, MELT area. *Journal of Geophysical Research: Solid Earth*, 107 (B12), Dec 2002. ISSN 01480227. doi: 10.1029/2001JB000807. URL `http://doi.wiley.com/10.1029/2001JB000807`.

C. H. Craig and D. P. McKenzie. The existence of a thin low-viscosity layer beneath the lithosphere. *Earth and Planetary Science Letters*, 78(4):420–426, 1986. ISSN 0012821X. doi: 10.1016/0012-821X(86)90008-7.

F. A. Dahlen, S. H. Hung, and G. Nolet. Fréchet kernels for finite-frequency traveltimes-I. Theory. *Geophysical Journal International*, 141(1):157–174, Apr 2000. ISSN 0956540X. doi: 10.1046/j.1365-246X.2000.00070.x. URL `http://doi.wiley.com/10.1046/j.1365-246X.2000.00070.x`.

A. Darold and E. D. Humphreys. Upper mantle seismic structure beneath the Pacific Northwest: A plume-triggered delamination origin for the Columbia River flood basalt eruptions. *Earth and Planetary Science Letters*, 365, 2013.

J. R. Delph, A. Levander, and F. Niu. Fluid Controls on the Heterogeneous Seismic Characteristics of the Cascadia Margin. *Geophysical Research Letters*, 45(20):11,021–11,029, oct 2018. ISSN 00948276. doi: 10.1029/2018GL079518. URL `http://doi.wiley.com/10.1029/2018GL079518`.

C. DeMets, R. G. Gordon, and D. F. Argus. Geologically current plate motions. *Geophysical Journal International*, 181(1):1–80, 2010. ISSN 0956540X. doi: 10.1111/j.1365-246X.2009.04491.x.

D. L. Desonie and R. A. Duncan. The Cobb-Eickelberg Seamount Chain: Hotspot volcanism with mid-ocean ridge basalt affinity. *Journal of Geophysical Research*, 95(B8):12697, 1990. ISSN 0148-0227. doi: 10.1029/JB095iB08p12697. URL `http://doi.wiley.com/10.1029/JB095iB08p12697`.

R. S. Dietz. Continent and ocean basin evolution by spreading of the sea floor. *Nature*, 190 (4779):854–857, 1961.

D. L. Divins. Total Sediment Thickness of the World's Oceans and Marginal Seas. *NOAA Natl. Geophys. Data Cent., Boulder, Colo.*, 2003.

C. Doglioni, A. Ismail-Zadeh, G. F. Panza, and F. Riguzzi. Lithosphere-asthenosphere viscosity contrast and decoupling. *Physics of the Earth and Planetary Interiors*, 189(1-2): 1–8, 2011. ISSN 00319201. doi: 10.1016/j.pepi.2011.09.006.

K. A. Druken, M. D. Long, and C. Kincaid. Patterns in seismic anisotropy driven by rollback subduction beneath the High Lava Plains. *Geophysical Research Letters*, 38(L13310):1–6, 2011. doi: 10.1029/2011GL047541.

C. M. Eakin, M. Obrebski, R. M. Allen, D. C. Boyarko, M. R. Brudzinski, and R. W. Porritt. Seismic anisotropy beneath Cascadia and the Mendocino triple junction: Interaction of the subducting slab with mantle flow. *Earth and Planetary Science Letters*, 297(3-4):627–632, 2010. ISSN 0012821X. doi: 10.1016/j.epsl.2010.07.015. URL `http://dx.doi.org/10.1016/j.epsl.2010.07.015`.

Z. C. Eilon and G. A. Abers. High seismic attenuation at a mid-ocean ridge reveals the distribution of deep melt. *Science Advances*, 3(5), May 2017. ISSN 2375-2548. doi: 10.1126/sciadv.1602829. URL `http://advances.sciencemag.org/lookup/doi/10.1126/sciadv.1602829`.

G. Ekström. Love and Rayleigh phase-velocity maps, 5–40 s, of the western and central USA from USArray data. *Earth and Planetary Science Letters*, 402(C):42–49, Sep 2014. ISSN 0012821X. doi: 10.1016/j.epsl.2013.11.022. URL `http://dx.doi.org/10.1016/j.epsl.2013.11.022`.

R. L. Evans, P. E. Wannamaker, R. S. McGary, and J. Elsenbeck. Electrical structure of the central Cascadia subduction zone: The EMSLAB Lincoln Line revisited. *Earth and Planetary Science Letters*, 402(C):265–274, 2014. ISSN 0012821X. doi: 10.1016/j.epsl.2013.04.021.

U. H. Faul and I. Jackson. The seismological signature of temperature and grain size variations in the upper mantle. *Earth and Planetary Science Letters*, 234(1-2):119–134, May 2005. ISSN 0012821X. doi: 10.1016/j.epsl.2005.02.008. URL `https://linkinghub.elsevier.com/retrieve/pii/S0012821X05001044`.

M. A. Feighner and M. A. Richards. The fluid dynamics of plume-ridge and plume-plate interactions: An experimental investigation. *Earth and Planetary Science Letters*, 129 (1-4):171–182, Jan 1995. ISSN 0012821X. doi: 10.1016/0012-821X(94)00247-V. URL `http://linkinghub.elsevier.com/retrieve/pii/0012821X9400247V`.

K. M. Fischer, H. A. Ford, D. L. Abt, and C. A. Rychert. The Lithosphere-Asthenosphere Boundary. *Annual Review of Earth and Planetary Sciences*, 38(1):551–575, 2010. ISSN 0084-6597. doi: 10.1146/annurev-earth-040809-152438. URL `http://www.annualreviews.org/doi/abs/10.1146/annurev-earth-040809-152438`.

M. T. Ford, A. L. Grunder, and R. A. Duncan. Bimodal volcanism of the High Lava Plains and Northwestern Basin and Range of Oregon: Distribution and tectonic implications of age-progressive rhyolites. *Geochemistry, Geophysics, Geosystems*, 14(8):2836–2857, 2013. ISSN 15252027. doi: 10.1002/ggge.20175.

D. A. Foster, P. A. Mueller, D. W. Mogk, J. L. Wooden, and J. J. Vogl. Proterozoic evolution of the western margin of the Wyoming craton: implications for the tectonic and magmatic evolution of the northern Rocky Mountains. *Canadian Journal of Earth Sciences*, 43: 1601–1619, 2006. doi: 10.1139/E06-052.

A. M. Freed, A. Hashima, T. W. Becker, D. A. Okaya, H. Sato, and Y. Hatanaka. Resolving depth-dependent subduction zone viscosity and afterslip from postseismic displacements following the 2011 Tohoku-oki, Japan earthquake. *Earth and Planetary Science Letters*, 459:279–290, 2017. ISSN 0012821X. doi: 10.1016/j.epsl.2016.11.040. URL `http://dx.doi.org/10.1016/j.epsl.2016.11.040`.

C. Frohlich, W. Gan, and R. B. Herrmann. Two Deep Earthquakes in Wyoming. *Seismological Research Letters*, 86(3):810–818, 2015. ISSN 0895-0695. doi: 10.1785/0220140197. URL `https://pubs.geoscienceworld.org/srl/article/86/3/810-818/315610`.

K. P. Furlong and S. Y. Schwartz. Influence of the Mendocino Triple Junction on the Tectonics of Coastal California. *Annual Review of Earth and Planetary Sciences*, 32(1):403–433, 2004. ISSN 0084-6597. doi: 10.1146/annurev.earth.32.101802.120252. URL `http://www.annualreviews.org/doi/abs/10.1146/annurev.earth.32.101802.120252`.

H. Gao. Seismic velocity structure of the Juan de Fuca and Gorda plates revealed by a joint inversion of ambient noise and regional earthquakes. *Geophysical Research Letters*, May 2016. ISSN 00948276. doi: 10.1002/2016GL069381. URL `http://doi.wiley.com/10.1002/2016GL069381`.

H. Gao. Three-dimensional variations of the slab geometry correlate with earthquake distributions at the Cascadia subduction system. *Nature Communications*, 9(1):1–8, 2018. ISSN 2041-1723. doi: 10.1038/s41467-018-03655-5. URL `http://dx.doi.org/10.1038/s41467-018-03655-5`.

D. J. Geist and M. A. Richards. Origin of the Columbia Plateau and Snake River Plain: Deflection of the Yellowstone Plume. *Geology*, 21:789–792, 1993.

C. Goldfinger, C. H. Nelson, A. E. Morey, J. E. Johnson, J. Patton, E. Karabanov, J. Gutierrez-Pastor, A. Eriksson, E. Gracia, G. Dunhill, R. Enkin, A. Dallimore, and T. Valiier. Turbidite Event History–Methods and Implications for Holocene Paleoseismicity of the Cascadia Subduction Zone. *U.S. Geological Survey Professional Paper 1661-F*, page 170 p., 2012. URL `https://pubs.usgs.gov/pp/pp1661f/`.

D. W. Graham, M. R. Reid, B. T. Jordan, A. L. Grunder, W. P. Leeman, and J. E. Lupton. Mantle source provinces beneath the Northwestern USA delimited by helium isotopes in young basalts. *Journal of Volcanology and Geothermal Research*, 188(1-3):128–140, 2009. ISSN 03770273. doi: 10.1016/j.jvolgeores.2008.12.004.

T. C. Hales, D. L. Abt, E. D. Humphreys, and J. J. Roering. A lithospheric instability origin for Columbia River flood basalts and Wallowa Mountains uplift in northeast Oregon. *Nature*, 438:842–845, 2005. doi: 10.1038/nature04313.

S. Han, S. M. Carbotte, J. P. Canales, M. R. Nedimović, H. Carton, J. C. Gibson, and G. W. Horning. Seismic reflection imaging of the Juan de Fuca plate from ridge to trench: New constraints on the distribution of faulting and evolution of the crust prior to subduction. *Journal of Geophysical Research: Solid Earth*, 121(3):1849–1872, Mar 2016. ISSN 21699313. doi: 10.1002/2015JB012416. URL `http://doi.wiley.com/10.1002/2015JB012416`.

R. T. J. Hansen, M. G. Bostock, and N. I. Christensen. Nature of the low velocity zone in Cascadia from receiver function waveform inversion. *Earth and Planetary Science Letters*, 337-338:25–38, 2012. ISSN 0012821X. doi: 10.1016/j.epsl.2012.05.031. URL `http://dx.doi.org/10.1016/j.epsl.2012.05.031`.

W. B. Hawley and R. M. Allen. The Fragmented Death of the Farallon Plate. *Geophysical Research Letters*, 46(2019GL083437), Jul 2019. ISSN 0094-8276. doi: 10.1029/2019GL083437. URL `https://onlinelibrary.wiley.com/doi/abs/10.1029/2019GL083437`.

W. B. Hawley, R. M. Allen, and M. A. Richards. Tomography reveals buoyant asthenosphere accumulating beneath the Juan de Fuca plate. *Science*, 353(6306):1406–1408, Sep 2016. ISSN 0036-8075. doi: 10.1126/science.aad8104. URL `http://www.sciencemag.org/cgi/doi/10.1126/science.aad8104`.

H. H. Hess. History of Ocean Basins. In A. E. J. Engel, H. L. James, and B. F. Leonard, editors, *Petrologic Studies*, pages 599–620. Geological Society of America, 1962. ISBN 9780813759425. doi: 10.1130/Petrologic.1962.599. URL `https://pubs.geoscienceworld.org/books/book/847/chapter/3918672/`.

R. Hey. A new class of "pseudofaults" and their bearing on plate tectonics: A propagating rift model. *Earth and Planetary Science Letters*, 37(2):321–325, 1977. ISSN 0012821X. doi: 10.1016/0012-821X(77)90177-7.

N. Hirano, E. Takahashi, J. Yamamoto, N. Abe, S. P. Ingle, I. Kaneoka, T. Hirata, J.-I. Kimura, T. Ishii, Y. Ogawa, S. Machida, and K. Suyehiro. Volcanism in response to plate flexure. *Science*, 313(5792):1426–1428, 2006. ISSN 0036-8075. doi: 10.1126/science.1128235. URL `http://www.sciencemag.org/cgi/doi/10.1126/science.1128235`.

M. M. Hirschmann. Partial melt in the oceanic low velocity zone. *Physics of the Earth and Planetary Interiors*, 179(1-2):60–71, Mar 2010. ISSN 00319201. doi: 10.1016/j.pepi.2009.12.003. URL `http://dx.doi.org/10.1016/j.pepi.2009.12.003`.

G. Hirth and D. L. Kohlstedt. Water in the oceanic upper mantle: implications for rheology, melt extraction and the evolution of the lithosphere. *Earth and Planetary Science Letters*, 144(1-2):93–108, 1996. ISSN 0012821X. doi: 10.1016/0012-821X(96)00154-9.

P. F. Hoffman. United Plates of America, The Birth of a Craton: Early Proterozoic Assembly and Growth of Laurentia. *Annual Review of Earth and Planetary Sciences*, 16(1):543–603, May 1988. ISSN 0084-6597. doi: 10.1146/annurev.ea.16.050188.002551. URL `http://www.annualreviews.org/doi/10.1146/annurev.ea.16.050188.002551`.

T. Höink and A. Lenardic. Long wavelength convection, Poiseuille-Couette flow in the low-viscosity asthenosphere and the strength of plate margins. *Geophysical Journal International*, 180(1):23–33, 2010. ISSN 0956540X. doi: 10.1111/j.1365-246X.2009.04404.x.

J. A. Hole, B. C. Beaudoin, and T. J. Henstock. Wide-angle seismic constraints on the evolution of the deep San Andreas plate boundary by Mendocino triple junction migration. *Tectonics*, 17(5):802–818, 1998. ISSN 02787407. doi: 10.1029/98TC02261. URL `http://dx.doi.org/10.1029/98TC02261`.

E. E. E. Hooft and R. S. Detrick. Relationship between axial morphology, crustal thickness, and mantle temperature along the Juan de Fuca and Gorda Ridges. *Journal of Geophysical Research*, 100(B11):22499–22508, 1995.

E. Hopper, H. A. Ford, K. M. Fischer, V. Lekić, and M. J. Fouch. The lithosphere-asthenosphere boundary and the tectonic and magmatic history of the northwestern United States. *Earth and Planetary Science Letters*, 402(C):69–81, 2014. ISSN 0012821X. doi: 10.1016/j.epsl.2013.12.016. URL `http://dx.doi.org/10.1016/j.epsl.2013.12.016`.

G. W. Horning, J. P. Canales, S. M. Carbotte, S. Han, H. Carton, M. R. Nedimović, and P. E. van Keken. A 2-D tomographic model of the Juan de Fuca plate from accretion at axial seamount to subduction at the Cascadia margin from an active source ocean bottom seismometer survey. *Journal of Geophysical Research: Solid Earth*, 121(8):5859–5879, Aug 2016. ISSN 21699313. doi: 10.1002/2016JB013228. URL `http://doi.wiley.com/10.1002/2016JB013228`.

Y. Hu, R. Bürgmann, P. Banerjee, L. Feng, E. M. Hill, T. Ito, T. Tabei, and K. Wang. Asthenosphere rheology inferred from observations of the 2012 Indian Ocean earthquake. *Nature*, pages 1–17, 2016. ISSN 0028-0836. doi: 10.1038/nature19787. URL `http://www.nature.com/doifinder/10.1038/nature19787`.

E. D. Humphreys and D. D. Coblentz. North American Dynamics and Western U.S. Tectonics. *Reviews of Geophysics*, 45(RG3001):1–30, 2007. doi: 10.1029/2005RG000181.

E. D. Humphreys and B. H. Hager. A kinematic model for the recent development of southern California crust and upper mantle Model for the Late Cenozoic Development of Southern California Crust and Upper Mantle. *Journal of Geophysical Research*, 95(B12): 19747–19762, 1990.

S. E. Ingebritsen and R. H. Mariner. Hydrothermal heat discharge in the Cascade Range, northwestern United States. *Journal of Volcanology and Geothermal Research*, 196(3-4): 208–218, 2010. ISSN 03770273. doi: 10.1016/j.jvolgeores.2010.07.023.

M. A. Jadamec and M. I. Billen. The role of rheology and slab shape on rapid mantle flow : Three-dimensional numerical models of the Alaska slab edge. *Journal of Geophysical Research*, 117(B02304), 2012. doi: 10.1029/2011JB008563.

D. E. James, M. J. Fouch, R. W. Carlson, and J. B. Roth. Slab fragmentation, edge flow and the origin of the Yellowstone hotspot track. *Earth and Planetary Science Letters*, 311: 124–135, 2011. ISSN 0012-821X. doi: 10.1016/j.epsl.2011.09.007. URL `http://dx.doi.org/10.1016/j.epsl.2011.09.007`.

H. A. Janiszewski and G. A. Abers. Imaging the Plate Interface in the Cascadia Seismogenic Zone: New Constraints from Offshore Receiver Functions. *Seismological Research Letters*, 86(5):1261–1269, 2015. ISSN 0895-0695. doi: 10.1785/0220150104. URL `http://srl.geoscienceworld.org/lookup/doi/10.1785/0220150104`.

B. T. Jordan. Age-progressive volcanism of the Oregon High Lava Plains; overview and evaluation of tectonic models. *Special Paper - Geological Society of America*, 388(30): 503–515, 2005. ISSN 0072-1077. doi: 10.1130/0-8137-2388-4.503. URL `http://dx.doi.org/10.1130/0-8137-2388-4.503`.

S.-i. Karato and H. Jung. Water, partial melting and the origin of the seismic low velocity and high attenuation zone in the upper mantle. *Earth and Planetary Science Letters*, 157 (3-4):193–207, 1998. ISSN 0012821X. doi: 10.1016/S0012-821X(98)00034-X.

K. E. Karlstrom, D. Coblentz, K. Dueker, W. Ouimet, E. Kirby, J. Van Wijk, B. Schmandt, S. Kelley, G. Lazear, L. J. Crossey, R. S. Crow, A. Aslan, A. Darling, R. C. Aster, J. MacCarthy, S. M. Hansen, J. Stachnik, D. F. Stockli, R. V. Garcia, M. Hoffman, R. McKeon, J. Feldman, M. Heizler, and M. S. Donahue. Mantle-driven dynamic uplift of the Rocky Mountains and Colorado Plateau and its surface response: Toward a unified hypothesis. *Lithosphere*, 4(1):3–22, 2012. ISSN 1941-8264. doi: 10.1130/L150.1. URL `https://pubs.geoscienceworld.org/lithosphere/article/4/1/3-22/145610`.

R. F. Katz. Porosity-driven convection and asymmetry beneath mid-ocean ridges. *Geochemistry, Geophysics, Geosystems*, 11(Q0AC07), 2010. doi: 10.1029/2010GC003282.

H. Kawakatsu. At the Bottom of the Oceanic Plate. *Science*, 335(6075):1448–1449, mar 2012. ISSN 0036-8075. doi: 10.1126/science.1219658. URL `http://www.sciencemag.org/cgi/doi/10.1126/science.1219658`.

H. Kawakatsu, P. Kumar, Y. Takei, M. Shinohara, T. Kanazawa, E. Araki, and K. Suyehiro. Seismic evidence for sharp lithosphere-asthenosphere boundaries of oceanic plates. *Science*, 324(5926):499–502, 2009. ISSN 1095-9203. doi: 10.1126/science.1169499. URL `https://dx.doi.org/10.1126/science.1169499`.

T. Keller, R. F. Katz, and M. M. Hirschmann. Volatiles beneath mid-ocean ridges: Deep melting, channelised transport, focusing, and metasomatism. *Earth and Planetary Science Letters*, 464:55–68, apr 2017. ISSN 0012821X. doi: 10.1016/j.epsl.2017.02.006. URL `http://dx.doi.org/10.1016/j.epsl.2017.02.006`.

B. Kennett and E. R. Engdahl. Traveltimes for global earthquake location and phase identification. *Geophysical Journal International*, 105(2):429–465, 1991. doi: 10.1111/j.1365-246X.1991.tb06724.x.

A. H. Lachenbruch and J. H. Sass. Heat flow and energetics of the San Andreas Fault Zone. *Journal of Geophysical Research: Solid Earth*, 85(B11):6185–6222, Nov 1980. ISSN 01480227. doi: 10.1029/JB085iB11p06185. URL `http://doi.wiley.com/10.1029/JB085iB11p06185`.

A. Levander, B. Schmandt, M. S. Miller, K. Liu, K. E. Karlstrom, R. S. Crow, C.-T. A. Lee, and E. D. Humphreys. Continuing Colorado plateau uplift by delamination-style convective lithospheric downwelling. *Nature*, 472(7344):461–465, 2011. ISSN 0028-0836. doi: 10.1038/nature10001. URL `http://dx.doi.org/10.1038/nature10001`.

B. T. R. Lewis and L. M. Dorman. Recording teleseisms on the seafloor; an example from the Juan de Fuca plate. *Bulletin of the Seismological Society of America*, 88(1):107–116, 1998. ISSN 00371106.

P.-Y. P. Lin, J. B. Gaherty, G. Jin, J. A. Collins, D. Lizarralde, R. L. Evans, and G. Hirth. High-resolution seismic constraints on flow dynamics in the oceanic asthenosphere. *Nature*, Jul 2016. ISSN 0028-0836. doi: 10.1038/nature18012. URL `http://www.nature.com/doifinder/10.1038/nature18012`.

L. Liu and M. Gurnis. Dynamic subsidence and uplift of the Colorado Plateau. *Geology*, 38 (7):663–666, 2010. ISSN 00917613. doi: 10.1130/G30624.1.

L. Liu and D. R. Stegman. Segmentation of the Farallon slab. *Earth and Planetary Science Letters*, 311(1-2):1–10, 2011. ISSN 0012821X. doi: 10.1016/j.epsl.2011.09.027. URL `http://dx.doi.org/10.1016/j.epsl.2011.09.027`.

L. Liu and D. R. Stegman. Origin of Columbia River flood basalt controlled by propagating rupture of the Farallon slab. *Nature*, 482(7385):386–389, 2012. ISSN 0028-0836. doi: 10.1038/nature10749. URL `http://dx.doi.org/10.1038/nature10749`.

L. Liu, M. Gurnis, M. Seton, J. Saleeby, R. D. Müller, and J. M. Jackson. The role of oceanic plateau subduction in the Laramide orogeny. *Nature Geoscience*, 3(5):353–357, 2010. ISSN 1752-0894. doi: 10.1038/ngeo829. URL `http://www.nature.com/doifinder/10.1038/ngeo829`.

M. D. Long and P. G. Silver. The Subduction Zone Flow Field from Seismic Anisotropy: A Global View. *Science*, 319(5861):315–318, Jan 2008. ISSN 0036-8075. doi: 10.1126/science.1150809. URL `http://www.sciencemag.org/cgi/doi/10.1126/science.1150809`.

M. D. Long and P. G. Silver. Shear wave splitting and mantle anisotropy: Measurements, interpretations, and new directions. *Surveys in Geophysics*, 30(4-5):407–461, 2009. ISSN 01693298. doi: 10.1007/s10712-009-9075-1.

M. D. Long, H. Gao, A. Klaus, L. S. Wagner, M. J. Fouch, D. E. James, and E. D. Humphreys. Shear wave splitting and the pattern of mantle flow beneath eastern Oregon. *Earth and Planetary Science Letters*, 288(3-4):359–369, Nov 2009. ISSN 0012821X. doi: 10.1016/j.epsl.2009.09.039. URL `http://dx.doi.org/10.1016/j.epsl.2009.09.039`.

M. D. Long, C. B. Till, K. A. Druken, R. W. Carlson, L. S. Wagner, M. J. Fouch, D. E. James, T. L. Grove, N. Schmerr, and C. Kincaid. Mantle dynamics beneath the Pacific Northwest and the generation of voluminous back-arc volcanism. *Geochemistry, Geophysics, Geosystems*, 13(8), Aug 2012. ISSN 15252027. doi: 10.1029/2012GC004189. URL `http://doi.wiley.com/10.1029/2012GC004189`.

M. Marjanović, S. M. Carbotte, M. R. Nedimović, and J. P. Canales. Gravity and seismic study of crustal structure along the Juan de Fuca Ridge axis and across pseudofaults on the ridge flanks. *Geochemistry, Geophysics, Geosystems*, 12(5):1–22, 2011. ISSN 15252027. doi: 10.1029/2010GC003439.

R. Martin-Short, R. M. Allen, I. D. Bastow, E. Totten, and M. A. Richards. Mantle flow geometry from ridge to trench beneath the Gorda–Juan de Fuca plate system. *Nature Geoscience*, 8(December):1–21, 2015. ISSN 1752-0894. doi: 10.1038/ngeo2569. URL `http://www.nature.com/doifinder/10.1038/ngeo2569`.

P. A. McCrory, J. L. Blair, F. Waldhauser, and D. H. Oppenheimer. Juan de Fuca slab geometry and its relation to Wadati-Benioff zone seismicity. *Journal of Geophysical Research: Solid Earth*, 117(9):1–23, 2012. ISSN 21699356. doi: 10.1029/2012JB009407.

D. P. McKenzie. Speculations on the Consequences and Causes of Plate Motions. *Geophysical Journal of the Royal Astronomical Society*, 18:1–32, 1969.

D. P. McKenzie and R. L. Parker. The North Pacific: an Example of Tectonics on a Sphere. *Nature*, 216(5122):1276–1280, 1967. ISSN 0028-0836. doi: 10.1038/2161276a0.

MELT Seismic Team. Imaging the Deep Seismic Structure Beneath a Mid-Ocean Ridge : The MELT Experiment. *Science*, 280(5367):1215–1220, 1998.

E. C. Mitchell and Y. Asmerom. U-series isotope systematics of mafic magmas from central Oregon: Implications for fluid involvement and melting processes in the Cascade arc. *Earth and Planetary Science Letters*, 312(3-4):378–389, 2011. ISSN 0012821X. doi: 10.1016/j.epsl.2011.09.060. URL `http://dx.doi.org/10.1016/j.epsl.2011.09.060`.

R. Moucha, A. M. Forte, D. B. Rowley, J. X. Mitrovica, N. A. Simmons, and S. P. Grand. Deep mantle forces and the uplift of the Colorado Plateau. *Geophysical Research Letters*, 36(L19310):1–6, 2009. ISSN 00948276. doi: 10.1029/2009GL039778.

S. Naif, K. Key, S. Constable, and R. L. Evans. Melt-rich channel observed at the lithosphere-asthenosphere boundary. *Nature*, 495(7441):356–9, 2013. ISSN 1476-4687. doi: 10.1038/nature11939. URL `https://dx.doi.org/10.1038/nature11939`.

M. R. Nedimović, D. R. Bohnenstiehl, S. M. Carbotte, J. Pablo Canales, and R. P. Dziak. Faulting and hydration of the Juan de Fuca plate system. *Earth and Planetary Science Letters*, 284(1-2):94–102, Jun 2009. ISSN 0012821X. doi: 10.1016/j.epsl.2009.04.013. URL `http://linkinghub.elsevier.com/retrieve/pii/S0012821X09002325`.

C. Nicholson, C. C. Sorlien, T. Atwater, J. C. Crowell, and B. P. Luyendyk. Microplate capture, rotation of the western Transverse Ranges, and initiation of the San Andreas transform as a low-angle fault system. *Geology*, 22(6):491, 1994. ISSN 0091-7613. doi: 10.1130/0091-7613(1994)022⟨0491:MCROTW⟩2.3.CO;2. URL `https://pubs.geoscienceworld.org/geology/article/22/6/491-495/206061`.

M. Obayashi, J. Yoshimitsu, and Y. Fukao. Tearing of Stagnant Slab. *Science*, 324(5931):1173–1175, May 2009. ISSN 0036-8075. doi: 10.1126/science.1172496. URL `http://www.sciencemag.org/cgi/doi/10.1126/science.1172496`.

M. Obrebski, R. M. Allen, M. Xue, and S. H. Hung. Slab-plume interaction beneath the Pacific Northwest. *Geophysical Research Letters*, 37(14), 2010. ISSN 00948276. doi: 10.1029/2010GL043489.

M. Obrebski, R. M. Allen, F. F. Pollitz, and S. H. Hung. Lithosphere-asthenosphere interaction beneath the western United States from the joint inversion of body-wave traveltimes and surface-wave phase velocities. *Geophysical Journal International*, 185(2):1003–1021, 2011. ISSN 0956540X. doi: 10.1111/j.1365-246X.2011.04990.x.

A. Paulson and M. A. Richards. On the resolution of radial viscosity structure in modelling long-wavelength postglacial rebound data. *Geophysical Journal International*, 179(3):1516–1526, Dec 2009. ISSN 1365-246X. doi: 10.1111/j.1365-246X.2009.04362.x.

K. L. Pierce and L. A. Morgan. The track of the Yellowstone hot spot : Volcanism, faulting, and uplift. In P. Link, M. Kuntz, and L. Platt, editors, *Regional Geology of Eastern Idaho and Western Wyoming: Geological Society of America Memoir 179*, chapter 1, pages 1–53. Geological Society of America, 1992.

T. Plank, K. A. Kelley, M. M. Zimmer, E. H. Hauri, and P. J. Wallace. Why do mafic arc magmas contain ∼4 wt % water on average? *Earth and Planetary Science Letters*, 364:168–179, 2013.

R. W. Porritt, R. M. Allen, D. C. Boyarko, and M. R. Brudzinski. Investigation of Cascadia segmentation with ambient noise tomography. *Earth and Planetary Science Letters*, 309 (1-2):67–76, 2011. ISSN 0012821X. doi: 10.1016/j.epsl.2011.06.026. URL `http://dx.doi.org/10.1016/j.epsl.2011.06.026`.

R. W. Porritt, R. M. Allen, and F. F. Pollitz. Seismic imaging east of the Rocky Mountains with USArray. *Earth and Planetary Science Letters*, 402(C):16–25, 2014. ISSN 0012821X. doi: 10.1016/j.epsl.2013.10.034. URL `http://dx.doi.org/10.1016/j.epsl.2013.10.034`.

D. E. Portner, S. L. Beck, G. Zandt, and A. Scire. The nature of subslab slow velocity anomalies beneath South America. *Geophysical Research Letters*, 44(10):4747–4755, may 2017. ISSN 00948276. doi: 10.1002/2017GL073106. URL `http://doi.wiley.com/10.1002/2017GL073106`.

L. A. Preston, K. C. Creager, R. S. Crosson, T. M. Brocher, and A. M. Tréhu. Intrastab Earthquakes: Dehydration of the Cascadia Slab. *Science*, 302(5648):1197–1200, 2003. ISSN 00368075. doi: 10.1126/science.1090751.

M. A. Richards, W.-S. Yang, J. R. Baumgardner, and H.-P. Bunge. Role of a low-viscosity zone in stabilizing plate tectonics: Implications for comparative terrestrial planetology. *Geochemistry, Geophysics, Geosystems*, 2(8), 2001. ISSN 15252027. doi: 10.1029/2000GC000115. URL `http://dx.doi.org/10.1029/2000GC000115`.

G. Rogers and H. Dragert. Episodic Tremor and Slip on the Cascadia Subduction Zone : The Chatter of Silent Slip. *Science*, 300:1942–1943, 2003. doi: 10.1126/science.1084783.

G. Rosenbaum, M. Gasparon, F. P. Lucente, A. Peccerillo, and M. S. Miller. Kinematics of slab tear faults during subduction segmentation and implications for Italian magmatism. *Tectonics*, 27(2):1–16, 2008. ISSN 02787407. doi: 10.1029/2007TC002143.

J. B. Roth, M. J. Fouch, D. E. James, and R. W. Carlson. Three-dimensional seismic velocity structure of the northwestern United States. *Geophysical Research Letters*, 35(L15304): 1–6, 2008. doi: 10.1029/2008GL034669.

D. B. Rowley, A. M. Forte, C. J. Rowan, P. Glišović, R. Moucha, S. P. Grand, and N. A. Simmons. Kinematics and dynamics of the East Pacific Rise linked to a stable, deep-mantle upwelling. *Science Advances*, 2(12):e1601107, 2016. ISSN 2375-2548. doi: 10.1126/sciadv.1601107. URL `http://advances.sciencemag.org/lookup/doi/10.1126/sciadv.1601107`.

M. Roy, T. H. Jordan, and J. Pederson. Colorado Plateau magmatism and uplift by warming of heterogeneous lithosphere. *Nature*, 459(7249):978–982, 2009. ISSN 0028-0836. doi: 10.1038/nature08052. URL `http://www.nature.com/doifinder/10.1038/nature08052`.

L. J. Ruff. Do Trench Sediments Affect Great Earthquake Occurrence in Subduction Zones? *PAGEOPH*, 129(1/2):263–282, 1989.

R. M. Russo. Subducted oceanic asthenosphere and upper mantle flow beneath the Juan de Fuca slab. *Lithosphere*, 1(4):195–205, 2009. ISSN 1941-8264. doi: 10.1130/L41.1.

R. M. Russo and P. G. Silver. Trench-Parallel Flow Beneath the Nazca Plate from Seismic Anisotropy. *Science*, 263:1105–1111, 1994. doi: 10.1126/science.263.5150.1105.

C. A. Rychert and P. M. Shearer. A Global View of the Lithosphere-Asthenosphere Boundary. *Science*, 324(5926):495–498, Apr 2009. ISSN 0036-8075. doi: 10.1126/science.1169754. URL `http://www.sciencemag.org/cgi/doi/10.1126/science.1169754`.

C. A. Rychert, N. Harmon, and S. Tharimena. Scattered wave imaging of the oceanic plate in Cascadia. *Science Advances*, 4(2):eaao1908, Feb 2018. ISSN 2375-2548. doi: 10.1126/sciadv.aao1908. URL `http://advances.sciencemag.org/lookup/doi/10.1126/sciadv.aao1908`.

G. M. Schmalzle, R. Mccaffrey, and K. C. Creager. Central Cascadia Subduction Zone Creep. *Geochemistry, Geophysics, Geosystems*, 15:1515–1532, 2014. doi: 10.1002/2013GC005172. URL `https://dx.doi.org/10.1002/2013GC005172`.

B. Schmandt and E. D. Humphreys. Complex subduction and small-scale convection revealed by body-wave tomography of the western United States upper mantle. *Earth and Planetary Science Letters*, 297(3-4):435–445, 2010. ISSN 0012821X. doi: 10.1016/j.epsl.2010.06.047.

B. Schmandt and F.-C. Lin. P and S wave tomography of the mantle beneath the United States. *Geophysical Research Letters*, 41(18):6342–6349, Sep 2014. ISSN 00948276. doi: 10.1002/2014GL061231. URL `http://doi.wiley.com/10.1002/2014GL061231`.

N. Schmerr. The Gutenberg discontinuity: melt at the lithosphere-asthenosphere boundary. *Science*, 335(6075):1480–1483, 2012. ISSN 0036-8075. doi: 10.1126/science.1215433. URL `https://dx.doi.org/10.1126/science.1215433`.

M. E. Schmidt, A. L. Grunder, and M. C. Rowe. Segmentation of the Cascade Arc as indicated by Sr and Nd isotopic variation among diverse primitive basalts. *Earth and Planetary Science Letters*, 266(1-2):166–181, 2008. ISSN 0012821X. doi: 10.1016/j.epsl.2007.11.013.

J. Severinghaus and T. Atwater. Cenozoic geometry and thermal state of the subducting slabs beneath North America. In B. P. Wernicke, editor, *Basin and Range Extensional Tectonics Near the Latitude of Las Vegas, Nevada*, pages 1–22. Geological Society of America, 1990.

K. Sigloch. Mantle provinces under North America from multifrequency P wave tomography. *Geochemistry, Geophysics, Geosystems*, 12(Q02W08):n/a–n/a, Feb 2011. ISSN 15252027. doi: 10.1029/2010GC003421. URL `http://doi.wiley.com/10.1029/2010GC003421`.

K. Sigloch. Yellowstone debate erupts again. *Nature Geoscience*, 11(6):385–387, 2018. ISSN 17520908. doi: 10.1038/s41561-018-0150-4.

K. Sigloch, N. McQuarrie, and G. Nolet. Two-stage subduction history under North America inferred from multiple-frequency tomography. *Nature Geoscience*, 1:458–462, 2008. doi: 10.1038/ngeo231.

C. R. Sine, D. S. Wilson, W. Gao, S. P. Grand, R. C. Aster, J. Ni, and W. S. Baldridge. Mantle structure beneath the western edge of the Colorado Plateau. *Geophysical Research Letters*, 35(L10303):1–5, 2008. doi: 10.1029/2008GL033391.

T. R. A. Song and H. Kawakatsu. Subduction of oceanic asthenosphere: Evidence from subslab seismic anisotropy. *Geophysical Research Letters*, 39(17):1–6, 2012. ISSN 00948276. doi: 10.1029/2012GL052639.

D. R. Stegman, J. Freeman, W. P. Schellart, L. Moresi, and D. May. Influence of trench width on subduction hinge retreat rates in 3-D models of slab rollback. *Geochemistry Geophysics Geosystems*, 7(Q03012), 2006. doi: 10.1029/2005GC001056.

T. A. Stern, S. A. Henrys, D. A. Okaya, J. N. Louie, M. K. Savage, S. Lamb, H. Sato, R. Sutherland, and T. Iwasaki. A seismic reflection image for the base of a tectonic plate. *Nature*, 518(7537):85–88, 2015. ISSN 0028-0836. doi: 10.1038/nature14146. URL `http://www.nature.com/nature/journal/v518/n7537/full/nature14146.html`.

L. Stixrude and C. Lithgow-Bertelloni. Mineralogy and elasticity of the oceanic upper mantle: Origin of the low-velocity zone. *Journal of Geophysical Research*, 110(B3):B03204, 2005. ISSN 0148-0227. doi: 10.1029/2004JB002965. URL `http://doi.wiley.com/10.1029/2004JB002965`.

E. Tan, L. L. Lavier, H. J. A. Van Avendonk, and A. Heuret. The role of frictional strength on plate coupling at the subduction interface. *Geochemistry, Geophysics, Geosystems*, 13 (10), Oct 2012. ISSN 15252027. doi: 10.1029/2012GC004214. URL `http://doi.wiley.com/10.1029/2012GC004214`.

Y. Tian and D. Zhao. P-wave tomography of the western United States: Insight into the Yellowstone hotspot and the Juan de Fuca slab. *Physics of the Earth and Planetary Interiors*, 200-201:72–84, 2012. ISSN 00319201. doi: 10.1016/j.pepi.2012.04.004. URL `http://dx.doi.org/10.1016/j.pepi.2012.04.004`.

C. B. Till, T. L. Grove, R. W. Carlson, J. M. Donnelly-Nolan, M. J. Fouch, L. S. Wagner, and W. K. Hart. Depths and temperatures of <10.5 Ma mantle melting and the lithosphere-asthenosphere boundary below southern Oregon and northern California. *Geochemistry, Geophysics, Geosystems*, 14(4):864–879, Apr 2013. ISSN 15252027. doi: 10.1002/ggge.20070. URL `http://doi.wiley.com/10.1002/ggge.20070`.

D. R. Toomey, W. S. D. Wilcock, J. A. Conder, D. W. Forsyth, J. Blundy, E. Parmentier, and W. C. Hammond. Asymmetric mantle dynamics in the MELT region of the East Pacific Rise. *Earth and Planetary Science Letters*, 200(3-4):287–295, Jun 2002. ISSN 0012821X. doi: 10.1016/S0012-821X(02)00655-6. URL `https://linkinghub.elsevier.com/retrieve/pii/S0012821X02006556`.

D. R. Toomey, R. M. Allen, A. H. Barclay, S. W. Bell, P. Bromirski, R. W. Carlson, X. Chen, J. A. Collins, R. P. Dziak, B. Evers, D. W. Forsyth, P. Gerstoft, E. E. E. Hooft, D. Livelybrooks, J. Lodewyk, D. Luther, J. J. McGuire, S. Y. Schwartz, M. Tolstoy, A. M. Tréhu, M. Weirathmueller, and W. S. D. Wilcock. The Cascadia Initiative: A Sea Change In Seismological Studies of Subduction Zones. *Oceanography*, 27(2):138–150, jun 2014. ISSN 10428275. doi: 10.5670/oceanog.2014.49. URL `https://tos.org/oceanography/article/the-cascadia-initiative-a-sea-change-in-seismological-studies-of-subduction`.

A. M. Tréhu, I. Asudeh, T. M. Brocher, J. H. Luetgert, W. D. Mooney, J. L. Nabelek, and Y. Nakamura. Crustal Architecture of the Cascadia Forearc. *Science*, 266(5183):237–243, 1994.

A. M. Tréhu, R. J. Blakely, and M. C. Williams. Subducted seamounts and recent earthquakes beneath the central Cascadia forearc. *Geology*, 40(2):103–106, 2012. doi: 10.1130/G32460.1.

D. L. Turcotte and G. Schubert. *Geodynamics*. Cambridge University Press, Mar 2002. ISBN 978-0-521-66624-4.

S. van der Lee and G. Nolet. Seismic image of the subducted trailing fragments of the Farallon plate. *Nature*, 386(6622):266–269, Mar 1997. ISSN 0028-0836. doi: 10.1038/386266a0. URL `http://www.nature.com/doifinder/10.1038/386266a0`.

J. C. VanDecar and R. S. Crosson. Determination of teleseismic relative phase arrival times using multi-channel cross-correlation and least squares. *Bulletin of the Seismological Society of America*, 80(1):150–169, feb 1990. URL `http://bssa.geoscienceworld.org/content/80/1/150.full`.

L. S. Wagner, D. W. Forsyth, M. J. Fouch, and D. E. James. Detailed three-dimensional shear wave velocity structure of the northwestern United States from Rayleigh wave tomography. *Earth and Planetary Science Letters*, 299(3-4):273–284, 2010. ISSN 0012821X. doi: 10.1016/j.epsl.2010.09.005.

G. P. Waite, R. B. Smith, and R. M. Allen. Vp and Vs structure of the Yellowstone hot spot from teleseismic tomography: Evidence for an upper mantle plume. *Journal of Geophysical Research*, 111(B4):B04303, 2006. ISSN 0148-0227. doi: 10.1029/2005JB003867. URL `http://doi.wiley.com/10.1029/2005JB003867`.

K. J. Walowski, P. J. Wallace, E. H. Hauri, I. Wada, and M. A. Clynne. Slab melting beneath the Cascade Arc driven by dehydration of altered oceanic peridotite. *Nature Geoscience*, 8(May):404–409, 2015. ISSN 1752-0894. doi: 10.1038/ngeo2417.

Y. Wang, D. W. Forsyth, C. J. Rau, N. Carriero, B. Schmandt, J. B. Gaherty, and B. Savage. Fossil slabs attached to unsubducted fragments of the Farallon plate. *Proceedings of the National Academy of Sciences*, 110(14):5342–5346, Apr 2013. ISSN 0027-8424. doi: 10.1073/pnas.1214880110. URL `http://www.pnas.org/cgi/doi/10.1073/pnas.1214880110`.

S. C. Webb. Broadband seismology and noise under the ocean. *Reviews of Geophysics*, 36 (1):105–142, 1998. ISSN 8755-1209. doi: 10.1029/97RG02287. URL `http://dx.doi.org/10.1029/97RG02287`.

A. G. Wech. Interactive Tremor Monitoring. *Seismological Research Letters*, 81(4):664–669, Jul 2010. ISSN 0895-0695. doi: 10.1785/gssrl.81.4.664. URL `https://pubs.geoscienceworld.org/srl/article/81/4/664-669/143714`.

R. E. Wells, R. J. Blakely, Y. Sugiyama, D. W. Scholl, and P. A. Dinterman. Basin-centered asperities in great subduction zone earthquakes: A link between slip, subsidence, and subduction erosion? *Journal of Geophysical Research: Solid Earth*, 108(B10), Oct 2003. ISSN 01480227. doi: 10.1029/2002JB002072. URL `http://doi.wiley.com/10.1029/2002JB002072`.

P. Wessel, W. H. F. Smith, R. Scharroo, J. Luis, and F. Wobbe. Generic Mapping Tools: Improved Version Released. *Eos, Transactions American Geophysical Union*, 94(45):409–410, Nov 2013. ISSN 00963941. doi: 10.1002/2013EO450001. URL `http://doi.wiley.com/10.1002/2013EO450001`.

J. D. West, M. J. Fouch, J. B. Roth, and L. T. Elkins-Tanton. Vertical mantle flow associated with a lithospheric drip beneath the Great Basin. *Nature Geoscience*, 2(6):439–444, 2009. ISSN 1752-0894. doi: 10.1038/ngeo526. URL `http://dx.doi.org/10.1038/ngeo526`.

D. S. Wilson. Deformation of the so-called Gorda Plate. *Journal of Geophysical Research*, 94:3065–3075, 1989.

D. S. Wilson. Kinematics of overlapping rift propagation with cyclic rift failure. *Earth and Planetary Science Letters*, 96(3-4):384–392, 1990. ISSN 0012821X. doi: 10.1016/0012-821X(90)90014-O.

D. S. Wilson. Confidence intervals for motion and deformation of the Juan de Fuca Plate. *Journal of Geophysical Research*, 98(B9):16053, 1993. ISSN 0148-0227. doi: 10.1029/93JB01227.

D. S. Wilson. The Juan de Fuca plate and slab: Isochron structure and Cenozoic plate motions. In E. S. Kirby, K. Wang, and S. Dunlop, editors, *The Cascadia Subdunction Zone and Related Subduction Systems–Seismic Structure, Intraslab Earthquakes and Processes, and Earthquake Hazards: U.S. Geological Survey Open-File Report 02-328*, pages 9–12. U.S. Geological Survey, August 2002. ISBN 0-607-99675-7.

J. T. Wilson. Hypothesis of Earth's Behaviour. *Nature*, 198(4884):925–929, 1963. ISSN 0028-0836. doi: 10.1038/198925a0.

J. T. Wilson. A New Class of Faults and their Bearing on Continental Drift. *Nature*, 207 (4995):343–347, 1965. ISSN 0028-0836. doi: 10.1038/207343a0.

C. J. Wolfe, S. C. Solomon, G. Laske, J. A. Collins, R. S. Detrick, J. A. Orcutt, D. Bercovici, and E. H. Hauri. Mantle P-wave velocity structure beneath the Hawaiian hotspot. *Earth and Planetary Science Letters*, 303(3-4):267–280, Mar 2011. ISSN 0012821X. doi: 10.1016/j.epsl.2011.01.004. URL `http://dx.doi.org/10.1016/j.epsl.2011.01.004`.

M. Xue and R. M. Allen. The fate of the Juan de Fuca plate: Implications for a Yellowstone plume head. *Earth and Planetary Science Letters*, 264(1-2):266–276, 2007. ISSN 0012821X. doi: 10.1016/j.epsl.2007.09.047.

H. Yuan, B. Romanowicz, K. M. Fischer, and D. L. Abt. 3-D shear wave radially and azimuthally anisotropic velocity model of the North American upper mantle. *Geophysical Journal International*, 184(3):1237–1260, 2011. ISSN 0956540X. doi: 10.1111/j.1365-246X.2010.04901.x.

G. Zandt and E. D. Humphreys. Toroidal mantle flow through the western U.S. slab window. *Geology*, 36(4):295–298, 2008. ISSN 0091-7613. doi: 10.1130/G24611A.1. URL `https://pubs.geoscienceworld.org/geology/article/36/4/295-298/103824`.

G. Zandt, S. C. Myers, and T. C. Wallace. Crust and mantle structure across the Basin and Range–Colorado Plateau boundary at 37N latitude and implications for Cenozoic extensional mechanism. *Journal of Geophysical Research*, 100(B6):10529–10548, 1995.

G. Zandt, H. Gilbert, T. J. Owens, M. Ducea, J. Saleeby, and C. H. Jones. Active foundering of a continental arc root beneath the southern Sierra Nevada in California. *Nature*, 431 (September):6–8, 2004.

Q. Zhou, J. Hu, L. Liu, T. Chaparro, D. R. Stegman, and M. Faccenda. Western U.S. seismic anisotropy revealing complex mantle dynamics. *Earth and Planetary Science Letters*, 500: 156–167, Oct 2018a. ISSN 0012821X. doi: 10.1016/j.epsl.2018.08.015. URL `https://linkinghub.elsevier.com/retrieve/pii/S0012821X18304746`.

Q. Zhou, L. Liu, and J. Hu. Western US volcanism due to intruding oceanic mantle driven by ancient Farallon slabs. *Nature Geoscience*, 11(1):70–76, Jan 2018b. ISSN 1752-0894. doi: 10.1038/s41561-017-0035-y. URL `http://dx.doi.org/10.1038/s41561-017-0035-y`.

W. Zhu, G. A. Gaetani, F. Fusseis, L. G. J. Montési, and F. De Carlo. Microtomography of Partially Molten Rocks: Three-Dimensional Melt Distribution in Mantle Peridotite. *Science*, 332(6025):88–91, Apr 2011. ISSN 0036-8075. doi: 10.1126/science.1202221. URL `http://www.sciencemag.org/cgi/doi/10.1126/science.1202221`.